Reynolds-averaged Navier-Stokes and Large-Eddy Simulation Over and Inside Inhomogeneous Forests

Boudreault, Louis-Etienne

Publication date:
2015

Document Version
Publisher's PDF, also known as Version of record

Reynolds-averaged Navier-Stokes and Large-Eddy Simulation Over and Inside Inhomogeneous Forests

Louis-Étienne Boudreault
DTU Wind Energy PhD-0042 (EN)
June 2015

DTU Wind Energy
Department of Wind Energy

Author: Louis-Étienne Boudreault

Title: Reynolds-Averaged Navier-Stokes and Large-Eddy Simulation Over and Inside Inhomogeneous Forests

Department: DTU Wind Energy

DTU Wind Energy PhD-0042 (EN)

June 2015

ISBN: 978-87-93278-03-5

Pages: 115

Supervisors:

Ebba Dellwik

Andreas Bechmann

Jens Madsen

Grade:

Doctor of Philosophy

Sponsorship:

Center for Computational Wind Turbine Aerodynamics and Atmospheric Turbulence (COMWIND)

Vattenfall A/S

Technical University of Denmark
Department of Wind Energy
Frederiksborgvej 399
Bulding 118
4000 Roskilde
Telephone +45 46 77 50 32

www.vindenergi.dtu.dk

Reynolds-Averaged Navier-Stokes and Large-Eddy Simulation Over and Inside Inhomogeneous Forests

by

Louis-Étienne Boudreault

SUBMITTED TO THE DEPARTMENT OF WIND ENERGY
IN PARTIAL FULFILLMENT OF THE REQUIREMENTS FOR THE

PHD DEGREE

AT THE

TECHNICAL UNIVERSITY OF DENMARK

Committee:

Jakob Mann
DTU Wind Energy, DK
Professor

Andrew N. Ross
University of Leeds, UK
Lecturer

Edward G. Patton
NCAR, USA
Project Scientist III

CONTENTS

"If you think in terms of a year, plant a seed; if in terms of ten years, plant trees; if in terms of 100 years, teach the people."

Confucius

ABSTRACT

Numerical modeling is a useful tool for estimating the local wind resource in relation to wind turbine siting. At onshore sites, the wind climate is often influenced by nearby forests and they cause an increase in wind shear and turbulence intensity, which may compromise the performance of wind turbines. The wind flow over forests therefore needs to be predicted with a high degree of accuracy. Forests are however inhomogeneous in nature causing complex flow dynamics difficult to capture in numerical models. An accurate description of the canopy structure is necessary to properly evaluate the performance of wind models in such environment.

A systematic method to acquire gridded input of canopy structure from aircraft-based LiDAR scans of heterogeneous forests is defined. An extensive validation against ground-based measurements of the vertically summed frontal area density (or plant area index) and tree height is performed. The method is optimized both in terms of plant area index magnitude and spatial variability. A forest grid is generated from the LiDAR method using airplane scans of a 5×5 km^2 forested site in Sweden. The grid serves as the basis for Reynolds-averaged Navier-Stokes (RANS) simulations. Wind observations from an instrumented mast are used for validation where a good correlation is found for the mean wind speed of two contrasting wind directions with different influences from the upstream forest. The effects of successive simplifications of the forest representation show an important influence of the smaller heterogeneities on the flow when the site is complex. A second helicopter-based LiDAR scan of high resolution is used to create a highly detailed forest grid at the site of a previous forest edge experiment on the island of Falster in Denmark. This input is used in a large-eddy simulation (LES) study using the Advanced Regional Prediction System. The results show important spatial variability in the flow field, in close correlation with the canopy structure.

Both the RANS and the LES studies demonstrate that a detailed representation of the flow over and inside inhomogeneous forests can be acquired using the LiDAR-based forest parameterization. This opens up for a new way of developing and evaluating wind models adapted to complex forested terrains.

DANSK RESUMÉ

Numerisk modellering er et nyttigt redskab, når vindressourcen for vindmøller skal vurderes. På land kan skove forårsage forhøjet turbulens og "shear" i vinden, hvilket generelt mindsker vindmøllers produktivitet. Der er derfor brug for høj præcision, når vinden over skove skal vurderes. Skove er imidlertid heterogene og forårsager komplekse strømningsdynamikker, der er svære at fange i numeriske modeller. For at kunne forbedre modellerne er det vigtig med en præcis beskrivelse af den heterogene skovstruktur.

En systematisk metode til at opnå en præcis beskrivelse af den heterogene skovstruktur ud fra luftbaserede LiDAR scanninger er defineret. Metoden bliver grundigt valideret med jordbaserede målinger af træhøjden og af skovens frontareal densitet, og metoden bliver optimeret med hensyn til både størrelsen og variabiliteten af frontareal densiteten. I et hvert punkt af et fintmasket net, dækkende et 5×5 km^2 skov område i Sverige, bliver skovstrukturen bestemt med LiDAR metoden samt flybaserede scanninger. Nettet danner grundlag for RANS simuleringer (Reynolds-averaged Navier-Stokes), og vind målinger fra en mast anvendes til validering. De to beregnede vindretninger er påvirket forskelligt af skoven; men for begge retninger er der god overensstemmelse mellem den beregnede og målte vindhastighed. Gradvise forenklinger af skovbeskrivelsen viser den store indflydelse, som skovens små heterogeniteter har på strømningsdynamikken. En anden højopløst helikopter-baseret LiDAR scanning bruges til en yderst detaljeret beskrivelse af en skovkant på Falster (Danmark), hvor der tidligere har været en målekampagne. Denne skovbeskrivelse anvendes i en LES simulering (large-eddy simulation) ved hjælp af systemet: "Advanced Regional Prediction System". Resultaterne viser vigtig rumlig variabilitet i strømningen i tæt korrelation med den heterogene skovstruktur.

Både RANS og LES undersøgelserne viser, at en detaljeret beskrivelse af strømningen over og i heterogene skove kan opnås ved hjælp af LiDAR-baserede parametriseringer. I jagten på højere præcision er der derfor åbnet op for nye måder til at udvikle og evaluere vind modeller til skovrigt landskab.

ACKNOWLEDGEMENTS

I wish to thank my supervisors, Ebba Dellwik and Andreas Bechmann, who devoted their energy and young talent to achieve a successful project. Their support and comments were much useful and appreciated. Special thanks also goes to Jakob Mann and Niels Sørensen, for their skillful teaching and support during the project; Hans Jørgensen, for offering me a unique opportunity; Anette Werner, for achieving my administrative tasks; Jens Madsen, for his participation in the project and for the financial support; Sylvain Dupont, for his invaluable help and as well as the group at INRA for their fruitful collaboration; The DTU Wind Energy department, which do not skimp on resources to advance the wind turbine technology; My PhD colleagues, a motley crew of people with diverse backgrounds and origins, all united for progress; Chief-Nikola, my spiritual brother; My friends and Amelie, for their emotional and life assistance; My family, for which greek letters contained herein has no meaning, but who excels in speaking the language of love and support. The thesis is dedicated to all of them, and to those who find pragmatic solutions to modern challenges.

List of Figures

List of Tables

LIST OF PUBLICATIONS

Below is a list of dissemination activities accomplished during the thesis.

Journal articles

1. Boudreault, L.-E., Bechmann, A., Tarvainen, L., Klemedtsson, L., Shendryk, I., and Dellwik, E. (2014b). A LiDAR method of canopy structure retrieval for wind modeling of heterogeneous forests. *Agricultural and Forest Meteorology.* Accepted

2. Boudreault, L.-E., Dupont, S., Bechmann, A., and Dellwik, E. (2014c). Edge flow in inhomogeneous canopy. *Boundary-Layer Meteorology.* In preparation

Book chapter

1. Sørensen, N., Bechmann, A., Boudreault, L.-E., Koblitz, T., and Sogachev, A. (2013). CFD applications in wind energy using RANS. In *CFD for atmospheric flows and wind engineering.* von Karman Institute for Fluid Dynamics, Rhode-St-Genèse

Conference proceedings

1. Boudreault, L.-E., Bechmann, A., Sørensen, N., Sogachev, A., and Dellwik, E. (2014a). Canopy structure effects on the wind at a complex forested site. In *Journal of Physics: Conference Series*, volume 524 012112. IOP Publishing

2. Boudreault, L.-E., Dellwik, E., Bechmann, A., Sørensen, N., and Sogachev, A. (2012a). Numerical simulation of the air flow around a forest edge using LiDAR-derived forest heights. In *8th PhD Seminar on Wind Energy in Europe*, Zurich, Switzerland

Oral and poster presentations

1. Boudreault, L.-E., Dupont, S., Bechmann, A., and Dellwik, E. (2014d). Wind dynamics of an heterogeneous forest edge: large-eddy simulation and in-situ experiment. In *21st Symposium on Boundary Layers and Turbulence*, Leeds, UK

2. Boudreault, L.-E., Dellwik, E., Bechmann, A., Sørensen, N., and Sogachev, A. (2013). Plant area density extraction from aerial LiDAR scans for CFD applications over forests. In *13th EMS Annual Meeting & 11th European Conference on Applications of Meteorology (ECAM)*, Reading, UK

3. Boudreault, L.-E., Sogachev, A., Dellwik, E., and Bøgh, E. (2012b). Input parameters for CFD flow modelling of forested terrain. In *Proceedings of EWEA 2012 - European Wind Energy Conference & Exhibition. European Wind Energy Association (EWEA)*, Copenhagen, Denmark

1

INTRODUCTION

1.1 The wind energy context

Wind power capacity in Europe has increased at a compound annual growth rate of 10% over the last 13 years (EWEA, 2013). Onshore wind power contributed to a large extent to the increase, where a total of 110.7 GW capacity has now been installed (94% of the total wind power). The rapid expansion of wind energy steered the new wind farm developments towards sites where wind conditions are more difficult. Among them, forested sites became, and are becoming increasingly inevitable.

Forests constitute 31% of the world total land area (Fig. 1.1) and in Europe, 45% (FAO, 2010). The large cover fraction increase the probability of dealing with forests in wind energy projects. Siting wind turbines in such environment show numerous advantages, such as:

- The use of existing electrical grid infrastructure. Compared to offshore wind farms, costs can be avoided by making use of the already existing installations.
- Easy accessibility. The inland transport system makes it convenient for maintenance and installation, and also contributes to lower the costs.
- Low externalities. Problems such as noise, shadow effects and visual impacts are lesser in forests, since they are generally located far from residential areas.
- Decentralised electricity production. The regional communities near forested lands can benefit from the positive economic impacts of new wind farm developments.

However, the following disadvantages are encountered:

- Low wind speeds. Less energy is available in the wind over forests as they act as a sink of momentum.
- High turbulence and wind shear. The turbulence level and variations of velocity are more important over forests. The wind turbines therefore need to sustain higher loads.

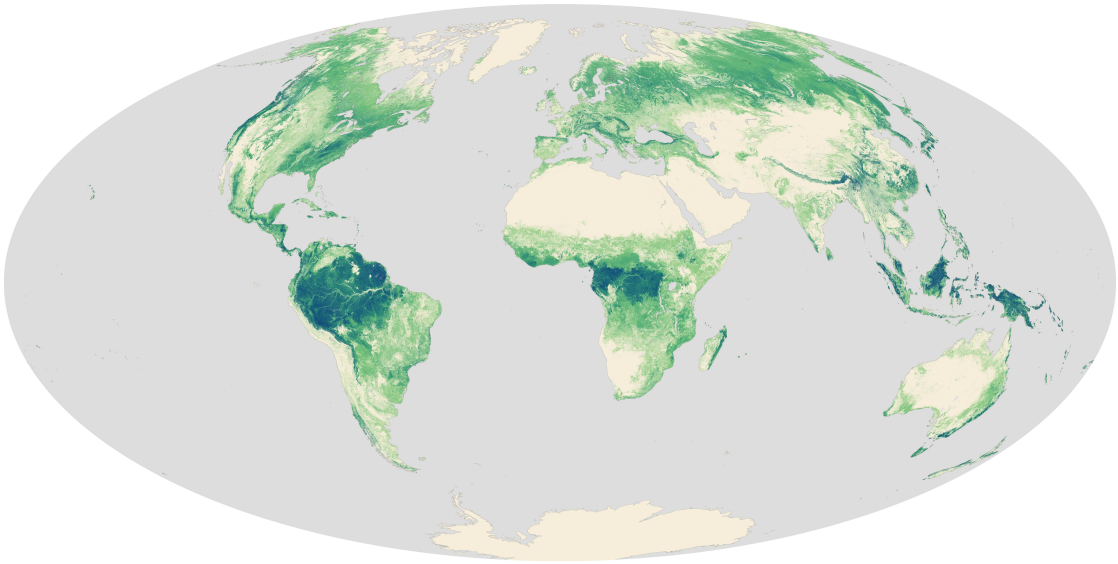

Figure 1.1: Canopy height map showing the distribution of forests over the world. Accessed from `http://visibleearth.nasa.gov/`.

- Stronger interactions. The wind is directly affected by the characteristics of the surface in the lower part of the atmosphere. The complex interactions often lead to the exceedance of existing wind farm design guidelines (IEC standards).

These factors traditionally contributed to more challenging wind ressource assessments, with higher risks, and higher costs associated. Albeit these disadvantages, a good knowledge of the wind resource could still lead to cost-effective projects. This can be accomplished by positioning the wind turbines at strategic locations, in favourable wind conditions (*i.e.* high wind speed and low turbulence). Numerical modeling proved useful to perform such task, but a higher degree of accuracy is needed.

1.2 Motivations of the thesis

In Europe, both private and public sectors are aiming at the reduction of wind resource assessments uncertainty. From 15% for onshore projects, the target is set to a global 3% by 2030 (TPWind, 2014). To achieve a lower uncertainty, the predictive capability of flow modeling tools needs improvements and forests are among important issues to consider. At micro-scale, the high degree of non-linear interactions between wind and forests is a challenging aspect to capture in numerical models. Even more complex interactions are expected for heterogeneous

forests (see *e.g* Lee, 2000).

The wind is affected by forest heterogeneities at various scales, among which two can be defined: (1) the tree- or plant-scale (1-10 m) and, (2) the stand-scale ($\geq$ 10 m). Over large areas of several kilometers, it is uncommon to find homogeneous forests with uniform properties. The landscape is rather fragmented and consists of a variety of stand-scale heterogeneities. For example, man-made activities often shaped the landscape into sharp forest edges and clearings. Moreover, within forest stands, the trees have different morphologies and they often are randomly distributed in non-plantation forests (tree-scale heterogeneity).

For the wind energy community, improved predictions over forest heterogeneities can greatly contribute to meet the low uncertainty targets. For this task, the precise description of the heterogeneous canopy structure is a key aspect to consider. The motivation and objectives of the current thesis are the following:

Problem statement: numerical predictions of the wind in the context of heterogeneous forests are currently performed with a high degree of uncertainty.

A first objective is to achieve higher-accuracy predictions by defining a better representation of forest heterogeneities in numerical models.

A second objective is to evaluate the effects of the detailed representation of inhomogeneous forests on the wind flow.

Below, three hypothesis are formulated in relation to these objectives (Section 1.3, 1.5 and 1.6). Each hypothesis are tested in Chapters 3–5 and are summarized in Chapter 6.

1.3 Choice of parameterization

It is important at this point to justify the method chosen to parameterize forests. Here, the focus is put on two methods: the modified roughness height and the drag parameterization.

The roughness height approach is derived from scaling approximations of the shear stress in the surface layer of the neutral atmosphere (Kaimal and Finnigan, 1998). The well-known logarithmic wind profile is derived from these approximations:

$$\overline{u} = \frac{u_*}{\kappa} \ln\left(\frac{z}{z_0}\right), \tag{1.1}$$

where $\bar{u}$ is the mean streamwise velocity component, u_* the friction velocity, κ the von Kármán constant, z the vertical direction above the surface and z_0, a parameter named the roughness height, which represents the influence of the surface under neutral conditions. In numerical models, boundary conditions can be

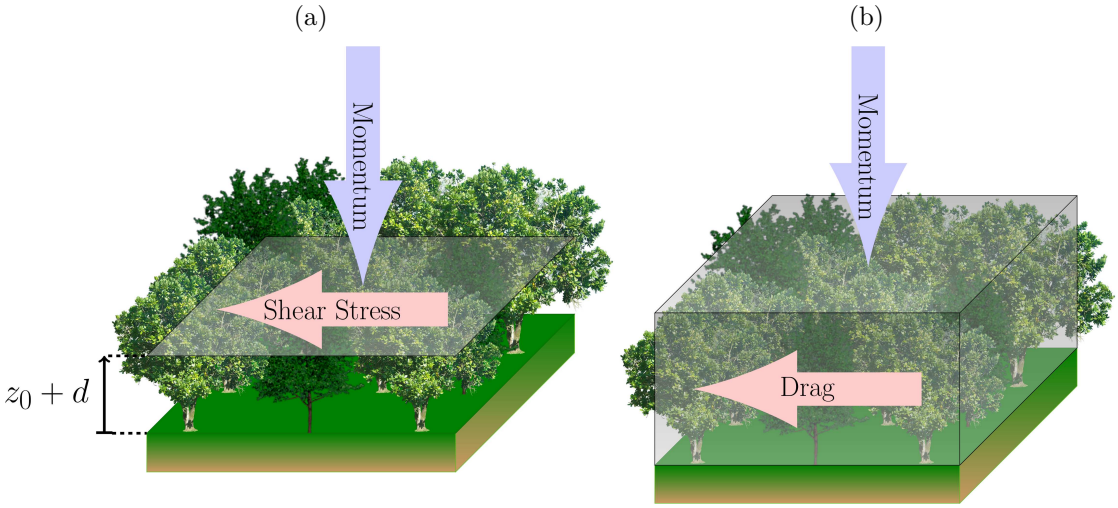

Figure 1.2: Schematic of principles behind (a) the roughness height and (b) the drag force.

applied according to logarithmic relationships, where z_0 is varied depending on the properties of the surface (see Fig. 1.2a). A complementary parameter often used together with the roughness height accounts for the displaced drag level, commonly represented by the displacement height d (Thom, 1971). The sum of roughness and displacement heights represents the level where the extrapolated logarithmic wind profile becomes zero. Several relationships between z_0 and d with measurable forest properties have been suggested: ratio to canopy height (*e.g* Hicks et al., 1975; Lindroth, 1993), forest density and plant area index (PAI) (Raupach, 1994, 1995; Verhoef et al., 1997). However, non-logarithmic behaviours are often encountered at forested sites. An example is for the enhanced mixing near the top of the canopy (Raupach et al., 1996b), which can influence the profile several canopy heights above the ground. To experimentally determine z_0 and d, tall towers are therefore required. As forested sites are rarely homogeneous, the flow at such towers is often adjusting to local heterogeneities (*e.g* Dellwik and Jensen, 2005), which makes accurate experimental assessment of z_0 and d difficult. Further difficulties arise when the parameterization of z_0 and d are used for varying atmospheric stability conditions, as they may become dependent on the flow conditions (Harman and Finnigan, 2007; Zilitinkevich, 2008). Taking these aspects into account, it is hard to distinguish whether z_0 and d are parameters that indirectly describe the forest structure, or variables describing the net aerodynamic effect of the forested surface.

In the drag parameterization approach (see Fig. 1.2b), a three-dimensional volume force represent the effect of the canopy in the momentum equation of the

temporally- and spatially-averaged Navier-Stokes equations as:

$$\frac{D\langle\bar{u}_i\rangle}{Dt} = \text{Pressure} + \text{Viscosity} + \text{Other volume forces} - \underbrace{C_d a|\langle\bar{u}\rangle|\langle\bar{u}_i\rangle}_{\text{Drag}}, \tag{1.2}$$

where $\bar{u}_i$ is the mean velocity vector and $|\bar{u}|$ its magnitude, C_d the drag coefficient, and a the frontal area density. The drag force parameterizes the net effect of the form and viscous drag produced by canopy elements. Although still approximative, the drag force allows more flexibility than the roughness height parameterization as the properties of the forest (represented with a) are treated separately from the dynamical effect of the forest (represented with C_d). Drag parameterization is however more complex as the canopy structure, or the distribution of a, needs to be specified for every point of the computational grid.

Over heterogeneous forests, the wind field is variable and the momentum transfer show differences compared to homogeneous forests and in free-air atmosphere. The flow prediction accuracy could therefore be diminished without a fine description the local variations in canopy stucture. Finding a systematic way of obtaining and prescribing the value of a for any type of forest is worthwhile to reach more precision in wind models. The thesis starts with the following hypothesis:

Hypothesis 1 *Using aerial LiDAR scans of forested areas in combination with Beer-Lambert's law, a high-accuracy forest description can be achieved for large computational domains.*

1.4 Acquiring the canopy structure

Forest canopies are very different from one site to another and their properties are highly variable in space. The only way to ensure a precise description of their properties is by performing actual measurements. Different methods can be considered for the determination of a (Jonckheere et al., 2004; Weiss et al., 2004). They can be classified as direct and indirect (Bréda, 2003). The direct methods consist of destructive sampling of trees, whereas indirect methods approximate the forest density using the light absorption properties of canopies (Morsdorf et al., 2006). The direct methods involve labor-intensive, ground-based tree height and density distribution measurements. For extended areas, this task is technically impracticable and local measurements of the canopy structure are often approximated to a larger scale. Approximating the trees and stand characteristics over such large scales can severely degrade the overall accuracy of the wind simulations. Thus, indirect methods represent a potentially useful approach for determining stand structure for applications requiring high accuracy description over extended areas.

The first task of the project was to identify and evaluate the indirect methods available (see Boudreault et al., 2012b, Appendix A). Products from space shuttle SRTM, satellite ASTER, satellite Terra MODIS and satellite Landsat 7 (ETM+) could provide useful information about forest properties. In our evaluation, it was found that the tree height estimations from the SRTM and ASTER satellites include information from the forest, but far from the precision needed for numerical modeling. The digital surface model based on aerial light detection and ranging (LiDAR) scans (ALS), a widely used output, underestimate the forest height by several meters, whereas the maximum height deduced from the raw point cloud were in good accordance with the forest inventory measurements. For the vertically summed frontal area density, or PAI, the satellite-based estimates should be used with care as calibration to site specific measurements is necessary (le Maire et al., 2012). Sensitivity to a number of environmental factors (*e.g.* presence of clouds or aerosols) can be found in the derived PAI values (Borak, 2009). The PAI values are also much dependent on the various scaling relationships used to obtain them. The Landsat 7 showed unphysical variability in the derived PAI. However, the mean value of PAI from Landsat 7 in the summer showed a good comparison with the mean value from a ground-based instrument (LAI-2000, LI-COR, Inc., Lincoln, Nebraska). A significant difference between MODIS and the ground-based instrument was obtained. Although reasonable estimates of PAI could be obtained from specific products, sattelites can only provide a coarse estimate of tree height and therefore, a would also become a coarse estimate derived from these products. The rather low spatial resolutions (100 m for SRTM, 15-90 m for ASTER and 30 m for Landsat) is also limiting in terms of accuracy. Reprocessing the point cloud from aerial LiDAR scans was therefore the most promising method for acquiring the canopy structure accurately.

An ALS is performed using an aircraft with a combined LiDAR and global positioning system (GPS) (*e.g* El-Sheimy et al., 2005). The x, y and z positions, where the reflection of each LiDAR pulse occurs, form a so-called point cloud. In addition to the terrain elevation, the beam penetration gives information about the canopy structure. Several forest attributes can be recovered from the point cloud (see van Leeuwen and Nieuwenhuis, 2010, for review). These include, for example, tree height (*e.g* Popescu and Wynne, 2004; Mcinerney et al., 2010) and plant area index (*e.g* Lefsky et al., 1999; Morsdorf et al., 2006; Solberg et al., 2006, 2009; Richardson et al., 2009). Although a has not previously been derived from the point cloud, a few studies have included the vertical distribution of the LiDAR reflections for determining the canopy structure (*e.g* Coops et al., 2007; Peduzzi et al., 2012). A good agreement was generally found between the ALS-derived properties and ground-based measurements in the various studies mentioned. However, the focus was put on a few local point validations, and no

systematic method to produce grid estimates input of a useful for numerical modeling has been proposed so far. In the present study, such a method is proposed. These developments constitute a major part of the thesis and are presented in the first part of Chapter 3.

1.5 Simulating the wind at micro-scale

Various numerical techniques are available to simulate the turbulent airflow. At micro-scale (spatial scales of 2 km or less, *e.g.* Orlanski, 1975), Reynolds-averaged Navier-Stokes (RANS) is an acknowledged tool to perform such task (see *e.g* Sørensen et al., 2013) as it combines both, reasonable accuracy and affordable computational requirements. For this reason, RANS has commonly been used in wind energy to perform siting assessments. For the thesis, it was therefore worthy to propose and show improvements in connection with this tool.

In the second part of Chapter 3, RANS simulations are performed using the LiDAR method to verify whether a detailed canopy description is important to improve the modeling accuracy. The method is tested using scans from a 5×5 km^2 area of a forested site in Sweden. For the first time, a large-scale numerical reconstruction of the three-dimensional wind field using a small-scale canopy structure description is presented. For this site, a vertical array of sonic anemometers is used for validation. In a second study (Chapter 4), the effects of successive simplifications of the forest representation on the wind field is investigated. The goal of this second study is to verify whether:

Hypothesis 2 *A detailed representation of the canopy structure is important to achieve high-accuracy simulations of the wind field over large areas.*

1.6 Simulating the edge flow in inhomogeneous canopy

Edges are common type of heterogeneities encountered in forests. An improved understanding of the changes of wind and turbulence at and near forest edges has implications for the fields of *e.g.* wind resource assessment, air pollution or pollen dispersion, as well as for the interpretation of near-edge flux measurements. The wind near and within forest edges is however complex, and severely limits the prediction accuracy of wind models. A better characterization of edge flows and therefore, their better representation in simple wind models, could potentially lead to improved accuracy.

With this motivation, the study of an edge flow using large-eddy simulation (LES) is conducted. The LiDAR method developed in Chapter 3 is a strong basis

to investigate the impacts of tree-scale heterogeneities in edge flow, and to verify whether they should be carefully accounted for in numerical modeling. For this purpose, high resolution scans are gathered for a site located on the Falster island in Denmark. Although restricted to a smaller domain, LES is preferred to RANS in this context as high-order statistics can be calculated and therefore, a more in-depth investigation can be performed. This study is presented in Chapter 5 starting with the following third and last hypothesis:

Hypothesis 3 *Tree-scale heterogeneities do not have an important impact in edge flow.*

1.7 Novelty of the thesis

Several contributions are brought in the thesis while some aspects are left for future developments.

The thesis is about a method for acquiring detailed forest properties for large areas from aircraft-based LiDAR scans applicable to a wide variety of wind models. Having a method to estimate highly-realistic canopy structures, new insights about flows in inhomogeneous canopies are gained using RANS and LES simulations. The impacts of the thesis are not restricted only to wind energy, but also to other fields of application where accurate information involving wind interactions with forests are needed.

The thesis is not about improvements of numerical techniques or turbulence and canopy models. Choices of specific models based from previous works are rather made and used in the background of the thesis. Efforts are rather dedicated to the canopy structure acquisition and the general understanding of inhomogeneous canopy flows for improving wind models. The thesis is also not about development of new methods of measurement analysis, but rather the use of existing measurement methods to validate the numerical setups defined.

1.8 Outline of the thesis

The thesis is subdivided in five chapters, where Chapters 3-5 correspond to articles prepared during the thesis. The following topics are addressed:

Chapter 2 reflects all necessary material needed to understand the thesis. The topics adressed are only briefly introduced and various references are indicated for more details.

Chapter 3 is about a LiDAR method of canopy structure retrieval developed for wind modeling. The method is tested for a forested site in Sweden using RANS simulations.

Chapter 4 concerns RANS simulations for the site described in Chapter 3, but the canopy structure is successively simplified from the LiDAR method. The purpose of this analysis is to verify whether simplifying the canopy structure produces significant differences in the wind field at micro-scale.

Chapter 5 is related to LES simulations of a forest edge using high-resolution scans together with the LiDAR method. The objective of this analysis is to quantify the impacts of tree-scale heterogeneities in edge flow.

Chapter 6 summarizes the thesis with conclusions of the work achieved and outlooks of some future perspectives.

Supplementary material is provided in the Appendix.

2

BACKGROUND

To describe the airflow motion above and within forest canopies, governing equations and statistical operators are introduced in Section 2.1. In Sections 2.2 and 2.3, respectively, the RANS and LES models used to perform the wind simulations are detailed. Aspects of canopy structure theory are finally introduced in Section 2.4.

2.1 Governing equations

2.1.1 Navier-Stokes equations

The Navier-Stokes (NS) equations in the incompressible form are obtained by applying Newton's second law to a fluid particle and read

$$\frac{\partial u_i}{\partial t} + u_j \frac{\partial u_i}{\partial x_j} = -\frac{1}{\rho}\frac{\partial p}{\partial x_i} + \nu \frac{\partial^2 u_i}{\partial x_j \partial x_j} + f_i^C + f_i, \tag{2.1}$$

$$\frac{\partial u_i}{\partial x_i} = 0, \tag{2.2}$$

where p is the pressure, ν the kinematic viscosity, f_i^C the Coriolis force, f_i are other body forces acting on the fluid and $u_i \equiv \boldsymbol{u} \equiv \{u_1, u_2, u_3\} \equiv \{u_x, u_y, u_z\} \equiv \{u, v, w\}$ the velocity components in the Cartesian coordinate system $x_i \equiv \boldsymbol{x} \equiv \{x_1, x_2, x_3\} \equiv \{x, y, z\}$. By convention, z is taken as the vertical direction, and x is aligned with the mean wind vector. Eqs. 2.1 and 2.2 are known as the momentum and continuity equations, respectively.

Coriolis force

In the atmospheric boundary-layer, the Coriolis force f_i^C is an external body force acting on the air due to the Earth's rotation,

$$f_i^C = -2\epsilon_{ijk}\Omega_j u_k \approx f_c \epsilon_{ij3} u_j, \tag{2.3}$$

where Ω_j is the Earth's angular velocity vector, $f_c = 2\omega \sin\phi \approx 10^{-4}$ in $\mathrm{rad\,s^{-1}}$ is the Coriolis frequency, $\omega = 7.27 \times 10^{-5}$ in $\mathrm{rad\,s^{-1}}$ the angular velocity of the Earth, and ϕ the latitude of the site under consideration ($\phi = 43°\mathrm{N}$). The Coriolis force will be accounted or assumed negligible depending on the context of the study. In the last approximation of Eq. 2.3, the Coriolis force is neglected in the vertical.

2.1.2 Averaging and filtering operators

Time-averaging

The time-averaging operator of a scalar or vector ϕ_i, denoted by an overbar, and the departure from the time-average, denoted by a prime, are defined as

$$\bar{\phi}_i(\boldsymbol{x}) = \frac{1}{T}\int_t^{t+T} \phi_i(\boldsymbol{x},t)\mathrm{d}t, \quad \phi_i' = \phi_i - \bar{\phi}_i \quad \text{where} \quad \overline{\phi_i'} = 0, \tag{2.4}$$

and where T is the averaging time-period. This operator is used to calculate time-averaged wind statistics from LES outputs, and to simplify the instantaneous flow in the NS-equations into a mean and a fluctuating component, the so-called *Reynolds decomposition* (Section 2.2). Here, the flow is averaged over a finite time-scale T much longer than the turbulent fluctuations, but small enough to retain the mean time-variations greater than T ($\partial\bar{\phi}_i/\partial t \neq 0$). For wind observations, T is typically taken as 10-30 minutes between averaging samples, and about 30 minutes for a large-eddy simulation run.

Spatial-averaging

The spatial-averaging operator, denoted by angled brackets, and the departure from the spatial-average, denoted by a double prime, are defined as,

$$\langle\phi_i(\boldsymbol{x},t)\rangle = \frac{1}{V}\iiint_V \phi_i(\boldsymbol{x}+\boldsymbol{y},t)\mathrm{d}^3\boldsymbol{y}, \quad \phi_i'' = \phi_i - \langle\phi_i\rangle \quad \text{where} \quad \langle\phi_i''\rangle = 0, \tag{2.5}$$

and V is an averaging volume. This operator is used for grid-volume averaging the NS-equations in the canopy airspace (Section 2.1.3), thereafter used for constructing the RANS model (Section 2.2), or at larger scales, to perform a spatially-averaged statistical analysis of the time-averaged flow field. For this latter purpose, the volume-averaging is defined as an horizontal-averaging operator over a region R, where the dimension x_3 is ignored (see Chapter 5).

For averaging the NS-equations, the surfaces occupied by plant parts are excluded from V. In the x_3 direction, the extension of V is small enough to resolve the vertical variability in tree density. In x_1 and x_2, it extends over a length-scale much smaller than the large-scale nonrandom inhomogeneity in canopy structure (Raupach et al., 1996a), but is extensive enough to eliminate small-scale heterogeneity (see Finnigan, 1985, for a discussion of the mathematical implications of the latter approximation). In reality, the separation of scales can be considered to occur at the plant-scale, as a canopy usually consists of trees of the same species showing similar (homogeneous) structural characteristics.

Spatial-filtering

The spatial-filtering operator, denoted by an overtilde, and the residual sub-filter scale field, denoted by a s upper indice, are defined as (Leonard, 1974),

$$\tilde{\phi}_i(\boldsymbol{x},t) = \int_D G(\boldsymbol{x}-\boldsymbol{y})\phi_i(\boldsymbol{y},t)\mathrm{d}\boldsymbol{y}, \quad \phi_i^s = \phi_i - \tilde{\phi}_i \quad \text{where} \quad \widetilde{\phi_i^s} \neq 0, \tag{2.6}$$

where D is the entire domain of the flow field and G, a box-type filter given by

$$G(\boldsymbol{x}-\boldsymbol{y}) = \begin{cases} \frac{1}{V_R} & \text{if} \quad |x_i - y_i| \leq \frac{\Delta_i}{2}, \\ 0, & \text{otherwise}, \end{cases} \tag{2.7}$$

and $V_R = \Delta_1\Delta_2\Delta_3$ is the box-volume with side lengths Δ_i used to perform the flow filtering. The grid-filtered NS-equations describes the large-eddy simulation mathematical model (Section 2.3). Compared to spatial-averaging, spatial-filtering describes a cut-off scale where the fluctuations smaller than V are removed.

2.1.3 NS-equations in the canopy airspace

Canopies are characterized by randomly distributed canopy elements obstructing the airflow, such as branches, leaves and stems. A detailed representation of the flow around each individual canopy elements is too complex and a statistical description is required. First-order moment equations in the canopy airspace can be obtained from the NS-equations (Eq. 2.1) by performing, 1– time-averaging (Eq. 2.4) and 2– spatial-averaging (Eq. 2.5). Let us suppose that the averaging time-period is long enough, that the averaging-volume is large and thin enough to neglect the Leonard stresses (see Leonard, 1974; Finnigan, 1985, 2000), and that the time-derivative terms do not vanish knowing that in reality, a true ensemble average is experimentally unattainable (Finnigan, 2000). The momentum equations using this procedure read (Wilson and Shaw, 1977; Raupach and Shaw, 1982; Finnigan, 1985, 2000)

$$\frac{\partial\langle\bar{u}_i\rangle}{\partial t} + \langle\bar{u}_j\rangle\frac{\partial\langle\bar{u}_i\rangle}{\partial x_j} = -\frac{1}{\rho}\frac{\partial\langle\bar{p}\rangle}{\partial x_i} + \frac{\partial\tau_{ij}}{\partial x_j} - 2\epsilon_{ijk}\Omega_j\langle\bar{u}_k\rangle + \langle F_{Di}\rangle, \tag{2.8}$$

$$\frac{\partial\langle\bar{u}_i\rangle}{\partial x_i} = 0, \tag{2.9}$$

where

$$\tau_{ij} = -\underbrace{\overline{\langle u_i' u_j' \rangle}}_{Turbulent} - \underbrace{\langle \bar{u}_i'' \bar{u}_j'' \rangle}_{Dispersive} + \underbrace{\nu \frac{\partial \langle \bar{u}_i \rangle}{\partial x_j}}_{Viscous}, \tag{2.10}$$

$$\langle F_{Di} \rangle = \underbrace{\frac{1}{V} \sum_{n=1}^{N} \iint_{S_n} \bar{p} \mathbf{n}_e \mathrm{d}S}_{Form\ drag} - \underbrace{\frac{\nu}{V} \sum_{n=1}^{N} \iint_{S_n} \frac{\partial \bar{u}_i}{\partial n} \mathrm{d}S}_{Viscous\ drag}, \tag{2.11}$$

where S_n is the surface of the nth canopy element within V and $\mathbf{n}_e$, the unit vector pointing away from its surface. Performing spatial-averaging (Section 2.1.2) in a multiply-connected airspace, where the plant parts intersect the volume V, leads to spatial discontinuities in the differentiation at the air-canopy elements interfaces, and the terms in $\langle F_{Di} \rangle$ remain due to *non-commutativity* (see Raupach and Shaw, 1982). Respectively, these terms represent the form (or pressure) and viscous drag produced by the canopy elements. It is physically impossible to retrieve the mean pressure and velocity field around each canopy elements inside the volume V to sum their form and viscous drag contributions. For this reason, the net effect of plant drag inside V is often parameterized as

$$\langle F_{Di} \rangle = -C_d a |\langle \bar{u} \rangle| \langle \bar{u}_i \rangle, \tag{2.12}$$

where it is assumed that the form drag dominate in $\langle F_{Di} \rangle$ from the dependence on the square of the velocity, altough some authors reported a non-negligible contribution of viscous drag in the total drag (*e.g.*, Thom, 1968).

In addition to turbulent and viscous fluxes, the total fluxes τ_{ij} (Eq. 2.10) contain so-called dispersive fluxes, or spatial correlation in time-averaged velocities. In the following RANS and LES equations, where the grid-volume averaging and filtering of the NS-equations are applied at the scale of V, the small-scale dispersive and viscous fluxes below the grid size are ignored, and the heterogeneities smaller than the computational grid volumes are removed using the drag parameterization. The possible dispersive fluxes arising above the grid size are kept resolved in the simulations when an heterogeneous canopy is considered. At these larger scales, the contribution of dispersive fluxes were traditionally considered small compared to turbulent fluxes (Kaimal and Finnigan, 1998) and the homogeneity of the flow was often assumed. The validity of this hypothesis is evaluated in Chapter 5 for an edge flow using an heterogeneous canopy description.

2.2 Reynolds-averaged Navier-Stokes model

2.2.1 RANS equations

RANS equations are here obtained from the set of equations (2.8)-(2.12) presented in Section 2.1.3. The dispersive and viscous fluxes are assumed small compared to turbulent fluxes and are henceforth ignored from the equations. The remaining turbulent fluxes $\langle\overline{u_i'u_j'}\rangle$ are non-linear terms requiring modeling in order to close the system of equations. This can be accomplished by using the Boussinesq hypothesis:

$$\tau_{ij} = -\langle\overline{u_i'u_j'}\rangle \approx 2\nu_t S_{ij} - \frac{2}{3}k\delta_{ij}, \tag{2.13}$$

where ν_t is the eddy viscosity, $k = \frac{1}{2}\langle\overline{u_i'u_i'}\rangle$ the turbulent kinetic energy (TKE), and δ_{ij} the Kronecker delta. The mean strain rate of deformation tensor S_{ij} writes

$$S_{ij} = \frac{1}{2}\left(\frac{\partial\langle\bar{u}_i\rangle}{\partial x_j} + \frac{\partial\langle\bar{u}_j\rangle}{\partial x_i}\right). \tag{2.14}$$

The Boussinesq hypothesis is assuming the turbulent fluxes to be proportional to the mean velocity gradient. The second term on the right-hand side of Eq. 2.13 is needed to obtain the proper trace of τ_{ij}, so that contraction on the index yields $\tau_{ii} = -2k$ since $S_{ii} = 0$ for an incompressible flow (Wilcox, 2006). Using the Boussinesq hypothesis and the Coriolis force approximation (Eq. 2.3), the RANS equations become

$$\langle\bar{u}_j\rangle\frac{\partial\langle\bar{u}_i\rangle}{\partial x_j} = \underbrace{F_{RANS}}_{Forcing} - \frac{1}{\rho}\frac{\partial(\langle\bar{p}\rangle + \frac{2}{3}k)}{\partial x_i} + \frac{\partial}{\partial x_j}\left[\nu_t\left(\frac{\partial\langle\bar{u}_i\rangle}{\partial x_j} + \frac{\partial\langle\bar{u}_j\rangle}{\partial x_i}\right)\right] - f_c\epsilon_{ij3}\langle\bar{u}_j\rangle - C_d a|\langle\bar{u}\rangle|\langle\bar{u}_i\rangle, \tag{2.15}$$

$$\frac{\partial\langle\bar{u}_i\rangle}{\partial x_i} = 0, \tag{2.16}$$

where the forcing term:

$$F_{RANS} = \delta_{i2}\frac{1}{\rho}\frac{\partial P}{\partial x_i}, \tag{2.17}$$

is a constant pressure gradient added in the momentum equation to drive the flow. The magnitude of the forcing is determined from the (geostrophic) balance with the Coriolis force above the boundary layer height as (see Bechmann, 2006):

$$\frac{\partial P}{\partial x_2} = -\rho f_c G, \tag{2.18}$$

where G is the desired x-oriented geostrophic wind at the top boundary of the computational domain. This forcing setup is used in Chapter 3 whereas it is omitted in Chapter 4, along with the Coriolis force.

2.2.2 Standard $k-\epsilon$ model

The eddy viscosity ν_t in the standard $k-\epsilon$ model (Jones and Launder, 1972) is provided with

$$\nu_t = C_\mu \frac{k^2}{\epsilon}, \tag{2.19}$$

where C_μ is a calibrated constant, k is the turbulent kinetic energy and ϵ is the turbulent dissipation rate. Solutions for k and ϵ are found by solving the two following transport equations:

$$\langle \bar{u}_i \rangle \frac{\partial k}{\partial x_j} = \tau_{ij} \frac{\partial \langle \bar{u}_i \rangle}{\partial x_j} - \epsilon + \frac{\partial}{\partial x_j} \left[\frac{\nu_t}{\sigma_\epsilon} \frac{\partial k}{\partial x_j} \right] + S_k, \tag{2.20}$$

and

$$\langle \bar{u}_i \rangle \frac{\partial \epsilon}{\partial x_j} = C_{\epsilon 1} \frac{\epsilon}{k} \tau_{ij} \frac{\partial \langle \bar{u}_i \rangle}{\partial x_j} - C_{\epsilon 2} \frac{\epsilon^2}{k} + \frac{\partial}{\partial x_j} \left[\frac{\nu_t}{\sigma_\epsilon} \frac{\partial \epsilon}{\partial x_j} \right] + S_\epsilon, \tag{2.21}$$

where the constants are $(C_\mu, \kappa, \sigma_k, \sigma_\epsilon, C_{\epsilon 1}, C_{\epsilon 2}) = (0.06, 0.4, 1.0, 2.1, 1.52, 1.83)$. The set of constants presented here differs from the standard set of constants originally proposed by Jones and Launder (1972). The $(C_{\epsilon 1}, C_{\epsilon 2})$ constants are rather set following Kantha (2004), the von Kármán constant to the widely used value of $\kappa = 0.4$, and the Schmidt number, to the constant-stress relationship $\sigma_\epsilon = \kappa^2 / (\sqrt{C_\mu}(C_{\epsilon 2} - C_{\epsilon 1}))$ (Wilcox, 2006). The constant C_μ is optimized from numerical simulations in the work presented in Chapter 3. S_k and S_ϵ are sink terms expressing the energy loss caused by drag (see Sanz, 2003; Katul et al., 2004). The model used to express these terms is presented in Section 2.2.3.

Length-scale limiter

The length-scale in the $k-\epsilon$ model grows infinitely with height, an effect incompatible with the upper part of the atmospheric boundary-layer. A correction can be applied, as suggested by Apsley and Castro (1997), where the constant $C_{\epsilon 1}$ in Eq. 2.21 is replaced by the new constant $C^*_{\epsilon 1}$ as

$$C^*_{\epsilon 1} = C_{\epsilon 1} + (C_{\epsilon 2} - C_{\epsilon 1}) \frac{l}{l_{max}}, \tag{2.22}$$

where the mixing-length l of the model is given by

$$l = C_\mu^{\frac{3}{4}} \frac{k^{\frac{3}{2}}}{\epsilon}. \tag{2.23}$$

The maximum length-scale l_{max} is prescribed using a relationship proposed by Blackadar (1962):

$$l_{max} = \frac{0.00027G}{f_c}, \tag{2.24}$$

where G is the geostrophic wind above the boundary-layer height, and f_c the Coriolis frequency (see Section 2.1.1). The length-scale limiter and the forcing setup described in Section 2.2.1 are used in Chapter 3 only.

2.2.3 RANS forest model

As presented in Sogachev and Panferov (2006) and Sogachev (2009), the following source terms S_k and S_ϵ are added in Eq. 2.20 and 2.21 to model the effect of the canopy

$$S_k = 0, \tag{2.25}$$

$$S_\epsilon = 12(C_{\epsilon 2} - C_{\epsilon 1})C_\mu^{1/2} C_d a |\langle \bar{u} \rangle| \epsilon. \tag{2.26}$$

Retaining only the term S_ϵ, the model is reproducing the enhanced dissipation caused by wake eddies behind the canopy elements. The model was chosen for its simplicity as only one term in addition to drag is needed, and because no new constants other than the constants already defined in the $k-\epsilon$ equations are required.

2.2.4 EllipSys3D code

The EllipSys3D code (Michelsen, 1992, 1994; Sørensen, 1995) is a computer program developed at the wind energy department of the Technical University of Denmark, to simulate the wind around terrains, airfoils and wind turbines. The code is based on a curvilinear finite-volume formulation of the discretized incompressible NS-equations on structured unstaggered grids. A multi-block decomposition approach of the domain is used to perform fast parallel computing using the message passing interface (MPI). The numerical procedure used in this work to solve the discretized equations is based on the semi-implicit method for pressure linked equations (SIMPLE) algorithm (Patankar, 1980), and the tri-diagonal matrix (TDMA) algorithm. The coupling between pressure and velocity is handled using the Rhie/Chow interpolation technique (Rhie, 1981). The solution is accelerated using a multigrid method, *i.e.* coarse solutions are first obtained on coarse grid levels, and interpolated onto the next finer grid levels as initial solutions. Volume forces such as canopy drag could create numerical oscillations, where steady-state solutions are difficult to obtain. The approach described in Rhétoré (2009) was used in the solver to mitigate this issue.

2.3 Large-eddy simulation model

2.3.1 LES equations

In large-eddy simulation, large eddies of the turbulent flow are explicitly resolved whereas the motion of the smaller-scale eddies are modeled. The LES equations for canopy flows (Shaw and Schumann, 1992; Lien et al., 2005) are obtained from the filter or grid volume-averaging operator described in Section 2.1.2. Using the drag parameterization to characterize the form and viscous drag resulting from the spatial-filtering operation (similarly obtained as in Section 2.1.3), the LES momentum equations read

$$\frac{\partial \tilde{u}_i}{\partial t} + \tilde{u}_j \frac{\partial \tilde{u}_i}{\partial x_j} = \underbrace{F_{LES}}_{Forcing} - \frac{1}{\rho}\frac{\partial \tilde{p}}{\partial x_i} - \frac{\partial \tau^s_{ij}}{\partial x_j} - C_d a \sqrt{\tilde{u}_j \tilde{u}_j}\tilde{u}_i, \tag{2.27}$$

where $\tau^s_{ij} = \widetilde{u^s_i u^s_j} = \widetilde{u_i u_j} - \tilde{u}_i \tilde{u}_j$ is the residual sub-filter scale stress tensor (Leonard, 1974). The forcing term F_{LES} will be detailed in Chapter 5. Henceforth, τ^s_{ij} will be designated as the sub-grid scale (SGS) stress tensor as the computational grid is used as an implicit filter of the turbulent motions. τ^s_{ij} needs to be modeled using a closed system of equations. One such model is described in the next section and is used in the present work.

The LES equations introduced above are formulated slightly different in the ARPS code. The differences found are summarized in Section 2.3.4 and detailed in Chapter 5.

2.3.2 Sub-grid scale model

A transport equation of SGS-turbulent kinetic energy e and horizontal and vertical length-scales l_h and l_v (1.5-equation closure model) is used in Eq. 2.27 for closure. The SGS-stress tensor τ^s_{ij} in Eq. 2.27 is approximated using the eddy-viscosity hypothesis:

$$\tau^s_{ij} = -\nu_t \left(\frac{\partial \tilde{u}_i}{\partial x_j} + \frac{\partial \tilde{u}_j}{\partial x_i} \right), \tag{2.28}$$

where ν_t is given by

$$\nu_t = (1 - \delta_{3j})\nu_{t,h} + \delta_{3j}\nu_{t,v}, \tag{2.29}$$

and where $\nu_{t,h}$ and $\nu_{t,v}$ are respectively the horizontal and vertical eddy-viscosities. Using relationships for the product of a velocity scale $\sqrt{e}$ and a horizontal and

vertical length scales, l_h and l_v, respectively, $\nu_{t,h}$ and $\nu_{t,v}$ can be approximated as

$$\nu_{t,h} = 0.1\sqrt{e}l_h, \tag{2.30}$$
$$\nu_{t,v} = 0.1\sqrt{e}l_v. \tag{2.31}$$

The length scales are obtained from the grid spacing as

$$l_h = \sqrt{\Delta x \Delta y}, \tag{2.32}$$
$$l_v = \Delta z, \tag{2.33}$$

and the velocity scale from a transport equation of the SGS turbulent kinetic energy e as

$$\frac{\partial e}{\partial t} + \tilde{u}_j \frac{\partial e}{\partial x_j} = -\tau_{ij}^s \frac{\partial \tilde{u}_i}{\partial x_j} + \frac{\partial}{\partial x_j}\left(2\nu_t \frac{\partial e}{\partial x_j}\right) - C_\epsilon \frac{e^{3/2}}{l_v} + S_e, \tag{2.34}$$

where C_ϵ is 3.9 at the lowest model level and 0.93 above, according to Deardorff (1980) and Moeng (1984). The terms on the right-hand side of Eq. 2.34 represent respectively the dynamic shear production, the turbulent transport and the dissipation; the last term S_e is discussed in the next section. Following Deardorff (1980), the pressure transport term from the prognostic SGS-TKE equation was included into the turbulent transport term by doubling its value, as both terms are assumed equivalent at the sub-grid scale.

2.3.3 LES forest model

The effect of canopy drag in the SGS-TKE (Eq. 2.34) is accounted with the following source term S_e (Shaw and Schumann, 1992; Watanabe, 2004):

$$S_e = -2C_d a \sqrt{\tilde{u}_j \tilde{u}_j} e. \tag{2.35}$$

This term represent the turbulent energy transfer from the larger to the smaller scales, or energy cascade, which is physically interrupted at the scale of the canopy elements. The largest structures directly transfer their energy to the fine wake turbulence structures behind the canopy elements, where the energy becomes rapidly dissipated (Baldocchi and Meyers, 1988; Finnigan, 2000; Cava and Katul, 2008). The term S_e represents the enhanced dissipation produced by wake-scale motions and is known as the SGS-TKE cascade term.

2.3.4 ARPS code

The Advanced Regional Prediction System (ARPS, version 5.1.5) solver is used to implicitely solve the LES equations. The ARPS code is designed for weather

systems prediction in meso-scale flows but was modified to include the effect of plant drag within vegetation canopies at fine-scales. This last version has been extensively validated against field and wind-tunnel measurements over homogeneous canopies (Dupont and Brunet, 2008b), over simple forest-clearing-forest patterns (*e.g.*, Dupont and Brunet, 2008a; Dupont et al., 2011), over a forested hill (Dupont et al., 2008), and over a waving crop (Dupont et al., 2010). The code is based on a three-dimensional, non-hydrostatic compressible model and terrain-following formulation of the NS-equations. The model allows to solve conservation equations for the three wind velocity components, pressure, potential temperature and water substance (water vapour, cloud water, rainwater, cloud ice, snow and graupel). Wind components and atmospheric state variables (air density, pressure and potential temperature) are split into a base state (represented by hat variables) and a deviation (starred variables), *i.e.* $\phi = \hat{\phi} + \phi^*$. The base state is assumed horizontally homogeneous, time invariant and hydrostatically balanced. It is used in ARPS to prescribe initial fields, or to apply a forcing of the flow. The filtered LES equations in the code are formulated as presented in Section 2.3.1 to 2.3.3, except that they include the base state and the deviation splitting of the variables, and that buoyancy is kept solved in all simulations, even if the flow is assumed neutral. The reader can refer to the ARPS User Manual (Xue et al., 1995) and to Xue et al. (2000, 2001) for more details and for validation cases.

2.4 Canopy structure theory

For wind modeling, a formal description of the individual characteristics of canopy elements is too complex. Actual canopies found in nature have variable properties at various scales, and the flow is impossible to solve directly around each individual plant part. An averaged description of the canopy structure eliminating small-scale randomness is therefore required. In the computational grid, the canopy structure is stored using the three-dimensional frontal area density introduced in Eq. 2.12. To describe the values of a in simplified volumes around each grid point, vertically aligned cylinders are considered, as they show an equal weighting to all wind directions. The three-dimensional frontal area density is difficult to use directly for validation and visualisation, simpler descriptors are needed. The tree height and plant area index (or the vertically summed frontal area density over the canopy height), are useful parameters to describe the forest properties.

While providing the terrain level information, a LiDAR can also be used to retrieve the canopy structure. However, the frontal areas from each canopy elements cannot be directly retrieved and averaged from an aerial LiDAR scan. A probabilistic description using radiation transfer properties of the forest media is still needed. For this task, the decay of light inside canopies was found to be strik-

ingly linked to the Beer-Lambert law following the observations of Monsi and Saeki (2005). This relationship proved useful, as it can relate the light attenuation to the structural property of the forest media. The forest properties descriptors, the G-function and the Beer-Lambert law used in the LiDAR method (see Chapter 3) are introduced in this section.

2.4.1 Tree height

The *tree height*, denoted by h_{max}, is defined as the vertical distance between the uppermost point on the canopy to the lowermost point on the ground.

2.4.2 Frontal area density

The *frontal area density*[1] $a(x, y, z)$

$$a(x, y, z) = \frac{1}{V(P)} \sum_{i=1}^{n} A_i, \tag{2.36}$$

is defined as the sum of all n frontal areas A_i of each ith canopy elements inside a volume $V(P)$, centred around a point $P(x, y, z)$. $V(P)$ is here represented with a vertically aligned cylinder.

The projected frontal area density $a^*(x, y, z, \theta, \phi)$ is defined as

$$a^*(x, y, z, \theta, \phi) = a(x, y, z)G(\theta, \phi), \tag{2.37}$$

where the function $G(\theta, \phi)$ is an operator establishing the dependence of the frontal area density $a(x, y, z)$ on both, the orientation of the canopy elements and a given projection direction (see Section 2.4.4).

2.4.3 Plant area index

The *downward cumulative plant area index*, or PAI, is defined as

$$PAI(x, y, z, \theta, \phi) = \int_{z}^{h_{max}} a^*(x, y, z, \theta, \phi) \mathrm{d}z, \tag{2.38}$$

and represents the projected frontal area of canopy elements $a^*(x, y, z, \theta, \phi)$ from the top of the canopy, per unit horizontal surface area at a height z. Followingly, the $PAI(x, y, \theta, \phi)$ is the total projected frontal area per unit ground area over the whole canopy height ($z = 0$).

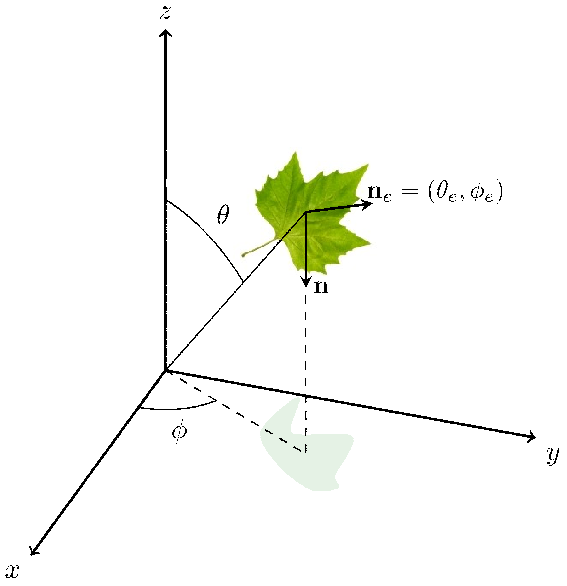

Figure 2.1: Geometry of the projection of a canopy element area (here onto the horizontal plane $x-y$).

2.4.4 G-function

The *G-function* (Ross, 1981) is an operator used for projecting the averaged area of canopy elements onto a surface perpendicular to the normal direction of the projection vector $\mathbf{n}$ (see Fig. 2.1). It is defined as

$$G(\theta,\phi) = \int_{\Omega_H} \frac{g(\mathbf{n}_e)}{2\pi} |\cos(\mathbf{n}\cdot\mathbf{n}_e)| \mathrm{d}\Omega_e, \tag{2.39}$$

where

$$\cos(\mathbf{n}\cdot\mathbf{n}_e) = \cos\theta\cos\theta_e + \sin\theta\sin\theta_e\cos(\phi-\phi_e), \tag{2.40}$$

with θ and ϕ, the zenith and azimuth angles, respectively, and where

$$\mathrm{d}\Omega_e = \sin\theta_e \mathrm{d}\theta_e \mathrm{d}\phi_e, \tag{2.41}$$

is the solid angle containing the canopy elements' surface normals $\mathbf{n}_e = (\theta_e, \phi_e)$ within the upper unit hemisphere Ω_H. The distribution function of the canopy elements' surface normals $g(\mathbf{n}_e)/2\pi$ sastisfies

$$\int_{\Omega_H} \frac{g(\mathbf{n}_e)}{2\pi} \mathrm{d}\Omega_e \equiv 1. \tag{2.42}$$

[1]The frontal area density denomination is here equivalent to the plant area density.

The distribution function is assumed to be the same at every point P of the forest media (xyz independent). Mathematically, the G-function sums the projections of the canopy elements surface normals falling within the solid angle $\mathrm{d}\Omega_e$ onto a plane perpendicular to the normal direction $\mathbf{n}$. Several approximations for $G(\theta, \phi)$ could be assumed from ideal distributions of $g(\mathbf{n}_e)$ (see *e.g.* Chen and Black, 1992). Here, a uniform or spherical distribution of the canopy element orientations with $g(\mathbf{n}_e) = 1$ is assumed for simplicity (Nichiporovich, 1962). This assumption is tested in Chapter 3. Projecting the average frontal areas in the direction $\mathbf{n}$ normal to the horizontal plane $x - y$ (see Fig. 2.1), and integrating the canopy elements normals $\mathbf{n}_e$ over the upper unit hemisphere Ω_H, $G(\theta, \phi)$ becomes

$$G(\theta) = \cos\theta \cdot \frac{1}{2\pi} \int_0^{2\pi} \mathrm{d}\phi_e \int_0^{\frac{\pi}{2}} \cos\theta_e \sin\theta_e \mathrm{d}\theta_e = \cos\theta \cdot G = \cos\theta \cdot \frac{1}{2}, \tag{2.43}$$

where the dependence on the azimuth angle is removed by the integration.

2.4.5 Beer-Lambert law

The Beer-Lambert law applied to canopies (Monsi and Saeki, 2005) reads

$$I(z) = I_0 \exp(-\gamma PAI), \tag{2.44}$$

and relates the decay of flux density of light $I(z)$ at a height z inside the canopy, to the incoming intensity I_0 at the top of the canopy. The extinction coefficient of light γ is defined as the ratio between the averaged projected area in the horizontal plane $x - y$, to the averaged canopy element area (Campbell and Norman, 1998). For a light beam radiation coming from the zenith angle θ, it follows from Eq. 2.43 that

$$\gamma = \frac{a^*(x, y, z)}{a(x, y, z)} = \frac{G(\theta)}{\cos\theta}. \tag{2.45}$$

3

LiDAR METHOD

Abstract

The difficulty of obtaining accurate information about the canopy structure is a current limitation towards higher accuracy in numerical predictions of the wind field in forested terrain. The canopy structure in computational fluid dynamics is specified through the frontal area density, and this information is required for each grid point in the three-dimensional computational domain. By using raw data from aerial LiDAR scans, together with the Beer-Lambert law, we propose and test a method to calculate and grid highly variable and realistic frontal area density input. An extensive comparison with ground-based measurements of the vertically summed frontal area density (or plant area index) and tree height, was used to optimize the method, both in terms of plant area index magnitude and spatial variability. The resolution of the scans was in general low (< 2.5 reflections$\,\mathrm{m}^{-2}$). A decrease of the resolution produced an increasing systematic underestimation of the spatially averaged tree height, whereas the mean plant area index remained insensitive. The gridded frontal area density and terrain elevation were used at the lower boundary of wind simulations in a 5×5 km^2 area of a forested site. The results of the flow simulations were compared to wind measurements using a vertical array of sonic anemometers. A good correlation was found for the mean wind speed of two contrasting wind directions with different influences from the upstream forest. The results also predicted a high variability on the horizontal and vertical mean wind speed, in close correlation with the canopy structure. The method is a promising tool for several computational fluid dynamics applications requiring accurate predictions of the near-surface wind field.

This chapter has been accepted for publication as: Boudreault, L.-E., Bechmann, A., Tarvainen, L., Klemedtsson, L., Shendryk, I., and Dellwik, E. (2014b). A LiDAR method of canopy structure retrieval for wind modeling of heterogeneous forests. *Agricultural and Forest Meteorology.* Accepted.

3.1 Introduction

In computational fluid dynamics (CFD) simulations of complex forested terrain, imposing the correct canopy structure at all spatial scales is crucial to reduce the modeling uncertainty (Lopes Da Costa et al., 2006). In the vicinity of the trees, the flow is affected by the canopy elements and the horizontal and vertical variability in forest density. At larger scales, natural and man-made heterogeneities cause the flow to be in constant adaptation to the surface. It has been shown that the flow in and over the heterogeneities is closely correlated with the density of the forest (Schlegel, 2012; Dellwik et al., 2014). Several CFD applications require high accuracy numerical predictions of forest flows. These include wind energy assessments (Lopes Da Costa et al., 2006; Ayotte, 2008), aerosol dispersion (Katul and Poggi, 2010), wildfire propagation (Coen, 2005; Sun et al., 2009), carbon dioxide exchange between forests and atmosphere (Belcher et al., 2012), and wind damage on trees (Dupont and Brunet, 2006). In this study, a method to obtain the forest canopy structure using aerial light detection and ranging (LiDAR) scans (ALS) for CFD is presented and evaluated.

In wind modeling, the effect of the forest is often parameterized using drag forces in the momentum equations (see *e.g.* Finnigan, 2000). Additional source terms are generally prescribed in a turbulence model to account for the modification of the turbulence length or velocity scale inside the canopy. In the Reynolds-averaged Navier-Stokes (RANS) canopy model proposed by Sogachev and Panferov (2006); Sogachev (2009), the drag terms S_d and the source term S_ϵ in the dissipation equation read

$$S_d = -C_d a |u| u_i, \tag{3.1}$$

$$S_\epsilon = 12 C_\mu^{1/2} C_d a |u| k, \tag{3.2}$$

where u (in $\mathrm{m\,s^{-1}}$) is the mean velocity vector, k (in $\mathrm{m^2\,s^{-2}}$) is the turbulent kinetic energy (TKE), C_d is the drag coefficient and a (in $\mathrm{m^2\,m^{-3}}$), the frontal area density. The frontal area density represents the area of leafs, branches and stems opposing the wind flow per unit volume. Two parameters, C_d and a, are required as input. C_d is often assigned using approximations based on measurements (see *e.g.* Pinard and Wilson, 2001; Queck et al., 2012). The canopy structure enters as an input through a.

Different methods can be considered for the determination of a (Jonckheere et al., 2004; Weiss et al., 2004). They can be classified as direct and indirect (Bréda, 2003). The direct methods consist of destructive sampling of trees, whereas indirect methods relate the forest density to the light absorption and the optical properties of canopies (Morsdorf et al., 2006). In wind modeling, performing labor-intensive, ground-based tree height and density distribution

measurements is technically impracticable as the forest properties are needed for extended areas. Therefore, the canopy structure is often simplified in flow models and parameterized based on few measurements only. This can severely degrade the overall accuracy of the wind simulations. Thus, indirect methods such as the ALS technique are potentially useful for determining stand structure for applications requiring high accuracy description over extended areas.

An ALS is performed using an aircraft with a combined LiDAR and global positioning system (GPS) (*e.g* El-Sheimy et al., 2005). The x,y and z positions, where the reflection of each LiDAR pulse occurs, form a so-called point cloud. In addition to the terrain elevation, the beam penetration gives information about the structure of the canopy. Several forest attributes can be recovered from the point cloud (see van Leeuwen and Nieuwenhuis, 2010, for review). These include, for example, tree height (*e.g* Popescu and Wynne, 2004; Mcinerney et al., 2010) and plant area index (PAI) (*e.g* Lefsky et al., 1999; Morsdorf et al., 2006; Solberg et al., 2006, 2009; Richardson et al., 2009). Although a has not previously been derived from the point cloud, a few studies have included the vertical distribution of the LiDAR reflections for determining the canopy structure (*e.g* Coops et al., 2007; Peduzzi et al., 2012). A good agreement was generally found between the ALS-derived properties and ground-based measurements in the various studies mentioned. However, the focus was put on a few local point validations and no systematic method to produce grid estimates of a useful for CFD input has been proposed so far. In the present study, we propose such a method. An extensive grid validation with ground-based tree height, PAI and a at various spatial scales was also performed. Today, ALS scans are becoming increasingly widespread and accessible, but the scans are often performed at low resolutions. We further explore how scanning resolution affects the forest description in the grid estimates of a. The scanning resolution was defined as the reflection density of LiDAR pulses per unit ground area (in reflections$\,\mathrm{m}^{-2}$).

The paper is divided into two major topics: (1) a method to organize ALS data into a 3D canopy structure input is proposed and validated and; (2) wind results are presented for a complex forested site located in Sweden where the input was coupled to a CFD model. For the first time, a large-scale numerical reconstruction of the 3D mean wind field for an actual forested site using a small-scale canopy structure description is presented.

3.2 LiDAR method of canopy structure retrieval

3.2.1 Forest description

A three-dimensional description of $a(x,y,z)$ is considered. However, performing an extensive validation of $a(x,y,z)$ using a direct comparison with ground-based measurements is a difficult task to perform. For this reason, simpler forest parameters such as the tree height h_{max} (in m) and PAI (in $\mathrm{m}^2\,\mathrm{m}^{-2}$) were used for comparison. The tree height was defined here as the height difference between highest vegetation point above the ground and the lowest point on the ground within a given area. The PAI was a reduced two-dimensional variable of the three-dimensional distribution of $a(x,y,z)$ defined as:

$$PAI(x,y) = \int_0^{h_{max}} a(x,y,z)dz \tag{3.3}$$

and represents the projected canopy element area per unit ground surface area. Here, $a = a(x,y,z)$ and $PAI = PAI(x,y)$ include all possible canopy elements opposing the wind flow, *i.e.* leafs, branches and stems.

3.2.2 Mathematical model

The ALS data was gathered as a point cloud, i.e. a set of reflections having x,y and z spatial coordinates (Fig. 3.1d). The Beer-Lambert law as a function of PAI was first introduced by Monsi and Saeki (2005)[2]. Extending its definition to $a(x,y,z)$ we get:

$$I(x,y,z) = I_0 \exp\left[-\gamma(\theta) \int_z^{h_{max}} a(x,y,z)dz\right] \tag{3.4}$$

where the incoming light of intensity I_0 a the top of the canopy decays exponentially to a I value within the canopy. Assuming a spherical distribution of the canopy element surface angles, the extinction coefficient $\gamma(\theta)$ was given by:

$$\gamma(\theta) = \frac{0.5}{\cos\overline{|\theta|}_{LiDAR}} \tag{3.5}$$

where $\overline{|\theta|}_{LiDAR}$ is the mean zenith angle of the LiDAR (Richardson et al., 2009). Using so-called voxels of a vertically discretized volume (or bin) (*e.g.* Fig. 3.2a), a

[2]Article from the same authors translated from a German version originally published in 1953.

relationship for a_k values into a k^{th} layer of thickness Δz can be directly obtained from Eq. 3.4. Assuming that the incoming and outgoing intensities $I_0 = I_{k-1}$ and $I = I_k$ could be obtained from the count of the intercepted LiDAR pulses R_i inside the k^{th} layer, a_k reduces to:

$$a_k = -\frac{1}{\gamma(\theta)\Delta z} \ln\left(\frac{I_k}{I_{k-1}}\right), \quad \text{where} \quad \begin{cases} I_k = 1 - \sum_{i=1}^{k} R_i/R_0 \\ I_{k-1} = 1 - \sum_{i=1}^{k-1} R_i/R_0 \end{cases} \tag{3.6}$$

and R_0 is the total number of reflections counted inside a given bin.

3.2.3 Gridding algorithm

The proposed LiDAR method was based on a local binning procedure (see *e.g.* El-Sheimy et al., 2005). A uniform grid of $\Delta x = \Delta y$ spacing in the horizontal was defined where cylindrical bins of variable radius r were created around each grid point (the blue shaded area in Fig. 3.2b illustrates the grid arrangement). Each of the individual bins was discretized in the vertical by defining layers of Δz thickness. Ground and vegetation reflections were separated into two distinct data sets according to a method defined in Evans and Hudak (2007). Using Eq. 5.2, the number of vegetation reflections R_i contained inside each Δz layers was then used to calculate the vertical distribution of a. A LiDAR beam may undergo multiple reflections when a pulse is emitted and reflected. Here, we only considered the first LiDAR reflections to be consistent with the definition of the Beer-Lambert law. The terrain height in each bin was set with the lowest first ground reflection. Last ground reflections could have been used to specify the terrain level but no significant difference were found on the tree height estimates for the considered point cloud. For the grid positions ij in the $x-y$ plane, the effective PAI (PAI^{ij}_{eff}) was defined as the cumulative sum of each a^{ij}_k voxels contained inside a given bin, given as:

$$PAI^{ij}_{eff} = \sum_{k=1}^{n_h} a^{ij}_k \Delta z\,, \quad \text{where} \quad n_h = ||h^{ij}_{max}/\Delta z||. \tag{3.7}$$

The PAI_{eff} denotes the raw PAI without any corrections applied.

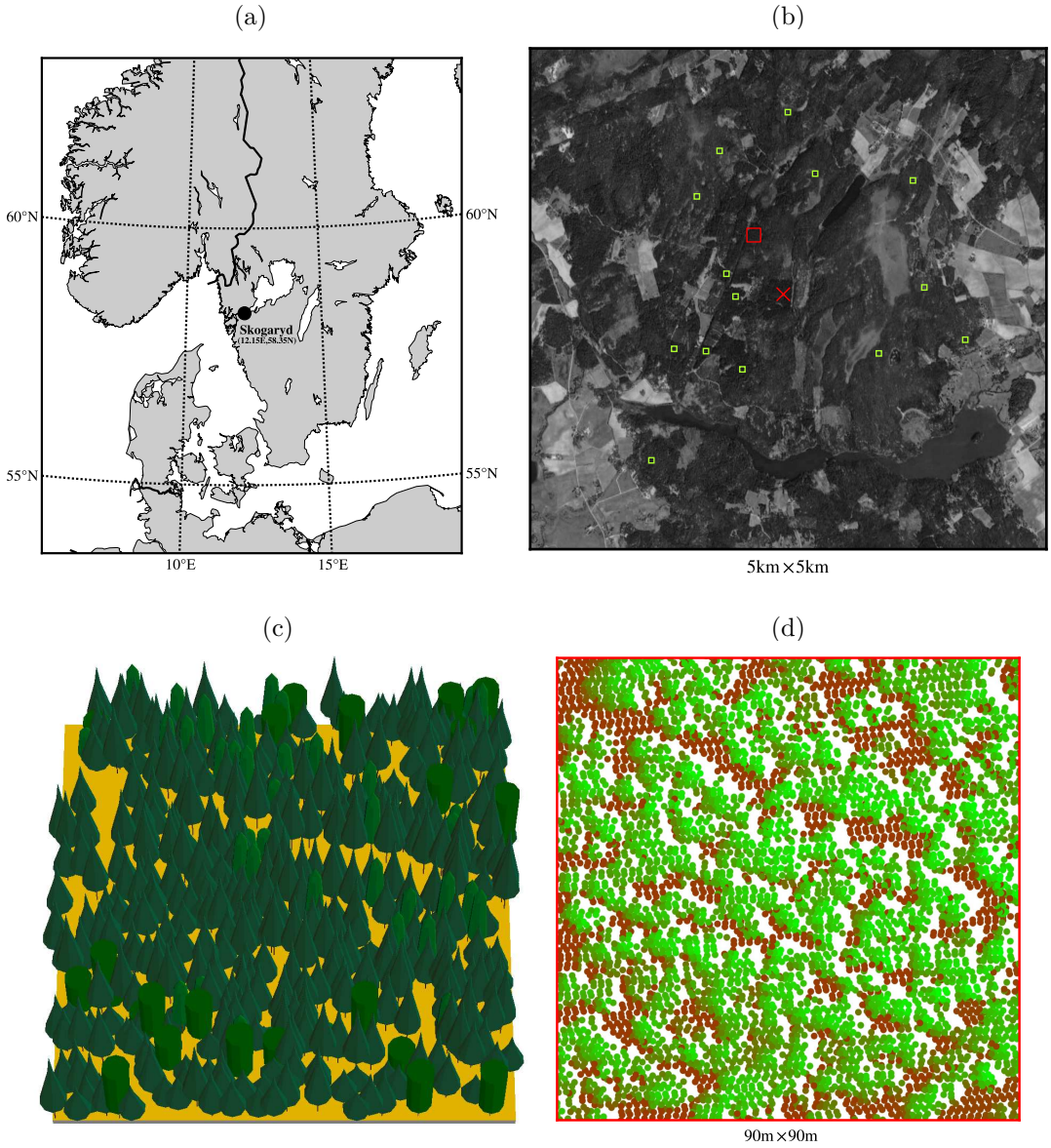

Figure 3.1: (a) Map of Sweden and neighbouring countries where the location of the study site is shown by the black dot. (b) Aerial photo of the study site investigated, where the red "×" marker in the centre of the domain indicates the mast location. The green square markers indicate the locations of the areas in *Inventory B*. The red square indicates the location of the *Inventory A* area. (c) Illustration of the stand in the *Inventory A* area in which the forest properties were calibrated and validated. Tree height, locations and species are represented in the figure (large-base cones: *Picea abies*, elongated cones: *Pinus sylvestris*, cylinders: *Betula pendula*). The crown shape is not to scale. (d) Raw point cloud distribution of *xyz* coordinates from the aerial LiDAR scans for the *Inventory A* area. The points in brown color indicate the ground reflections whereas the points in green, the vegetation reflections.

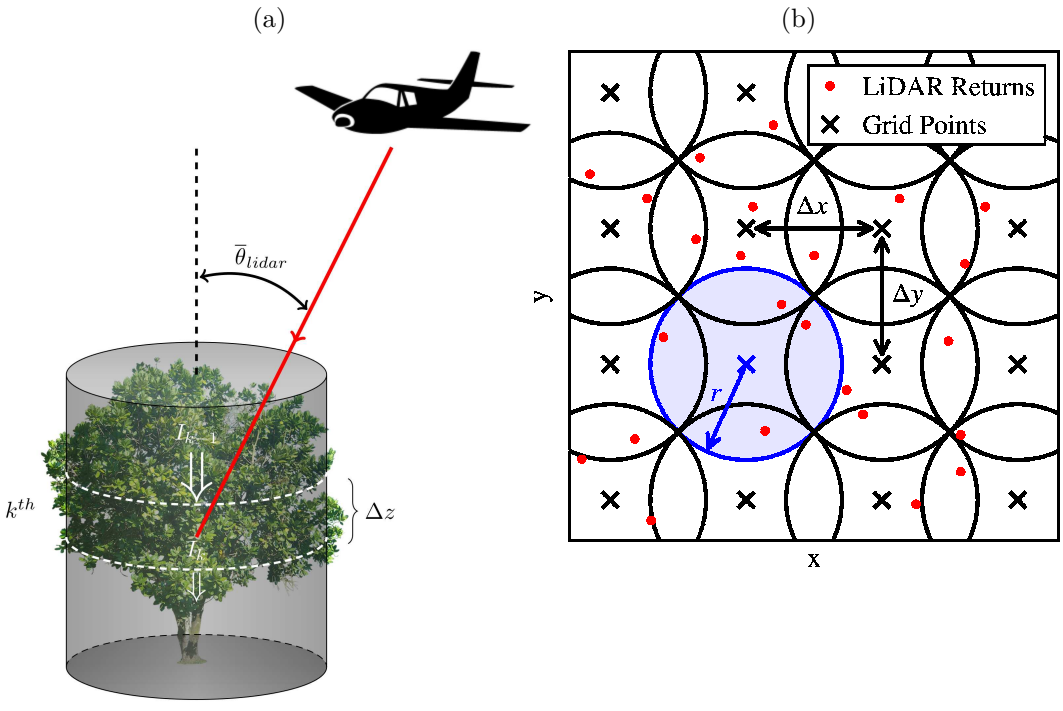

Figure 3.2: (a) Sketch of the cylindrical volume, or bins, containing voxel slices of Δz thickness. The red line illustrates an incoming LiDAR beam where $\overline{\theta}_{LiDAR}$ is the mean zenith angle of the beams inside a given Δz thick voxel. (b) Illustration of the binning procedure viewed from the top for an equidistant grid of $\Delta x = \Delta y$. The bin radius r in this image was arbitrarily chosen.

3.3 Test site and experimental method

3.3.1 Site description

The LiDAR method was implemented and tested on a 5×5 km^2 area, centered around the Skogaryd Research Catchment[3] (58°21′50.5”N, 12°8′59.4”E). The site is located $\simeq 50$ km from the west coast of Sweden (Fig. 3.1a). The ALS was produced by the National Land Survey of Sweden in the context of the Swedish national digital elevation model project. The scans were performed from 3 to 4 June 2011 and had a mean scanning resolution of 1.42 reflections m^{-2} for the whole area. The area is predominantly covered by coniferous forest, but also contains areas of low-crop agriculture. Two tall installations were present on the site, a mast and a scaffold tower.

3.3.2 Wind measurements

The 38-m-tall mast was the basis for the wind experiment. The mast was equipped with six sonic anemometers (Metek USA-1 Basic), which were mounted at 1.2, 6.5, 12.5, 18.5, 31.0 and 38.4 m above the local ground level. For the levels below the canopy top, the instruments were not closer than $\simeq 1$ m from the nearest branch. The measurement campaign lasted from 19 August 2010 to 25 October 2011. The forest immediately surrounding the mast was an $\simeq 50$-year-old forest dominated by Norway spruce (*Picea abies*). The local forest height h_c was estimated to be 24 to 28 m near the mast. Data were sampled at 20 Hz and averaged over 30 min. The Metek sonic anemometer data were corrected for flow distortion and treated the same way as described in Bechmann et al. (2009). The friction velocity and Monin-Obukhov lengths L were calculated as in Dellwik et al. (2014). The selection for near-neutral data was based on two criteria: $(z_{ref} - d)/|L_{ref}| < 0.05$ and $u_{38m} > 4.5$ m s^{-1}, where $z_{ref} = 38$ m denotes a reference height above terrain, L_{ref} the Monin-Obukhov length at the reference height z_{ref}, $d = 0.75 h_c \approx 20$ m was the assumed displacement height and u_{38m} the mean wind speed in the mean wind direction at $z = 38$ m. For the CFD model validation, we focused on the eastern and western wind directions, which had contrasting upstream vegetation density and terrain. A total of 222 samples centered around the 270° sector and 58 samples around the 90° sector were taken on a 30° wide angle.

[3] A research station within the Swedish Infrastructure for Ecosystem Research Science, SITES (www.fieldsites.se).

3.3.3 Inventory A area

The 24-m-tall scaffold tower is located about 600 m to the northwest of the mast (Fig. 3.1b, red square). In October 2010, detailed measurements of tree height and PAI were performed for a relatively homogeneous 90×90 m^2 area centered around the tower. This area was denoted as the *Inventory A* area. All trees in *Inventory A* were classified into species and status (alive or dead). There were 515 trees in the area (450 × *Picea abies*, 42 × *Pinus sylvestris* and 23 × *Betula pendula*). Tree height measurements were taken for each of the 515 trees using a Vertex IV inclinometer (Haglöf, Långsele, Sweden), with an instrumental uncertainty of ±0.1 m (Vertex IV, 2007). The distribution and location of the trees were mapped (Fig. 3.1c) using Stand Visualization System software. For comparison, the ALS data for this area are also shown (Fig. 3.1d).

3.3.4 Ground-based measurements of PAI

The PAI measurements in *Inventory A* were taken with a plant canopy analyzer (PCA) (LAI-2000, LI-COR, Inc., Lincoln, Nebraska). The PCA was used in its two-sensor and five rings mode with 45° view caps on both sensors. The reference sensor was mounted at 25 m on top of the scaffold tower and set to measure once every 15 s. The measurements from the sensor inside the canopy were taken at breast height ($z = 1.3$ m). The PAI_{eff} values were recorded once every 6 m in a 16×16 equidistant horizontal grid (256 measurements). The vertical distribution of PAI_{eff} was also measured at different heights on the tower: 2, 11, 15, 19 and 23 m. The measurements of the vertical PAI_{eff} variation were made using 180 degree view caps.

3.3.5 Inventory B areas

A similar inventory denoted *Inventory B*, consisting of 15 randomly selected 15×15 m^2 areas (Fig. 3.1b, green squares), was made between 26 June and 27 August 2012 (see also Shendryk et al., 2014). The height of all trees was measured using the Vertex IV inclinometer, but the PAI was not measured. Compared with the *Inventory A* area, the fifteen areas contained more variability in stand age and height. The mean stand density for all 15 areas was 0.0877 tree m^{-2}.

3.3.6 Forest growth

To account for the time difference of $\simeq 1$ year between the tree height measurements in the *Inventory B* areas and the ALS data, the ALS-based estimates were corrected for growth. Based on local field observations, 0.4 m was added to the tree

height results of the ALS. The growth was neglected for the comparison between the ALS data and the data taken in *Inventory A*. This assumption was based on the shorter gap between the time the ALS and the inventory measurements were acquired (≈ 8 months) and the reduced growth rate during the winter season.

3.4 CFD model

3.4.1 Model details

The CFD model was based on a neutrally stratified RANS analysis using the standard $k-\epsilon$ model (Jones and Launder, 1972). The source terms S_d and S_ϵ in Eqs. (3.1) and (3.2) were added to the $k-\epsilon$ equations to model the effect of the canopy (Sogachev and Panferov, 2006; Sogachev, 2009). The drag coefficient in the source terms was set to $C_d = 0.2$. The $k-\epsilon$ equations in the form used can be found in Wilcox (2006) where the constants of the model were set to $C_\mu = 0.06$, $\kappa = 0.4$, $\sigma_k = 1.0$, $\sigma_\epsilon = 2.1$, $C_{\epsilon 1} = 1.52$ and $C_{\epsilon 2} = 1.83$. The Coriolis force was added to the momentum equations and a length-scale limiter was added to limit the growth of the modeled mixing length following Apsley and Castro (1997). The maximum length scale l_{max} in the limiter was prescribed using the relationship of Blackadar (1962):

$$l_{max} = 0.00027G/f_c \tag{3.8}$$

where G is the geostrophic wind and $f_c = 1.2 \times 10^{-4}$ is the Coriolis frequency.

3.4.2 Domain and grid specifications

The domain specification in the following description is illustrated in Fig. 3.3. A box-type computational grid having a 50 km length and 20 km width centred on the mast location was used. The computational grid had an equidistant $x-y$ resolution of 10 m near the domain centre. The grid cells were stretched towards the exterior boundaries. A hyperbolic mesh generator (Sørensen, 1998) was used to make a three-dimensional volume grid. The domain height was set to 4 km with a vertical near-wall resolution of 0.03 m, from where it was expanded to a resolution of about 1 m at a 30 m height above the ground. Simulation tests indicated that the numerical solution was sufficiently grid-independent. Based on measurements made at the site (see Section 3.5.1 for details), a 5×5 km^2 forest grid was generated from the ALS, as described in Section 3.2, using a bin radius of $r = 10$ m, a grid spacing of $\Delta x = \Delta y = 10$ m and layers of $\Delta z = 1.0$ m thickness. The forest grid was interpolated in the central area of the CFD grid. Inside the forested area, a roughness height of $z_0 = 0.1$ m was used at the ground boundary

below the canopy. Outside this area, a roughness of $z_0 = 1.5$ m was set to reproduce appropriate farfield conditions.

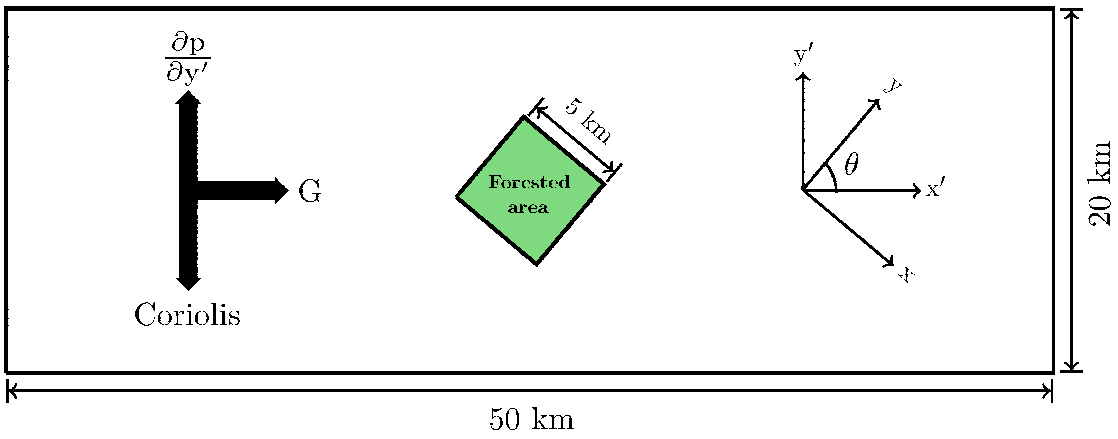

Figure 3.3: Sketch of the computational domain and the forcing setup of the simulations. A geostrophic wind is imposed from the balance of a lateral pressure gradient and the Coriolis force. The forcing is set such that the simulated wind velocity is oriented in the direction of the measured wind velocity at $z = 38$ m AGL (in the $x - y$ the reference frame).

3.4.3 Numerical setup

The set of model equations were solved using the EllipSys3D flow solver (Michelsen, 1992, 1994; Sørensen, 1995). The Leonard's third-order accurate QUICK scheme (Leonard, 1979) was used on the advective operators and the standard second-order central difference scheme was used for all remaining terms. Periodic conditions were used on all the vertical boundaries and symmetry conditions (zero normal gradients) were used at the top boundary. Standard log-law wall functions were applied at the ground boundary, as described in Sørensen (1995). The flow was forced with a lateral pressure gradient equivalent to the Coriolis force to simulate a geostrophic wind G. The forest grid and the terrain were horizontally rotated with an angle θ such that the wind vector at 38 m above ground level (AGL) was aligned with the desired wind direction at the mast location. The magnitude of G was imposed at the top boundary such that the calculated mean wind speed at 38 m AGL was matching the measured wind speed magnitude at the mast location.

3.5 Results

In this section, the tree height and PAI obtained using the LiDAR method proposed (Section 3.2) is first compared with ground-based measurements. Second,

results of CFD simulations using the method are presented. The simulations were performed for western and eastern wind directions to highlight asymmetric influence of the canopy structure on the wind field.

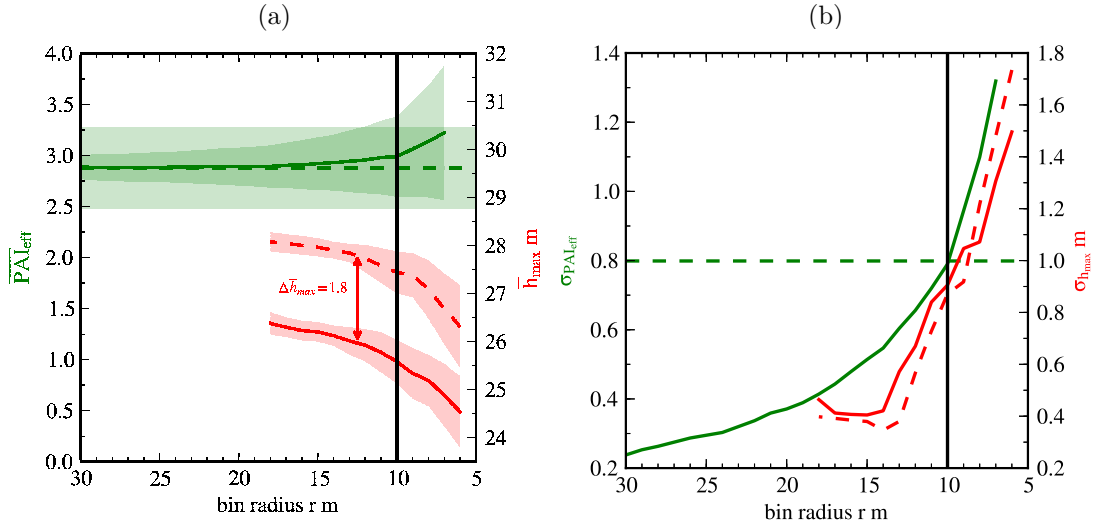

Figure 3.4: Variation of: (a) mean values and (b) standard deviations of plant area index and tree height with the bin radius r for the PCA and ALS grids in *Inventory A* area. The dash lines indicate the results from the PCA grid and the plain lines, the results from the ALS grid. The vertical plain black line indicates the bin radius chosen in the analysis ($r = 10$ m). The shaded areas in (a) shows the extent of the standard deviation around the mean.

3.5.1 LiDAR method validation

An unknown to be determined in the LiDAR method was the correct bin radius r (see Section 3.2.3). The PCA and ALS data were therefore assembled into grids and a statistical comparison of h_{max} and PAI_{eff} in *Inventory A* was performed. For the ALS grid, the thickness of the layers Δz in the bins were kept fixed to a value of $\Delta z = 1.0$ m. The first near-ground layer in the PAI_{eff}^{ALS} determination was excluded to be consistent with the PCA measurements, which were taken at breast height ($z = 1.3$ m). The ALS data was arranged in a grid having the same specifications in terms of $x-y$ grid point positions and spacing ($\Delta x = \Delta y = 6$ m), as the grid defined for the PCA data (Section 3.3.3). This grid was denoted the 16×16 grid. For h_{max}, the grid was reduced with a 18 m $x-y$ offset so that the bin radius does not exceed the area where the tree height data was recorded. For this reason, the h_{max} grid had fewer grid points and the maximum bin radius was limited to $r = 18$ m. This grid was denoted the 10×10 grid.

The bin radius r in the LiDAR method was varied to find the optimal grid value of $\overline{PAI}_{eff}^{ALS}$ matching the grid value of $\overline{PAI}_{eff}^{PCA}$. Both values agreed well for $r > 10$ m (Fig. 3.4a). The standard deviations $\sigma_{PAI_{eff}}$ became equal at $r = 10$ m (Fig. 3.4b). Regardless of the bin radius, $\overline{h}_{max}$ was underestimated compared with the ground-based measurements (Fig. 3.4a) although their variability $\sigma_{h_{max}}$ was similar (Fig. 3.4b). The difference in grid values of $\overline{h}_{max}$ for all r was $\Delta\overline{h}_{max} =$ 1.8 m. Because the PAI as measured with the PCA is a well-known standard and because we aimed for the smallest possible binning area without altering the $\overline{PAI}_{eff}$ estimates, we choose to fix the bin radius to $r = 10$ m. At this value, the same variability of $\sigma_{PAI_{eff}}$ occurred while the $\overline{PAI}_{eff}$ remained comparable. A grid spacing of $\Delta x = \Delta y = 10$ m was chosen as $\overline{PAI}_{eff}^{ALS}$ and $\sigma_{h_{max}}^{ALS}$ did not vary significantly for higher resolutions (not shown).

Using $r = 10$ m, the scatter plot between PAI_{eff}^{PCA} and PAI_{eff}^{ALS} (Fig. 3.5a) showed a low correlation ($r^2 = 0.176$) and a root mean square error of $R = 0.864$, although the grid values of $\overline{PAI}_{eff}$ were comparable ($\overline{PAI}_{eff}^{ALS} = 2.98$ and $\overline{PAI}_{eff}^{PCA} =$ 2.88). To investigate if a stronger correlation was present for larger averaging areas, the 16×16 grids were averaged and aggregated on coarser 8×8 grids (Fig. 3.5b). The result showed an increased $r^2 = 0.336$ and a diminished $R = 0.591$. The tree height scatter (Fig. 3.5c) clearly indicated an overall underestimation ($\Delta\overline{h}_{max} = 1.85$ m) by the LiDAR method compared to ground-based measurements. The correlation was low ($r^2 = 0.344$), but this was mainly due to the limited range of tree height values present in this specific area. To verify if a better correlation was present over a greater range of values taken in various areas, maximum tree heights derived from the ALS were compared with the maximum tree heights measured in *Inventory B* (Section 3.3.5, Fig. 3.5d). An improved correlation was obtained ($r^2 = 0.901$) with an overall tree height underestimation of $\Delta\overline{h}_{max} = 2.04$ m.

An analysis was performed to determine whether the statistical properties of the ALS grid were changing with different scanning resolutions. A scanning resolution map for the 5×5 km^2 area is presented (Fig. 3.6a). The figure shows higher-resolution areas in the point cloud due to overlapping scans in the flight paths. The *Inventory A* area was located in a low-scanning-resolution area ($\approx$ 0.6 reflections m^{-2}). Four different areas of 200×200 m^2 showing the highest scanning resolution were analyzed. The locations of these areas are indicated by black squares (Fig. 3.6a). The scanning resolution in these respective areas was intentionally lowered by successively removing every second pulse. The result is shown for four different resolutions (Fig. 3.6b). For all areas combined, the average lowest to highest resolutions were 0.3, 0.6, 1.2 and 2.5 reflections m^{-2}. For the resolutions of 0.3, 0.6 and 1.2 reflections m^{-2}, the average tree height respectively differed by 9.3, 5.1 and 2.1 % from the average tree height calculated using

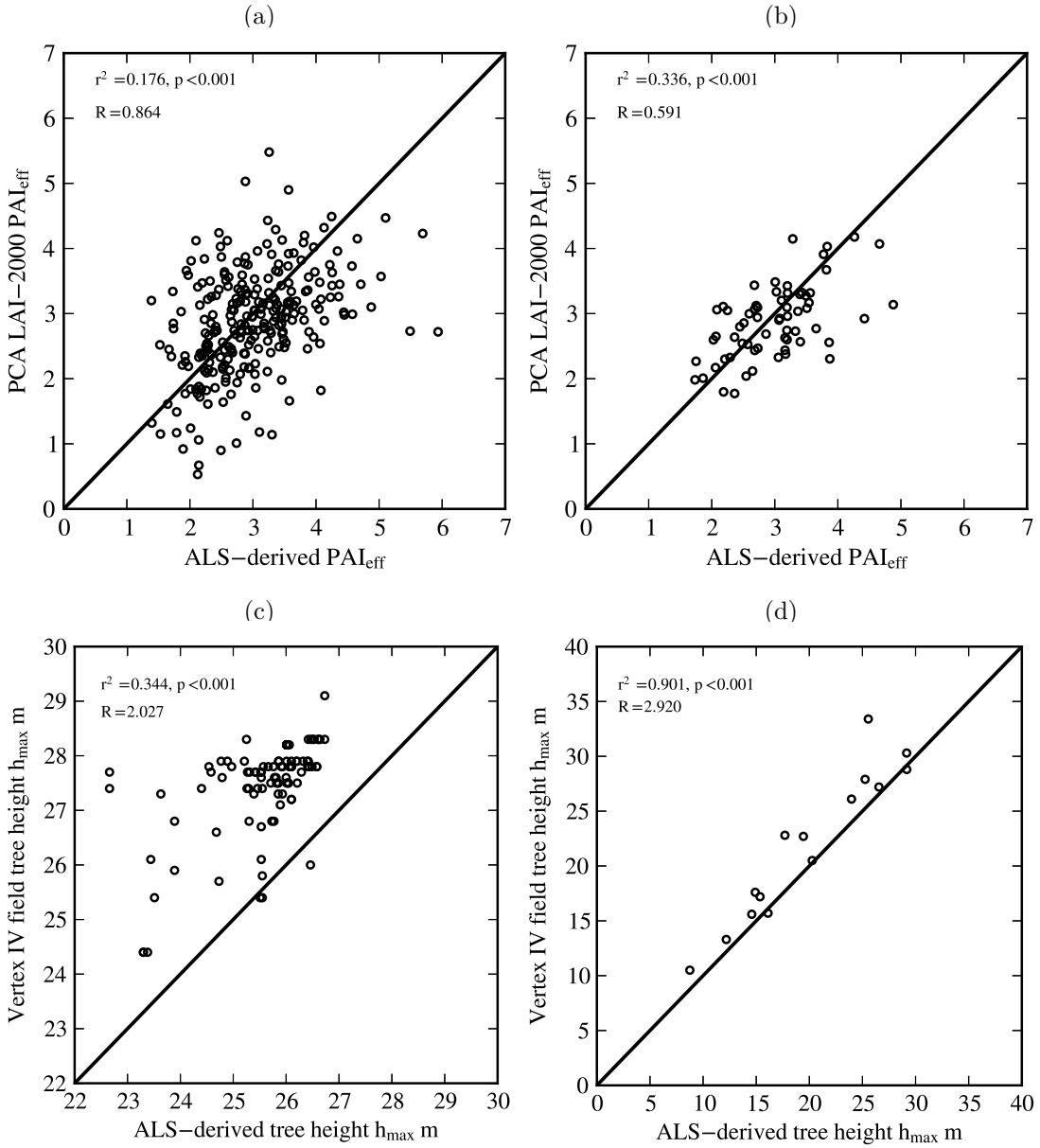

Figure 3.5: Scatter plots between the ALS and PCA grids in the *Inventory A* area: (a) plant area index for 16×16 grids (6 m resolution), (b) plant area index for 8×8 aggregated grids (12 m resolution) and, (c) tree height for 10×10 grids (6 m resolution). (d) Scatter plot of tree height for the *Inventory B* areas. The plain black line shows the 1:1 relationship.

the highest resolution (2.5 reflections m^{-2}). The calculated values of $\overline{PAI}_{eff}$ differed on average by 1.7 % between the lowest and the highest resolutions of 0.3 and 2.5 reflections m^{-2}. The tree height was therefore more sensitive than the

$\overline{PAI}_{eff}$ to the scanning resolution. These results indicated that even with relatively poor scanning resolution, a good description of $\overline{PAI}_{eff}$ can be achieved. A mean tree height underestimation (≈ 5 %) is however expected in specific areas of the ALS grid exposed to low scanning resolutions. Likewise, the variability $\sigma_{h_{max}}$ and $\sigma_{PAI_{eff}}$ showed a negligible dependence on the scanning density (not shown).

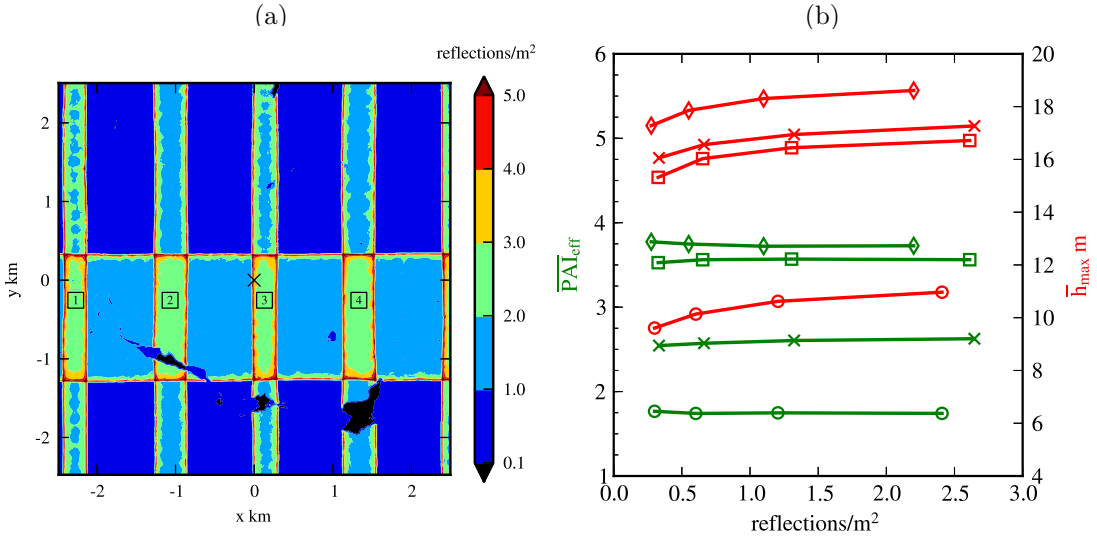

Figure 3.6: (a) ALS scanning resolution map for the Skogaryd 5×5 km^2 area. The "$\times$" black marker indicate the mast location. (b) Variation of the mean plant area index and tree height with the ALS scanning resolution. The markers on the lines indicate the results for area 1 ($\times$), area 2 ($\Diamond$), area 3 ($\square$) and area 4 ($\bigcirc$), as shown in (a).

PCA measurements were taken at several heights in the scaffold tower located in the *Inventory A* area (see Section 3.3.3). A comparison of the PAI_{eff} measured with the PCA and the LiDAR method is shown in Fig. 3.7. In this comparison, the vertically varying PAI at a given height z was defined as:

$$PAI(z) = \int_z^{h_{max}} a(z)dz. \tag{3.9}$$

A single bin centred on the tower location was used to obtain the profile of PAI_{eff}^{ALS}. The PAI_{eff}^{ALS} profile was similar to the profile of PAI_{eff}^{PCA}, but with a small systematic underestimation ($R = 0.49$). The binning area was also increased from $r = 10$ to 15 m and the scanning resolution was lowered from 0.6 to 0.3 reflections m^{-2} inside the bin. Both tests were only affecting the PAI_{eff}^{ALS} estimates in the bottom part of the canopy (4.5% and 10.3% differences at $z = 2$ m respectively, Fig. 3.7).

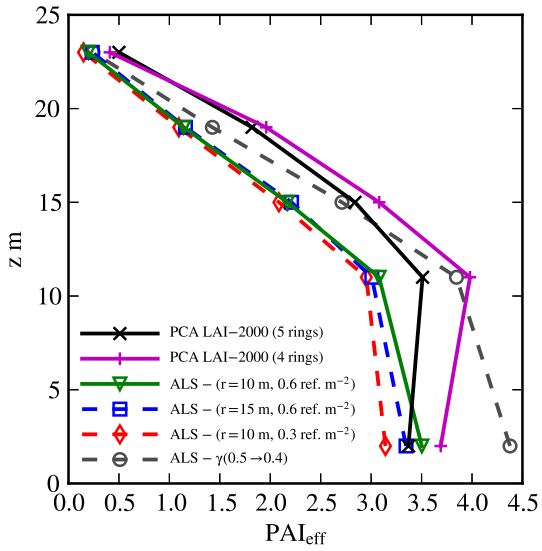

Figure 3.7: Comparison of vertical profiles of plant area index at the tower location in *Inventory A*.

3.5.2 Wind simulation results

In the following results, simulation are shown for the western and eastern wind directions. The magnitude of the velocity vector u at the reference height $z = 38$ m AGL of the mast location was denoted u_{38m}. The x, y and z axes were oriented in the west–east, north–south and vertical directions, respectively (see Fig. 3.3). At the upper boundary, $G = 27.5$ m/s was imposed for the western wind direction and $G = 25.0$ m/s for the eastern wind direction (see Section 3.4). A wind variability as low as ~ 10 m were seen in the $x - y$ plane for the western results (Fig. 3.8). As expected, the wind field variations for the u_x component were in great part influenced by the terrain elevation; but some recognizable forest signatures were observable (Fig. 3.8e, 3.8d). The most evident forest effect was produced by the patch of high PAI and h_{max} in the central part (Fig. 3.8a, 3.8b), where the low wind velocity field was corresponding with the geometry of the patch (Fig. 3.8e, 3.8d). Small and even slightly negative velocities were obtained at $z = 10$ m AGL in the northern part of the area (Fig. 3.8e). The small velocities were present over large distances (≈ 500 m). The combined effect of the low forest density/height and higher terrain elevation (Fig. 3.8a, 3.8b and 3.8c) produced a high velocity field along $y = -400$ m from $-400 < x < 0$ m (Fig. 3.8e, 3.8d). The u_z component was strongly correlated with the canopy structure (Fig. 3.8f). In areas where the terrain effect was not dominating, positive values were observed where the forest was denser and higher than the surrounding environment. An evident example was the north-south row of trees located on the eastern side of the mast ($x = 300$ m, Fig. 3.8b) showing positive u_z components (Fig. 3.8f). Negative values were obtained where the forest was sparser and lower than the surroundings.

Transects of the flow along the black line (in Fig. 3.8) are shown (Fig. 3.9). The raw point cloud data (Fig. 3.9a) showed various clearings (at $x = -140$ m, $x = 20$ m and $x = 110$ m), the height of the trees and the spatial distribution of the trees within the stands. The terrain elevation was fairly flat in this area, except from $125 < x < 200$ m where there is a small hill (Fig. 3.9a). The vegetation was also lower above the hill compared with the mast area (Fig. 3.9a). The a values extracted from the point cloud (Fig. 3.9b) showed regions of high-density crown and low-density trunk space in the western forest patches, as well as dense low trees around $x = 130$ m. For the western wind direction, the flow accelerated over the stand at $25 < x < 110$ m due to west–east decreasing tree height (Fig. 3.9c) and over the hill. The wind was strongly decelerated in the forest patches located at $x > -100$ m. This was significantly different for the eastern wind direction (Fig. 3.9d) where the u_x component was adjusting to the forest only for $x < -50$ m. Small regions of recirculation were observed close to the ground between $100 < x < 200$ m for both wind directions (Fig. 3.9c, 3.9d). These small-scale motions were induced by the large drag due to the high canopy density, the hill-induced adverse pressure

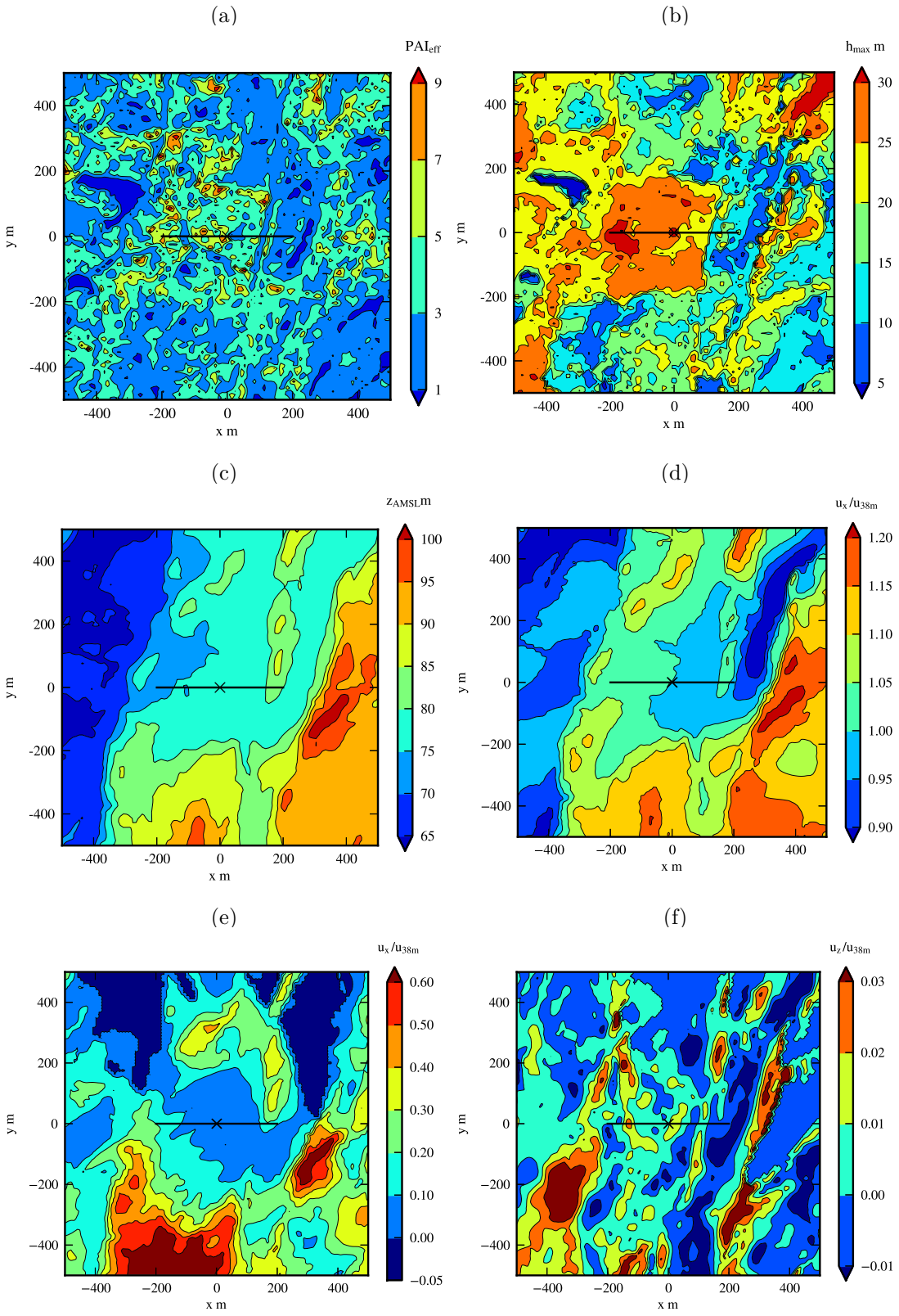

Figure 3.8: Horizontal contours of a 1×1 km^2 area centered around the mast: (a) plant area index, (b) tree height, (c) terrain elevation above mean sea level (AMSL), (d) streamwise velocity component at 38 m AGL, (e) streamwise velocity component at 10 m AGL and, (f) vertical velocity component at 10 m AGL. The flow direction goes from left to right (westerly wind). The velocity magnitude u_{38m} used for normalizing the results was taken at the mast location $(x, y, z = 0, 0, 38)$. The black line located at $y = 0$ shows the extent of the transects presented in Figure 3.9. The mast location is indicated by the black "×" marker.

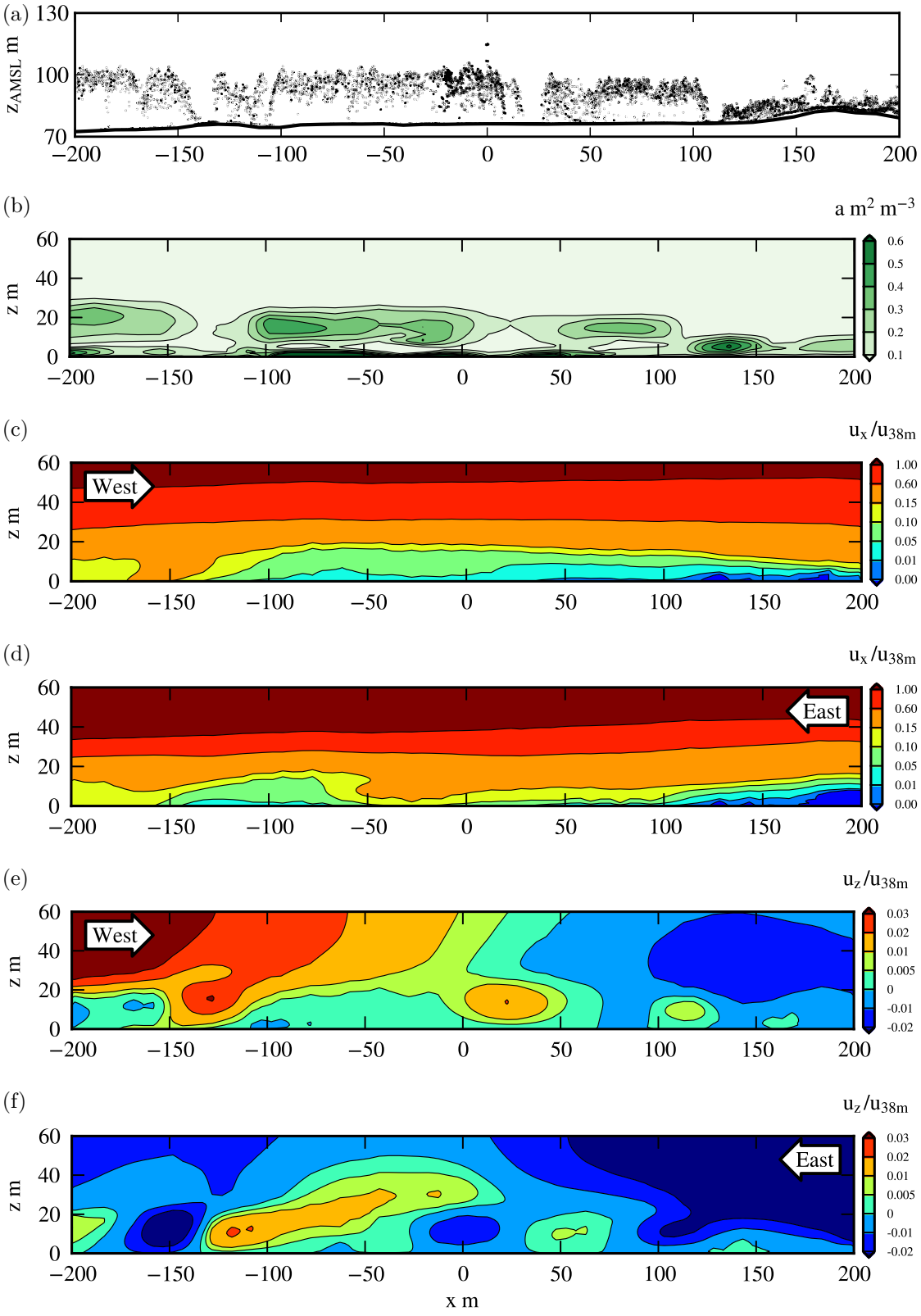

Figure 3.9: (a) West-east transect showing the point cloud distribution over a 10 m y-distance. Contours over a distance of 400 m of: (b) frontal area density, (c,d) west and east streamwise velocity component and, (e,f) west and east vertical velocity component. The velocity magnitude u_{38m} used for normalizing was taken at $z = 38$ m AGL at the mast location ($x = 0$).

gradient and the low pressure behind the forest edge at $x = 110$ m. For the eastern wind direction (Fig. 3.9f), the flow was mostly dominated by downward motions above $z = 50$ m from $-200 < x < 50$ m, an effect that was opposite in the western results (Fig. 3.9e). Inside the forest, the regions of updraughts and downdraughts were taking place at different locations for the eastern results compared to the western results (*e.g.* at $x = 0$ and $x = -100$ m). These differences suggests a strong wind directional dependence of the flow over and inside forests.

The profiles of u_x/u_{38m} (Fig. 3.10a) showed that the wind direction differences present in the measurements were captured in the CFD results. A better agreement was found for u/u_{38m} for the western wind direction ($R = 0.026$) compared to the eastern wind direction ($R = 0.046$). For the profiles of k/u^2_{38m} (Fig. 3.10b), the differences were small for the western wind direction ($R = 0.009$) but an over-prediction lying outside the measurement uncertainty range was obtained for the eastern wind direction ($R = 0.036$). Simulations performed with a flat terrain while preserving the forest information (not shown) indicated that the over-prediction was caused by the densely forested hill located upstream ($x = 400$ m, Fig. 3.8c).

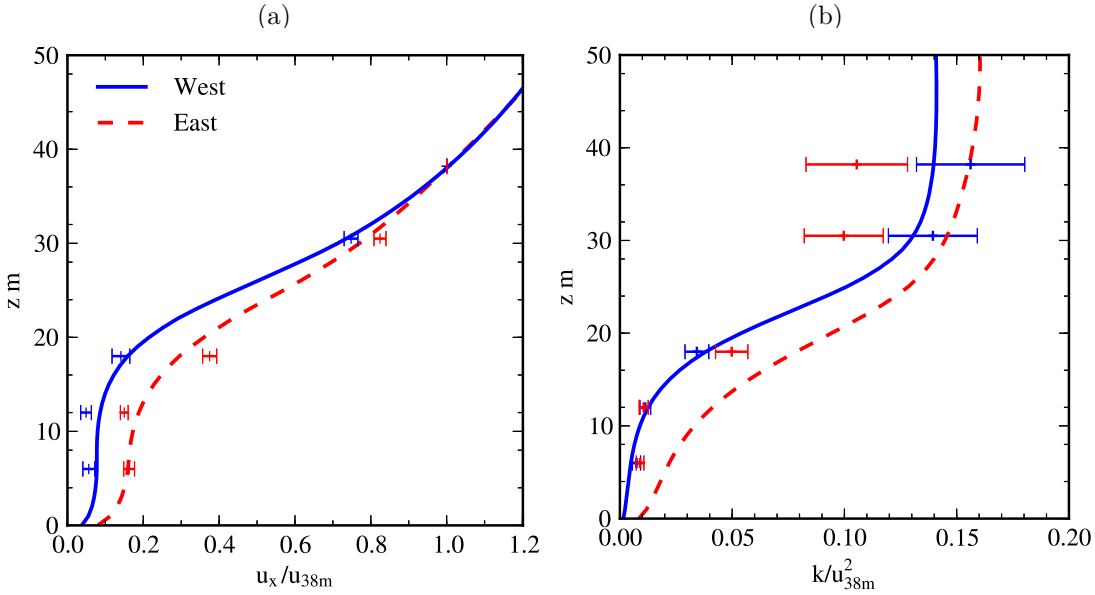

Figure 3.10: Comparison of simulation profiles: (a) streamwise velocity and, (b) turbulent kinetic energy with wind measurements from the western and eastern wind directions. The bars on the measurements indicate the extent of one standard deviation around the mean.

3.6 Discussion

The discussion is divided in three parts, each containing specific topics emerging from the study: the uncertainties from the presented methods for determining (1) the plant area index and (2) the tree height; and (3) recommendations and issues related to the wind simulations.

3.6.1 On the plant area index

The vertical profile of PAI_{eff}^{ALS} above $z = 11$ m was consistently lower compared to both the four and five rings profiles of PAI_{eff}^{PCA} (Fig. 3.7). In some cases, especially in the top part of the canopy, these PAI_{eff}^{PCA} readings were made very close to the stem or directly under a branch, leading to recordings that were likely higher than the average conditions at these heights. These problems were more easily avoided near the ground ($z = 2$ m) where the recordings are therefore expected to be more representative. Since there was an unphysical decrease in PAI_{eff}^{PCA} between $z = 11$ and 2 m (Fig. 3.7), we considered that the values of PAI_{eff}^{PCA} at the top part were in fact overestimated.

At the bottom part of the canopy, PAI_{eff}^{ALS} was reduced when the scanning resolution was lowered (Fig. 3.7). This local effect was due to higher amount of LiDAR reflections occurring in the top part of the canopy while fewer pulses penetrated the lower canopy. Although the observed differences were small, there could still be areas with very dense vegetation producing significantly poor estimates in the lower canopy. In wind simulations, most of the momentum is absorbed in the top part of the canopy (Wilson et al., 1982). For this reason, this effect was considered minor.

In this study, we assumed a spherical orientation of the canopy element surface angles — a specific approximation of the so-called G-function (Ross, 1981; Weiss et al., 2004). This function could be variable due to the variety of canopy element orientation, size and shape that can be observed for different types of forest. To test a different angle distribution on the vertical profile of PAI_{eff}^{ALS} (Fig. 3.7), the G-function was lowered from 0.5 to 0.4 in Eq. 3.5. At $z = 2$ m, where the results were more representative as argued above, a closer agreement with the PAI_{eff}^{PCA} results was found for 0.5. Richardson et al. (2009) also found that the G-function corresponded well to a spherical approximation for their analysis over a mixed-type forest, and mentioned that deviations from this theoretical distribution are not common. For these reasons, we considered the spherical approximation acceptable.

Compared with Solberg et al. (2009) and Richardson et al. (2009), low r^2 values were obtained in *Inventory A* (Fig. 3.5a, 3.5b in Section 3.5.1). Several factors

Table 3.1: $\overline{PAI}_{eff}^{PCA}$ in *Inventory A* for 14 measurement points taken on two different days (October 14 and 15) and for the day reported in the paper (October 12).

Date	$\overline{PAI}_{eff}^{PCA}$
October 14	2.83
October 15	3.12
Mean (October 14 + 15)	2.98
Paper (October 12)	3.01

may have influenced the scatter between PAI_{eff}^{PCA} and PAI_{eff}^{ALS}. Among them, the uncertainty related to the spatial resolution of the PCA could be mentioned (Fig. 3.5a). To assess this effect, the data were analyzed using either four of five rings. The r^2 values were similar using four rings ($r^2 = 0.178$) compared to five rings ($r^2 = 0.176$) indicating that the low correlation was not caused by the PCA resolution. Overall, the analysis was restricted to a small range of PAI values ($PAI_{eff} = 1-6$) and there was different influence from local forest heterogeneities for the two PCA and ALS methods. We believe that these factors were the most contributing to the low correlation.

Suboptimal light conditions may have caused a bias in $\overline{PAI}_{eff}^{PCA}$ (Leblanc and Chen, 2001). A sub-sample of fourteen of the grid points were measured on two supplementary days with predominantly clear and overcast conditions, respectively (Tab. 3.1). The differences in mean estimates of $\overline{PAI}_{eff}^{PCA}$ for these points between the two supplementary days and the day the complete measurements were recorded were below 6%. This result therefore provided a strong confidence in the PAI_{eff}^{PCA} values reported in the study.

Through the binning process, we ensured that the mean and standard deviation (variability) of the forest properties were well represented for the *Inventory A* area, where the scanning resolution was uniform and was ≈ 0.6 reflections m^{-2}. A smaller value for the binning radius was however used in our study compared to other studies ($r = 10$ m compared with *e.g.*, $r = 17.8$ and 15 m in Solberg et al. (2009) and Richardson et al. (2009), respectively). In our method, the binning represent a well-defined area but the PCA includes information from the local forest over an unknown area. Averaged over *Inventory A*, the $\overline{PAI}_{eff}^{ALS}$ results were almost independent of the binning radius (Fig. 3.4a). Moreover, varying the binning radius from $r = 10$ to 15 m produced a small effect on the vertical profile of PAI_{eff}^{ALS} (Fig. 3.7). Since we were aiming at obtaining a grid variability similar

to the PCA (Fig. 3.4b) while keeping the bin radius small, this increased our confidence in applying a value of $r = 10$ m in our analysis.

3.6.2 On the tree height

A mean tree height underestimation was systematic over the four 200×200 m^2 areas (Fig. 3.6a and 3.6b). For low scanning resolutions, the top part of the canopy was missing in the point cloud which explained the high sensitivity for the tree height (Fig. 3.6b). Depending on the CFD application, a h_{max} underestimation could potentially affect the wind results. Here, we validated the RANS model with near- and within-canopy wind measurements, which demanded a precise description of the forest properties. By coincidence, the ALS scans in the immediate vicinity of the wind mast were of considerably higher resolution (> 2 reflections m^{-2}) than the rest of the investigated area (Fig. 3.6a). Given that the mean underestimation of $\overline{h}_{max}$ for *Inventory A* and *Inventory B* was $\simeq 2$ m and that $\overline{h}_{max}$ showed a uniform increase of $\simeq 1$ m when the scanning density was increased from 0.6 to 2.4 reflections m^{-2} (Fig. 3.6b), we estimated that the error on h_{max} was < 1 m, which corresponded to $\leq 5\%$ of the local tree height. In addition to being within the uncertainty of the CFD grid vertical resolution (≈ 1 m at 30 m), we considered this underestimation negligible.

3.6.3 On the wind simulations

CFD applications require input over large areas which may include sub-areas of different scanning resolutions (Fig. 3.6a). For the Skogaryd forest, increasing the scanning resolution had a small effect on the mean values of $\overline{PAI}^{ALS}_{eff}$ (Fig. 3.6b). The vertical profile of PAI^{ALS}_{eff} was also unaffected by the scanning resolution down to a certain level at the bottom of the canopy (Fig. 3.7). Nevertheless, we suggest using scans with a resolution exceeding 0.6 reflections m^{-2} to avoid potential inaccuracies. At this resolution, an error of ≈ 5 % can be expected for the tree height and $\approx 2\%$ for the PAI.

The ALS technique gives a temporal snapshot of the forest properties. For wind-energy projects, the surface conditions evolve during the operating lifetime of wind farms (20-30 years). The average forest height growth over such a time period is significant (Lieffers et al., 1996). This can substantially affect the wind field during the life-span wind farm projects. In this case, other techniques allowing the temporal variations of the growth to be monitored, such as synthetic aperture radar for example (Peduzzi et al., 2012), could be used to apply corrections to the ALS data (Clewley et al., 2012). On shorter time periods, the extinction coefficient of light γ (Eq. 3.5) could change throughout the year (Bréda, 2003). This is due

to a particularly different light absorption behavior, for example, during the leaf on–leaf off periods in the summer and winter seasons. For coniferous forests, as was the case here, this effect could be ignored.

In the wind results, we showed that the LiDAR method produced a highly variable wind field above and within the canopy (Fig. 3.8e, 3.8f and 3.8d). Local phenomena such as flow separation were observed in hilly regions of dense forest (Fig. 3.8e and 3.8d). The u_z component was more strongly correlated than u_x with the canopy structure (Fig. 3.8f). By comparing results of two different wind directions (Fig. 3.9), a strong wind directional dependence was found. In Fig. 3.10a, the differences shown in profiles of mean velocity measurements between two opposite wind directions were correctly captured in the simulations. However, the TKE profile from the eastern wind direction showed a notable over-prediction (Fig. 3.10b). About 400 m upwind of the mast, a small hill (Fig. 3.8c) covered with dense forest (Fig. 3.8a, 3.8b) was identified as the source of the over-prediction (not shown). The $k-\epsilon$ model is well-known to suffer from various drawbacks when applied to free shear flows and under conditions of adverse pressure gradient (Wilcox, 2006), which was the case over the forested hill. The results indicate that the CFD model may need further development for accurate predictions in complex forested terrain. For such development, the proposed method provides an easily applicable flow modeling test bed with low uncertainty inputs, where the performance of different CFD models can be assessed at sites with high-quality wind measurements.

3.7 Conclusion

A LiDAR-based method was developed to retrieve the canopy structure for CFD applications and was able to recover forest properties with a good agreement with ground-based measurements. Detailed wind profile measurements provided a strong validation case for the CFD simulations. The CFD simulations showed a high variability in close correlation with the canopy structure. The LiDAR method can reduce the gap between predictions in numerical wind models and the true flow processes observed in nature.

Acknowledgments

The authors acknowledge the financial support of the Center for Computational Wind Turbine Aerodynamics and Atmospheric Turbulence sponsored by the Danish Council for Strategic Research, grant number 09-067216, Vattenfall and Vindforsk III, a research program sponsored by the Swedish Energy Agency. The authors also thank Margareta Hellström from Lund University and Mats Räntfors

from Gothenburg University for their valuable contribution with the inventory of the Skogaryd forest; the financial support of Formas, for the help provided by Elin Julén within the project Landscape Scale Investigation of Greenhouse Gas Exchange (LAGGE); and the Test and measurements section at DTU Wind Energy for their technical support. We also thank the three anonymous reviewers for their insightful comments. The code developed in this work to generate the forest CFD input is freely available upon request.

4

SITE INVESTIGATION

Abstract

We investigated the effect of the canopy description in a Reynolds-averaged Navier-Stokes (RANS) method based on key flow results from a complex forested site. The canopy structure in RANS is represented trough the frontal area of canopy elements per unit volume, a variable required as input in canopy models. Previously difficult to estimate, this variable can now be easily recovered using aerial LiDAR scans. In this study, three approaches were tested which were all based on a novel method to extract the forest properties from the scans. A first approach used the fully spatial varying frontal area density. In a second approach, the vertical frontal area density variations were ignored, but the horizontally varying forest heights were kept represented. The third approach ignored any variations: the frontal area density was defined as a constant up to a fixed tree height over the whole domain. The results showed significant differences among the cases. The large-scale horizontal heterogeneities produced the largest effect on the variability of wind fields. Close to the surface, specifying more details about the canopy resulted in an increase of $x-y$ area-averaged fields of velocity and turbulent kinetic energy.

4.1 Introduction

The mean wind speed, turbulence and scalar fluxes are modified by the heterogeneities present in forests (Bohrer et al., 2009; Dellwik et al., 2014). The more clearings, forest edges and density variations a canopy contains, the more likely the flow within and above the canopy will be subject to gradients and develop differently. The local wind field could thus be significantly modified by these heterogeneities. Predicting the wind field using numerical simulations in those circumstances becomes a technically difficult task and can have consequences for different applications and several areas of research. For example, the installation

This chapter has been published as: Boudreault, L.-E., Bechmann, A., Sørensen, N., Sogachev, A., and Dellwik, E. (2014a). Canopy structure effects on the wind at a complex forested site. In *Journal of Physics: Conference Series*, volume 524 012112. IOP Publishing.

of wind turbines in and close to forests is becoming a more common practice within the wind energy industry due to a decrease in high quality sites availability. In the RANS simulations by Lopes Da Costa et al. (2006), it is reported that the wind field is sensitive to the canopy density and that the latter contributes in great part to the simulation uncertainty. It is also mentioned that the simulation results are strongly dependent on the wind direction. In Dupont and Brunet (2006), the high turbulence intensity zones over a fragmented forest landscape were pointed out as the cause of wind damage occurrences on trees. Physically, the creation of near-surface wind gusts generated by the local heterogeneities was mentioned as the source of these damaging occurrences. In fire propagation modeling, a study (Pimont et al., 2011) pointed out that the density of the forest cover was related to the fire intensity and that the wind spatial variability increased for larger clumps of heterogeneities (see also, Panferov and Sogachev, 2008). The canopy structure description in this context is thus becoming an important issue.

An approach often employed to model the effect of the canopy in numerical modeling is the distributed drag formulation, using a momentum sink S_d as:

$$S_d = -C_d a |u| u_i, \tag{4.1}$$

where C_d is the drag coefficient, u_i the mean wind velocity components in the i direction ($x_i \equiv \{x_1, x_2, x_3\} \equiv \{x, y, z\}$) and $|u|$ denotes the velocity magnitude. The specification of the canopy structure is performed using the variable a — the frontal area density. This variable is defined as the area of leafs, branches and stems opposing the wind flow per unit volume (in m^2 m^3). Another important variable of consideration is the tree height h_{max}, which indicates the level below which the drag terms should be applied. However, wind modelers are often constrained by limited input information. Simplifications in the specification of a and h_{max} are therefore often necessary. To verify if such simplifications would be justified, we investigated the differences produced in the wind field by canopy descriptions of varying complexity. A series of tests were performed using a CFD model, in which the canopy description was successively degraded. A sensitivity analysis of the wind direction using a fully detailed canopy was also performed.

4.2 Methodology

4.2.1 Test site description

The Skogaryd site is a forested site dominated by Norway spruce located $\simeq 50$ km from the west coast of Sweden. A 38-m-tall mast located at 58°21′50.5”N, 12°8′59.4”E, was the basis for the experiment and was equipped with six sonic anemometers (Metek USA-1 Basic), which were mounted at 1.2, 6.5, 12.5, 18.5,

31.0 and 38.4 m above the local ground level. During the experiment, aerial LiDAR scans of the forest surrounding the tower were performed. A complete description of the experimental method can be found in Boudreault et al. (2014b). The terrain was fairly flat in the domain as the difference between the highest and the lowest elevation point was 35 m.

4.2.2 CFD model

The CFD model was based on the RANS equations using the standard $k-\epsilon$ model (Jones and Launder, 1972). For wind power production, the high wind speed situations are the most relevant. They generally coincide with neutral stratification which motivated the focus on the neutral case only. For the near-surface flow in these situations, the influence from the Coriolis force is small, except deep inside the canopy, and it was therefore neglected. The terrain elevation was assumed flat in the simulations. The source term in Eq. 4.1 and an additional source term in the transport equation of dissipation ϵ were added in the model to account for the effect of the canopy (Sogachev and Panferov, 2006; Sogachev, 2009). The turbulence model constants were set to $C_\mu = 0.06$, $\kappa = 0.4$, $\sigma_k = 1.0$, $\sigma_\epsilon = 2.1$, $C_{\epsilon 1} = 1.52$ and $C_{\epsilon 2} = 1.83$. A polar grid of 30 km diameter surrounding an inner 4×4 km^2 Cartesian grid was used. The computational grid had an $x-y$ resolution of 10 m in the inner region. A hyperbolic mesh generator (Sørensen, 1998) was used to make a three-dimensional volume grid. The domain height was set to 4 km with a vertical near-ground resolution of 0.03 m, from where it was expanded to a resolution of about 1 m at a 30 m height above the ground. Simulation tests indicated that the numerical solution was grid-independent. Inside the inner domain, where the forest information was available, a roughness height of $z_0 =$ 0.03 m was prescribed at the ground boundary below the canopy. Outside this domain, tests showed that a roughness of $z_0 = 0.03$ m was appropriate to reproduce the farfield conditions. The set of equations were solved using the EllipSys3D flow solver (Michelsen, 1992, 1994; Sørensen, 1995). The Leonard's third-order accurate QUICK scheme (Leonard, 1979) was used on the advective operators and the standard second-order central difference scheme for all remaining terms was used. As boundary conditions, values of u, k and ϵ in accordance with log-law relationships were prescribed at the inlet and at the top of the domain. Standard Neumann conditions (zero normal gradients) were used at the outlet. The inlet boundary condition extended over a 270° portion on the exterior boundary of the polar domain and the outlet boundary condition extended over a 90° portion. Standard log-law wall functions were applied at the ground boundary, as described in Sørensen (1995). The wind direction simulated for the main results is 270° (westerly wind).

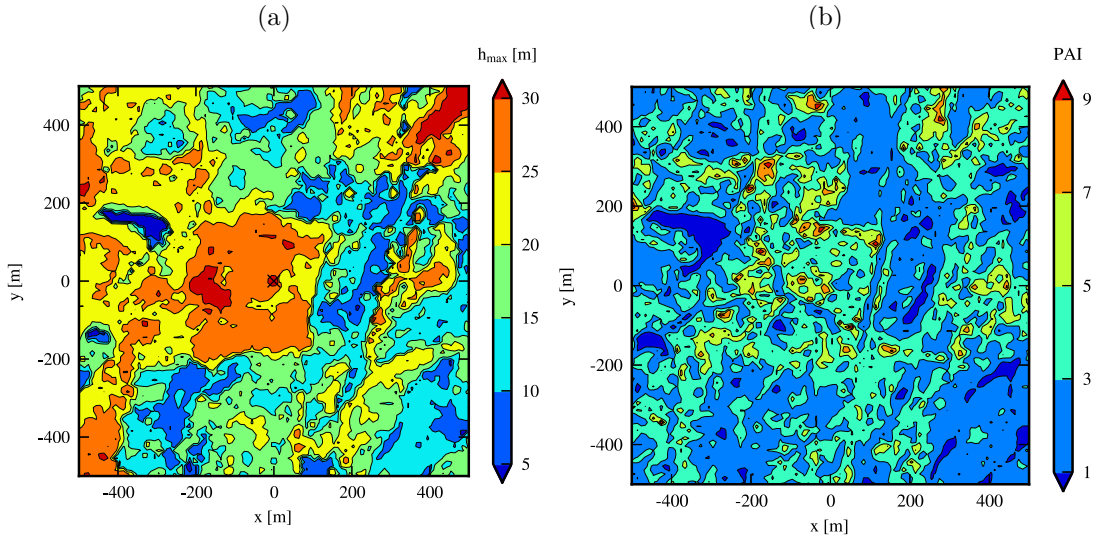

Figure 4.1: (a) Tree height and (b) plant area index, as obtained from the method described in *Case 1*.

4.2.3 Case study

In the following tests, three different cases including different levels of canopy structure complexity were used. In the first case, denoted *Case 1*, varying profiles of a in x, y and z as well as varying forest heights were used. This setup was the reference case from which the wind results obtained from the other two less detailed cases were compared. In *Case 2*, the frontal area density was kept constant with height but the forest height was spatially variable. In *Case 3*, a constant forest height and a constant frontal area density a was imposed throughout the domain. For all cases, the canopy information was prescribed inside and near the inner area of the CFD grid over 5×5 km^2. More specifically, the a and h_{max} distribution for each cases were defined as follows:

Case 1

A complete description of the method used for this case can be found in Boudreault et al. (2014b). In this method, the distribution of a was calculated based on aerial LiDAR scans. Compared to other remote sensing methods, LiDAR scans generally provide the most detailed description as it can reveal the 3D structure of the canopy. The resulting output is a grid of ijk index containing discrete values of a. In this method, the forest grid generated had a bin radius of $r = 10$ m, a grid spacing of $\Delta x = \Delta y = 10$ m and layers of $\Delta z = 1.0$ m thickness. The forest properties obtained can be visualized in Fig. 4.1 and Fig. 4.2 where the plant area index (PAI) was

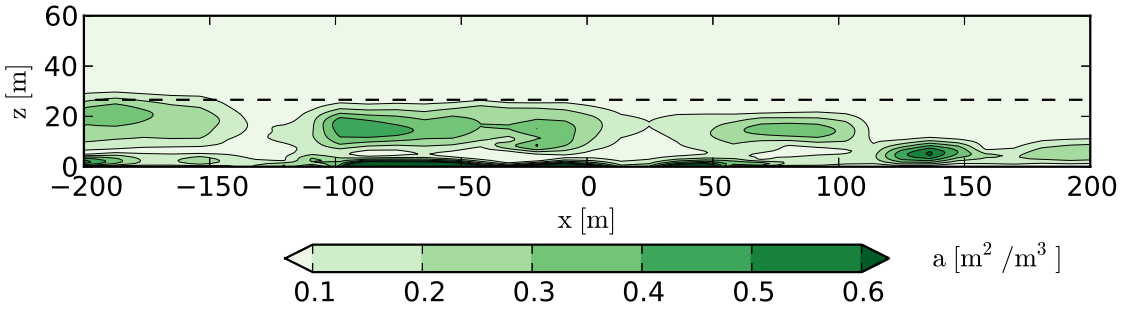

Figure 4.2: Frontal area density contours as retrieved from aerial LiDAR scans for a transect at $y = 0$ m passing trough the mast location ($x = 0$ m). The dash line indicate the constant forest height fixed in *Case 3* ($h_{max} = 26.6$ m).

obtained by summing the a^{ij} values over the k index:

$$PAI^{ij} = \sum_{k=1}^{n_h} a_k^{ij} \Delta z \,, \quad \text{where} \quad n_h = ||h^{ij}/\Delta z||. \tag{4.2}$$

Case 2

The distribution of constant a values was calculated based on the local plant area index and h_{max} was obtained from the method in *Case 1*. To do this, the PAI at the ij positions was kept the same as calculated in *Case 1*. The frontal area density at the ijk positions was then fixed to constant values of $a^{ijk} = PAI^{ij}/h^{ij}$.

Case 3

To determine a fixed a and h_{max} value for *Case 3*, we considered an averaging area of 200×200 m^2 centered around the mast location $(x, y) = (0, 0)$. This area was chosen as it was fairly homogeneous (Fig. 4.1), i.e. the trees were of the same species and similar heights. The values obtained were $\overline{PAI} = 4.5$ and $\overline{h}_{max} = 26.6$ m. The frontal area density was therefore fixed to $a = \overline{PAI}/\overline{h} = 0.169$ m^{2}m^{-3} over a fixed canopy height of $\overline{h} = 26.6$ m (showed as a dashed line in Fig. 4.2).

4.3 Results

The simulations for the three cases described in Section 4.2.3 were compared. The velocity magnitude u and the turbulent kinetic energy tke were used as comparison variables. The profiles obtained from the numerical results in the three cases were first validated with the mast measurements. The focus was put on results of a

1×1 km^2 area centered on the tower location below a height of 50 m above the ground level. This choice was motivated by the fact that an internal boundary layer will grow at the edges of the 5×5 km^2 area where the forest was prescribed. It was evaluated to be about 50 m thick over this area (Dellwik and Jensen, 2000). Area-averaged profiles over 1×1 km^2 areas at different heights were then compared between the cases. In these results, the root mean square error (R) estimator was used and was defined as:

$$R_{\phi_{12}} = \sqrt{\frac{\sum_{i=1}^{n}\sum_{j=1}^{m}(\phi_{1,ij} - \phi_{2,ij})^2}{n \times m}}, \tag{4.3}$$

as well as the percentage difference (%Diff) estimator,

$$\%\text{Diff}_{\phi_{12}} = \left| \frac{\phi_{2,ij} - \phi_{1,ij}}{\phi_{1,ij}} \right| \times 100, \tag{4.4}$$

where ϕ_1 and ϕ_2 were field variables under consideration in two different cases (*e.g. Case 1* and *Case 2*).

4.3.1 Wind direction sensitivity

The high variability of the canopy structure induces different wind fields with different wind directions, as reported in Lopes Da Costa et al. (2006). Therefore, an important aspect to verify first is how sensitive this effect could be. A wind direction analysis around the reference wind direction (270°) was thus performed for angles of ±1°, ±5°, ±10° and ±15°. This test used the full canopy structure description as obtained by the LiDAR measurements (*Case 1*). In Table 4.1, the R for the wind directions ±1° was small for both u/u_{50m} and tke/u_{50m}^2 (≈ 0.0075 and 9.5×10^{-5}, respectively). For wider angles, the $R_{u/u_{50m}}$ remained similar when the wind direction was changed (ranging between 1.8×10^{-2}–2.9×10^{-2}) but the R_{tke/u_{50m}^2} showed a higher sensitivity and variability (ranging between 3.26×10^{-4}–8.15×10^{-4}). The error due the wind direction is thus expected to remain similar for the velocity field within wind sectors of 10–30°; but larger errors and variability are expected in the tke field. Below a 2° wide sector, the differences in the flow field were negligible. As the wind direction variability in the present simulations can only be reproduced with spatially varying a and h_{max}, a minimal variability in the wind direction can only be obtained by including a description of the larger clumps of heterogeneities, as they produce the largest effect on the wind field (Pimont et al., 2011).

Table 4.1: Root mean square error (R) over a 1×1 km^2 area between the reference wind direction (270°) and perturbation values for the *Case 1* setup at 50 m AGL

Wind direction	$R_{u/u_{50m}}$	$R_{tke/u^2_{50m}}$
$270° - 1°$	0.0069	9.91×10^{-5}
$270° + 1°$	0.0078	9.06×10^{-5}
$270° - 5°$	0.0230	3.26×10^{-4}
$270° + 5°$	0.0260	4.61×10^{-4}
$270° - 10°$	0.0292	7.39×10^{-4}
$270° + 10°$	0.0188	4.18×10^{-4}
$270° - 15°$	0.0299	8.15×10^{-4}
$270° + 15°$	0.0187	4.98×10^{-4}

4.3.2 Profiles validation

Profiles from the simulation results and the mast measurements were compared (Fig. 4.3a and 4.3b). $R_{u/u_{38m}}$ was the lowest for *Case 1* (*Case 1*: 0.0358; *Case 2*: 0.0366; *Case 3*: 0.0385). The profiles in *Case 1* and *Case 2* compared better to measurements than *Case 3* inside the forest and the profile in *Case 3* was in closer agreement above the canopy (Fig. 4.3a). A secondary maximum close to the surface was observed in *Case 1* (Fig. 4.3a), a characteristic that was absent in the other two cases. This characteristic was attributed to specifying a varying distribution of a in the vertical direction above the surface. For the tke/u^2_{38m} (Fig. 4.3b), the lowest $R_{tke/u^2_{38m}}$ was obtained for *Case 2* (*Case 1*: 0.0926; *Case 2*: 0.0920; *Case 3*: 0.0923). The profiles in *Case 1* and *Case 2* were generally closer to the error range of the measurements than in *Case 3* (Fig. 4.3b). An overprediction of tke/u^2_{38m} was apparent inside the canopy in *Case 3* (Fig. 4.3b).

4.3.3 Fields comparison

In the following results, the upstream farfield velocity at 50 m above the ground level was used to normalize the fields. Visual inspection of the fields of u/u_{50m} for *Case 1* and *Case 2* showed similarities (Fig. 4.4a, 4.4b), as the contour patterns generally coincided, but with different mean values. The mean velocity was higher in *Case 1* ($u/u_{50m} = 0.64$) compared to *Case 2* ($u/u_{50m} = 0.62$) and *Case 3* ($u/u_{50m} = 0.57$). For the tke/u^2_{50m} fields (Fig. 4.4c, 4.4d), the average value was comparable for all cases ($tke/u^2_{50m} \approx 0.032$). The tke/u^2_{50m} was different between *Case 1* and *Case 2* above the central high and dense forest patch ($-200 > x > 200$ m and $-200 > y > 200$ m, Fig. 4.1a, 4.1b) as the contours levels differed in location and shape.

The *Case 1*-*Case 2* and *Case 1*-*Case 3* percentage difference fields (computed

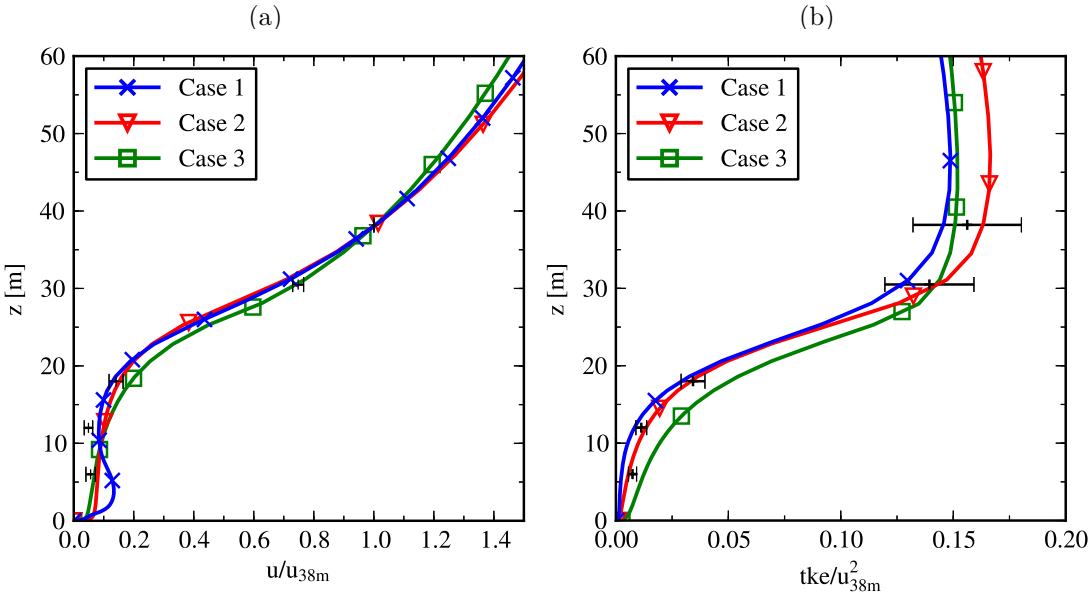

Figure 4.3: Profiles of (a) u/u_{38m} and (b) tke/u^2_{38m} for all 3 cases compared with mast measurements. The normalization velocity u_{38m} was taken at the 38 m level at the mast location. The error bars on the measurements shows the extent of one standard deviation around the mean value.

from Eq. 4.4) were compared (Fig. 4.5). For *Case 2* (Fig. 4.5a), the % difference in velocity with *Case 1* was globally below 6%. The largest differences were observed along the lines at $y = -200$ and $y = 200$ m, physically located along the north and south forest edges of the central tall trees and dense forest patch (Fig. 4.1a, 4.1b). For *Case 3* (Fig. 4.5b), the difference was generally larger than in *Case 2*. The error was the smallest in the central patch around the mast and in areas where the forest was homogeneous and had similar mean values of forest properties imposed (such areas could be seen along $x = -200$ m and at $(x, y) = (-200, 250)$ m in Fig. 4.1a, 4.1b). The largest percentage difference in tke/u^2_{50m} for *Case 2* (Fig. 4.5c) was inside the central forest patch, in the wake of the patch, as well as in the clearings along $y = -450$ m and at $(x, y) = (-400, 200)$ m. For *Case 3* (Fig. 4.5d), the largest differences were observed in the clearings.

4.3.4 Area-averaged profiles

In this section, $x - y$ area-averaged results, denoted by angled brackets $\langle \cdot \rangle_{xy}$, are presented at different heights. The area-averaged profiles (Fig. 4.6) clearly indicated higher $\langle u \rangle_{xy}/u_{50m}$ and $\langle tke \rangle_{xy}/u^2_{50m}$ in the following order: *Case* 1 > *Case* 2 > *Case* 3. The velocity profiles differed and reached a percentage differ-

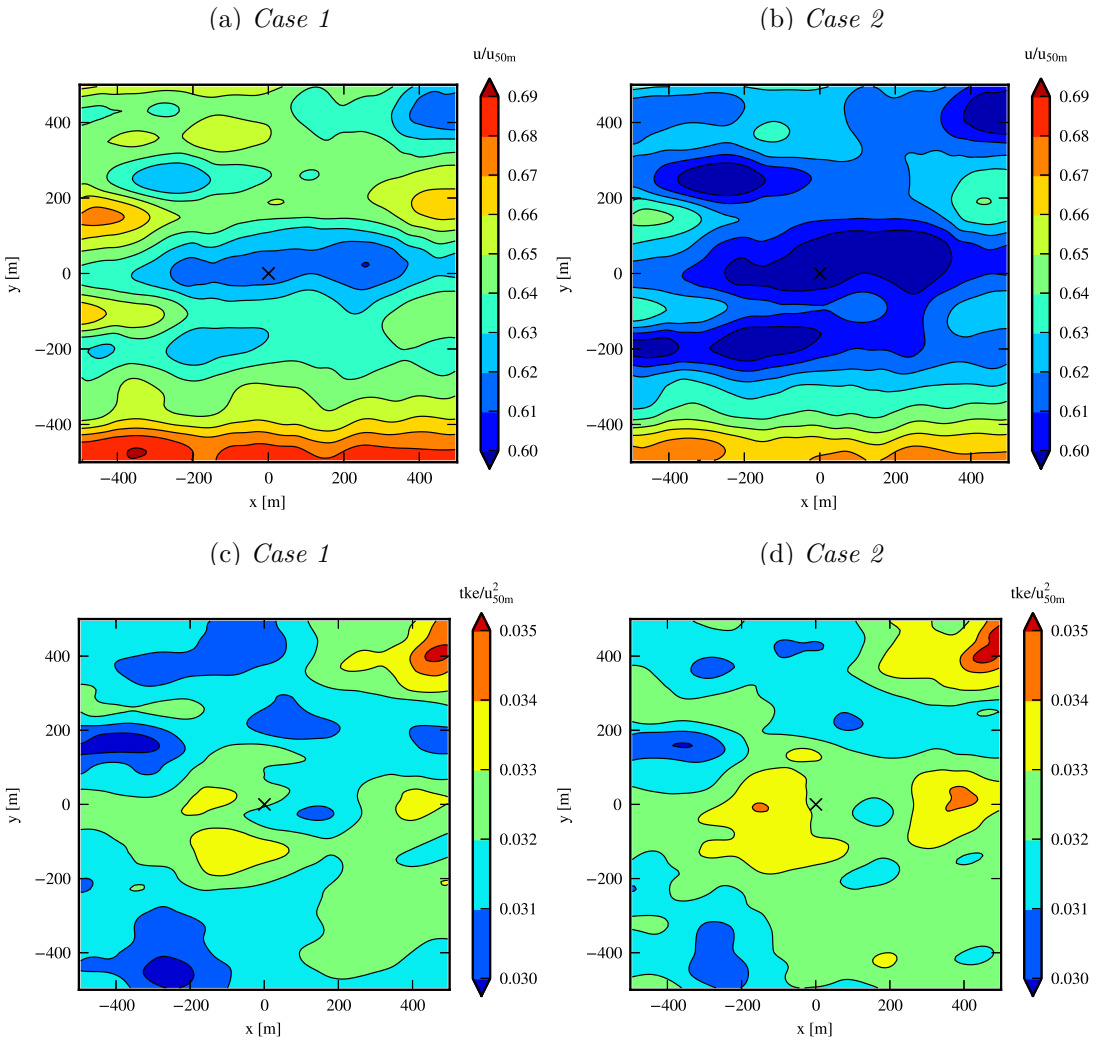

Figure 4.4: Contours of u/u_{50m} and tke/u_{50m}^2 at a height of 50 m above the ground level for *Case 1* and *Case 2*. The upstream farfield velocity u_{50m} at 50 m was used to normalize the fields. The flow direction goes from left to right.

ence of 8.9% between *Case 1*-*Case 3* and 3.5% between *Case 1*-*Case 2* at a height of 50 m. The *tke* profiles almost coincided above 40 m AGL (both *Case 2* and *Case 3* were below 1.5% of *Case 1* at 50 m AGL). The highest variability (standard deviation) in *Case 1* and *Case 2* were close to the canopy top, *i.e.* around 20 m for the velocity and 15 m for the *tke* profile (no variability was present in *Case 3* as the forest was horizontally homogeneous).

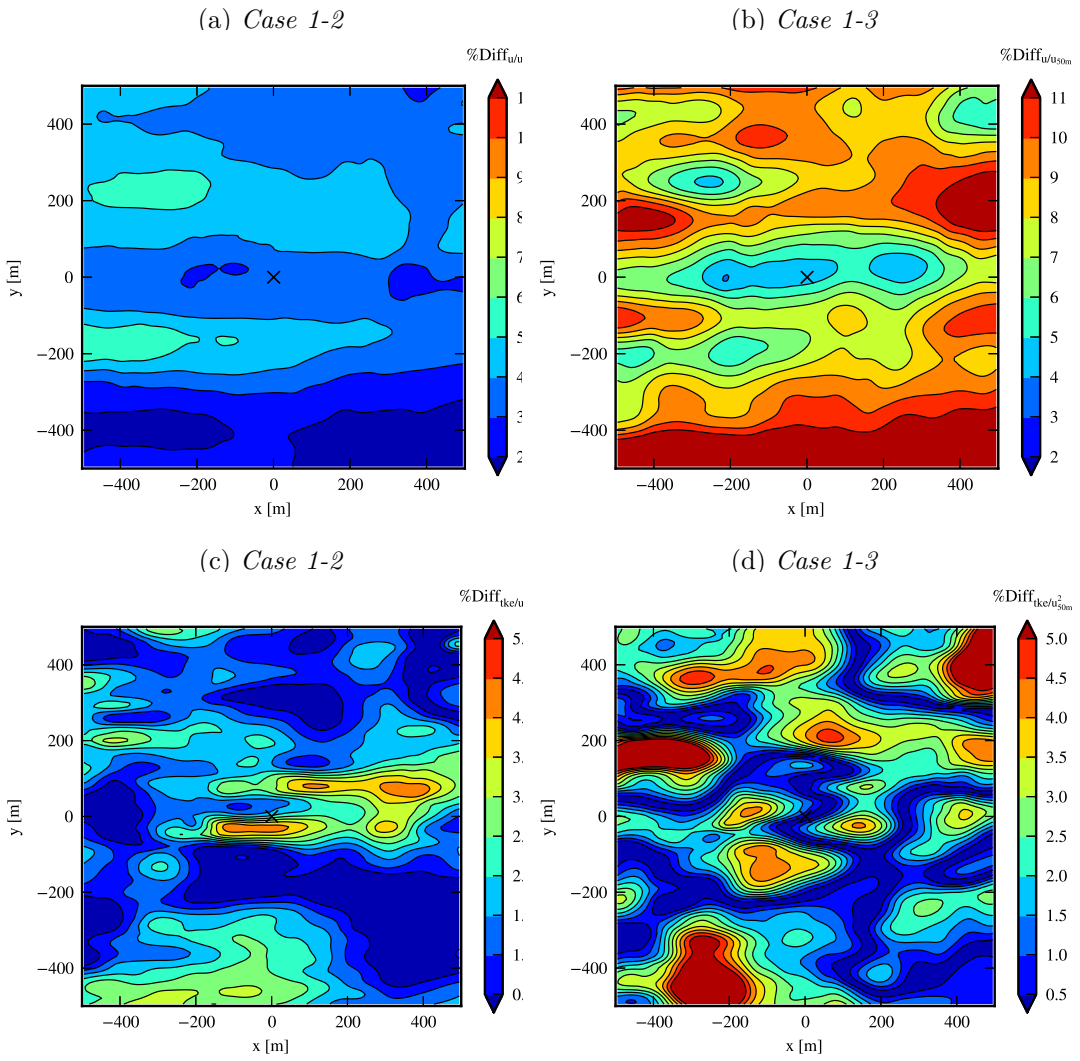

Figure 4.5: Percentage difference in u/u_{50m} and tke/u^2_{50m} between *Case 1* and *Case 2* and *Case 1* and *Case 3* at 50 m above the ground level. The upstream farfield velocity u_{50m} at 50 m was used to normalize the fields. The flow direction goes from left to right.

4.4 Discussion

Several points of discussion could be raised from the results. First, the profiles in Fig. 4.3 showed that a secondary maximum was produced in *Case 1* while it was absent in the other two cases. This shows that the predicted flow processes within the canopy are different for a method allowing density variations in the vertical direction compared to a method where the profiles are constant. This will affect

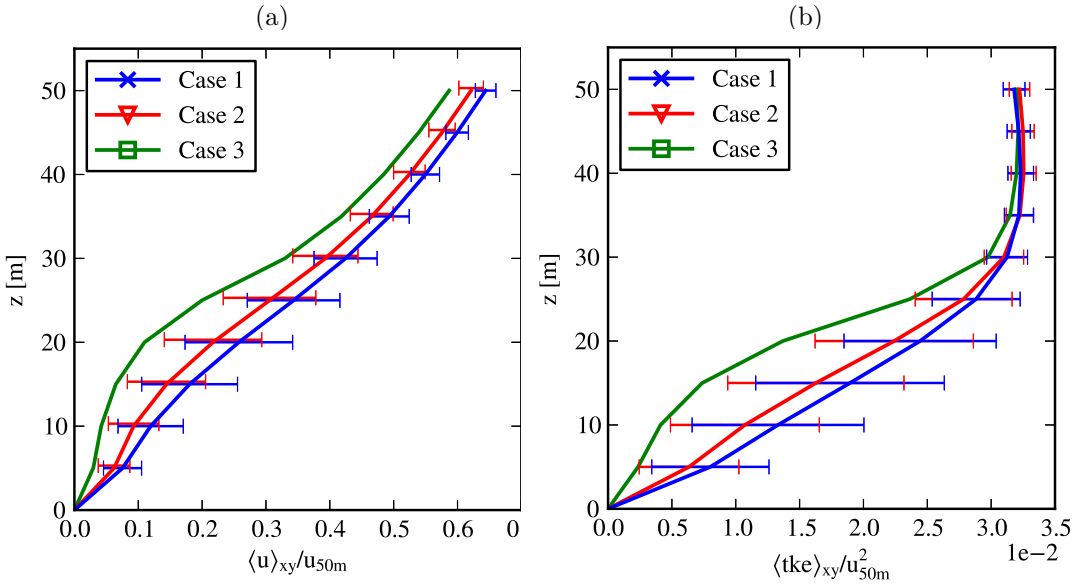

Figure 4.6: Spatially averaged profiles of (a) $\langle u \rangle_{xy}/u_{50m}$ and (b) $\langle tke \rangle_{xy}/u_{50m}^2$ at different heights over the 1×1 km^2 area for all three cases. The upstream farfield velocity u_{50m} at 50 m was used to normalize the profiles. The error bars on the profiles shows the extent of 1 spatial standard deviation around the mean value over the area.

the predictions in situations where the terrain is complex, *e.g.* close to forest edges (Dellwik et al., 2014) and potentially in steep orography. For the flow above the forest, the velocity profiles were similar but the *tke* profiles showed larger differences. Generally, the profiles agreed well with the measurements since they were close or within the range of one standard deviation of the measurements. However, for the upstream area along $y = 0$ m in the direction in-line with the mast (Fig. 4.1), the forest was fairly homogeneous which may explain the good comparison, and why only small differences were observed between the profiles. When a forest patch of a few hundreds of meters was obstructing the wind flow, *e.g.* in the central area and over clearings, differences between the methods started to appear (Fig. 4.5). In Fig. 4.4, the small variations in canopy density produced small visible differences in the velocity field between *Case 1* and *Case 2*. More significant differences were observed in the turbulence field, even when the forest was homogeneous, as was the case over the central forest patch. The velocity field was thus sensitive to changes in larger agglomerations of heterogeneities (*e.g.* along the forest edges of the central forest patch) while the *tke* field showed sensitivity to both the larger and the smaller heterogeneities (Fig. 4.5). To summarize, the accuracy in the *tke* prediction will be compromised if the smaller scale canopy structures are poorly

described. This aspect is however less significant for the velocity field, for which the larger heterogeneities are more important to parameterize.

The area-averaged profiles (Fig. 4.6) showed that the wind velocity and *tke* increased with an increasing amount of canopy details over the whole investigated height range. The presented results were however based on a simplified case over flat terrain in a 1×1 km^2 area. The effect of the canopy on the wind over a real terrain and a large domain should also be investigated. In complex orography, the flow may interact more strongly with the canopy and alter the wind field accordingly.

4.5 Conclusion

In this study, RANS simulations involving different levels of canopy structure complexity were performed. Non-negligible differences were found such that:

- the 50 m wind velocity over the 1×1 km^2 showed less sensitivity in wind direction change than the *tke* results;
- the velocity was more sensitive to the larger-scale heterogeneities while the *tke* was more sensitive to the smaller-scale heterogeneities;
- the most detailed methods of canopy structure description produced the highest velocities and *tke* results;
- using methods of the same PAI but prescribing a profile of constant vertical density failed to capture the secondary maximum close to the surface.

The results presented here showed that including an increasing amount of smaller heterogeneity variations in the canopy description is important when the site is complex.

Acknowledgements

The authors acknowledge the financial support of the Center for Computational Wind Turbine Aerodynamics and Atmospheric Turbulence sponsored by the Danish Council for Strategic Research, grant number 09-067216, Vattenfall and Vindforsk III, a research program sponsored by the Swedish Energy Agency.

5

EDGE FLOW

Abstract

Most of our knowledge on forest edge flows comes from numerical and wind-tunnel experiments where canopies were horizontally homogeneous. To quantify the impact of tree-scale heterogeneities (> 1 m) on edge flow dynamics, the flow in an inhomogeneous forest edge of the Falster island in Denmark is investigated using large-eddy simulation. The three-dimensional forest structure is prescribed in the model using high resolution helicopter-based LiDAR scans. The large-eddy simulation model is evaluated against field measurements, where the characteristics of the turbulent airflow upwind and downwind of the forest leading edge are compared. Several differences are identified in the mean two-dimensional edge flow compared to an equivalent homogeneous forest. The most important one is related to a further flow penetration found inside the canopy. Key properties to describe the edge include the density and vertical foliage distribution, both controlling the flow tilt angle and flow penetration within the canopy. Other differences are related to a slower adjustment of the correlation coefficient and the absence of a defined enhanced gust zone at canopy top. Forest heterogeneities induce significant spatial standard deviations of flow statistics, increasing with high-order moments. The spatial standard deviation of velocity can reach 30% of the mean at half-canopy height for a forest with plant area index and tree height spatial standard deviations of about 60% and 20%, respectively. Spatial-averaging over calculated flow statistics from the simulation using the heterogeneous canopy description yielded non-negligible dispersive fluxes at and near the edge. The spatial variability is found important in edge flow.

5.1 Introduction

The fragmented nature of forested landscapes leads to complex three-dimensional wind dynamics, and thus complex momentum, energy and mass exchanges between vegetated canopies and the atmosphere. An improved understanding of

Manuscript in preparation for *Boundary-Layer Meteorology*.

these exchanges is relevant for the fields of wind energy, in terms of wind resource assessment, or for pollen and pollutant dispersion.

Forest edge is one of the common heterogeneities encountered in forest landscapes. The wind dynamics over forest edge has been investigated in a number of studies using field, wind-tunnel or numerical experiments (*e.g.* Irvine et al., 1997; Morse et al., 2002; Yang et al., 2006; Dupont and Brunet, 2008b, 2009; Dupont et al., 2011; Dellwik et al., 2014). Dupont and Brunet (2008b) and Dupont et al. (2011) showed that edge flow depends on the vertical structure of the forest and on its density. For forests with a uniform vertical foliage distribution, the edge flow is characterized by the development of a growing internal boundary layer from the edge, the decrease of the streamwise wind velocity and turbulence within the canopy, an enhanced gust zone at the canopy top where sudden strong events (gusts) have a high probability of occurrence (see Raupach et al., 1987), and further downstream, the development of a turbulent region above the canopy as a growing layer within the internal boundary layer (Fig. 5.1a). For such forest, the flow adjusts with the canopy at about 8-10 canopy heights. For canopies with a foliated layer concentrated in the upper canopy, the above picture changes (Fig. 5.1b). The turbulent region developing above the canopy starts closer to the edge, no well-defined enhanced gust zone is observed, and a wind jet is present in the sparse sub-canopy layer over a long distance from the edge, inducing a layer with positive turbulent momentum flux around the base of the foliated layer. For such forest, the length of the adjustment region can extend to more than 20 canopy heights depending on the vertical extension of the trunk space. With denser canopy the flow is more distorted at the edge, adjusts faster, and higher gustiness is observed in the enhanced gust zone. These edge flow characteristics were mostly obtained from wind-tunnel and numerical experiments where canopies were horizontally uniform. In nature, forests are often not uniform in density and in height as a consequences of light competition between tree species and natural damage (windstorm, fire, pests, diseases, etc.). As a consequence, an open question remains whether tree-scale horizontal heterogeneities, as the forest vertical structure, modify significantly the above canopy edge flow picture.

Few recent numerical studies investigated the impact of plant-scale horizontal heterogeneities on the mean canopy flow. These heterogeneities were either complex, resulting from a random distribution or from a high resolution scan of real canopy structures (Bohrer et al., 2009), or organized, representing canopies structured in rows such as in vineyards (Bailey and Stoll, 2013; Chahine et al., 2014). They all observed that the mean flow and turbulent coherent structures in plant-scale heterogeneous canopies share similar features with those in uniform canopies. On the other hand, the canopy structure affects the location of coherent structures (Bohrer et al., 2009; Bailey and Stoll, 2013; Chahine et al., 2014), and coherent

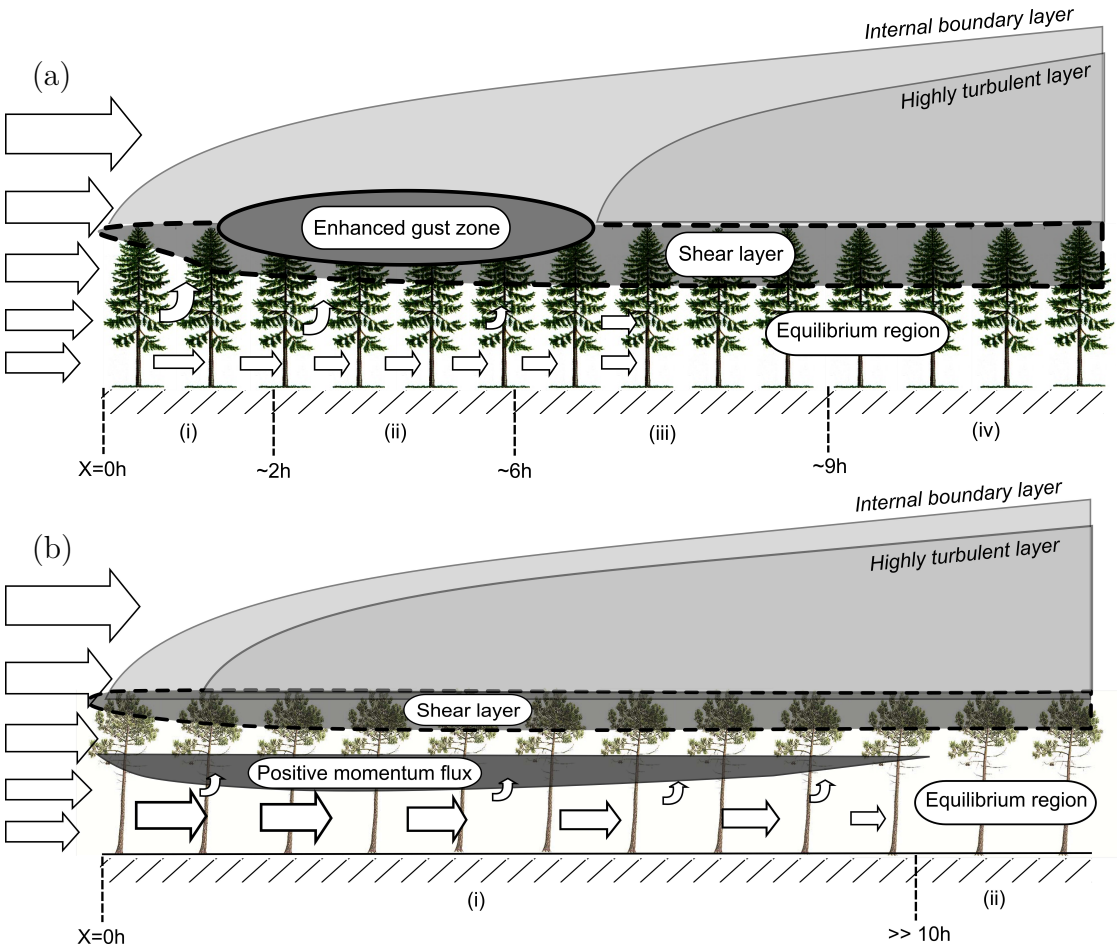

Figure 5.1: Idealized representation of the main characteristics of edge flow over forests with (a) a relatively uniform vertical foliage distribution and, (b) a deep and sparse trunk space (from Dupont et al., 2011).

structures penetrate deeper into the canopy, in presence of large gaps (about three canopy heights) (Bailey and Stoll, 2013). Dispersive fluxes are defined as spatial covariances between single-point, time-averaged quantities (Raupach and Shaw, 1982). In organized canopies, few studies reported dispersive momentum flux reaching up to 20% of the single-point momentum flux in the lower part of the canopy (Poggi et al., 2004; Bailey and Stoll, 2013). The dispersive fluxes were found higher in sparse canopies compared to dense canopies, where they were traditionally found insignificant ($< 1\%$, Kaimal and Finnigan, 1998).

To our knowledge, only Schlegel (2012) investigated the impact of plant-scale heterogeneities on an edge flow using high-resolution terrestrial LiDAR scan. Unlike canopy flow, they observed that the mean edge flow is significantly affected by plant-scale heterogeneities. However, the canopy heterogeneities were described

in two dimensions only, and the forest edge was located behind a small gap (only two canopy heights-long) instead of a wide open space. The impact of three-dimensional tree-scale heterogeneities on a forest leading edge flow has therefore not yet been fully assessed.

The aim of this paper is to investigate the impacts of three-dimensional tree-scale horizontal variabilities on the first-, second- and third-order moments of an edge flow, on the dispersive fluxes, and to compare them against an equivalent homogeneous edge forest. To that purpose, a large-eddy simulation (LES) is performed on a forest edge site in Denmark where the three-dimensional structure of the forest has been determined from helicopter-based LiDAR scans (Boudreault et al., 2014b). Simulations are evaluated against high-frequency wind measurements performed on this site across the edge (Dellwik et al., 2014). After presenting the model, the site and the numerical set-up in Section 5.2, the model is evaluated against measurements, and the edge flow over the horizontally heterogeneous forest and its equivalent homogeneous forest are compared in Section 5.3, together with the evaluation of dispersive fluxes. We finally move to Discussion and conclusion (Section 5.4).

5.2 Methods

5.2.1 LES model

The Advanced Regional Prediction System (ARPS) (version 5.1.5) solver is used in this study. The code is based on a three-dimensional, non-hydrostatic compressible model formulation of the Navier-Stokes equations. The model allows to solve conservation equations for the three wind velocity components, pressure, potential temperature and water substance (water vapour, cloud water, rainwater, cloud ice, snow and graupel). Wind components and atmospheric state variables (air density, pressure and potential temperature) are split into a base state (hereafter represented by hat variables) and a deviation therefrom (starred variables), *i.e.* $\phi = \hat{\phi} + \phi^*$. The base state is assumed horizontally homogeneous, time invariant and hydrostatically balanced. Here, the atmosphere is assumed neutral and temperature effects are neglected. Details and validation cases can be found in Xue et al. (1995, 2000, 2001). The ARPS code is designed for weather systems prediction in meso-scale flows but was modified to simulate flows within vegetated canopies at fine-scales. This last version has been extensively validated against field and wind-tunnel measurements over homogeneous canopies (Dupont and Brunet, 2008b), over simple forest-clearing-forest patterns (*e.g.*, Dupont and Brunet, 2008a; Dupont et al., 2011), over a forested hill (Dupont et al., 2008), and over a waving crop (Dupont et al., 2010). The model is

briefly described in the following and the reader is referred to the above references for further details.

Large eddies of the turbulent flow are explicitly resolved whereas the motion of the smaller-scale eddies are modeled. The filtered Navier-Stokes equations are considered for this purpose. The sub-grid scale (SGS) stress tensor is modeled using a closed system of equations. Here, a transport equation of SGS-turbulent kinetic energy e and fixed length-scales l_h and l_v (1.5-equation closure model) were used to close the system. The filtered momentum equation writes

$$\frac{\partial \tilde{u}_i}{\partial t} + \tilde{u}_j \frac{\partial \tilde{u}_i}{\partial x_j} = R_D(\hat{u}_i - \tilde{u}_i) - \frac{1}{\hat{\rho}} \frac{\partial \tilde{p}^*}{\partial x_i} - \frac{\partial \tau_{ij}^s}{\partial x_j} - C_d a \sqrt{\tilde{u}_j \tilde{u}_j} \tilde{u}_i, \tag{5.1}$$

where the summation notation of the vectors and tensors is used. The overtilde indicates the filtered variables or grid volume-averaged variables, resulting from the grid filtering. In this equation, t is time and x_i ($x_1 = x$, $x_2 = y$, $x_3 = z$) refer to the streamwise, lateral, and vertical directions, respectively; u_i ($u_1 = u$, $u_2 = v$, $u_3 = w$) is the instantaneous velocity component along x_i; δ_{ij} is the Kronecker delta, p the air pressure and ρ the air density, respectively. The first term on the right hand side applies a Rayleigh damping forcing of the fluctuations $u_i^* = \tilde{u}_i - \hat{u}_i$ towards the base-velocity $\hat{u}_i$. The force is varied with height from $z = z_D$, up to the top of the domain z_T, using the parametric relationship R_D of Klemp and Lilly (1978),

$$R_D = \begin{cases} 0.0 & \text{for} \quad z < z_D, \\ \dfrac{\alpha_R}{2}\left(1 - \cos\left[\dfrac{\pi(z - z_D)}{(z_T - z_D)}\right]\right) & \text{for} \quad z \geq z_D, \end{cases} \tag{5.2}$$

with $\alpha_R = 0.1\ s^{-1}$. The Coriolis force is neglected as no significant dynamic effects of the earth rotation at the scale of the canopy edge were found by Dupont et al. (2011). The term containing the drag coefficient C_d and the frontal area density a (in $\mathrm{m^2\,m^{-3}}$) represents the effect of the canopy on the flow. The frontal area density is the average area of leafs, branches and stems opposing the wind flow per unit volume. Each cells of the grid are therefore assigned a net force proportional to C_d and a. Here, C_d is kept fixed to 0.2 and a varies spatially depending on the structure of the canopy. Canopy structures smaller than tree-scales are smoothed out while larger heterogeneities are kept explicitly resolved.

The SGS stress tensor τ_{ij}^s in Eq. 5.1 is approximated using the eddy-viscosity hypothesis:

$$\tau_{ij}^s = -((1 - \delta_{3j})\nu_{t,h} + \delta_{3j}\nu_{t,v}) \left(\frac{\partial \tilde{u}_i}{\partial x_j} + \frac{\partial \tilde{u}_j}{\partial x_i}\right), \tag{5.3}$$

where $\nu_{t,h}$ and $\nu_{t,v}$ are respectively the horizontal and vertical eddy viscosities. Using relationships for the product of a velocity scale $\sqrt{e}$ and a horizontal and

vertical length scales, l_h and l_v, respectively, $\nu_{t,h}$ and $\nu_{t,v}$ can be approximated as,

$$\nu_{t,h} = 0.1\sqrt{e}l_h, \tag{5.4}$$
$$\nu_{t,v} = 0.1\sqrt{e}l_v. \tag{5.5}$$

The length scales are obtained from the grid spacing as,

$$l_h = \sqrt{\Delta x \Delta y}, \tag{5.6}$$
$$l_v = \Delta z, \tag{5.7}$$

and the velocity scale from the transport equation of the SGS turbulent kinetic energy e

$$\frac{\partial e}{\partial t} + \tilde{u}_j \frac{\partial e}{\partial x_j} = -\tau^s_{ij}\frac{\partial \tilde{u}_i}{\partial x_j} + \frac{\partial}{\partial x_j}\left(2((1-\delta_{3j})\nu_{t,h} + \delta_{3j}\nu_{t,v})\frac{\partial e}{\partial x_j}\right) - C_\epsilon \frac{e^{3/2}}{l_v} - 2C_d a\sqrt{\tilde{u}_j\tilde{u}_j}e, \tag{5.8}$$

where C_ϵ is 3.9 at the lowest model level and 0.93 above, according to Deardorff (1980) and Moeng (1984). The terms on the right-hand side of Eq. 5.8 represent respectively the dynamic shear production, the buoyancy production, the turbulent transport, the dissipation and the SGS-TKE cascade terms. The SGS equations above are here stated for completion. For the second-order moments, the magnitude of the SGS fluxes were at most 3% of the magnitude of the resolved fluxes, except near the forest floor. Therefore, only the resolved components of the fluxes are shown in the article as the SGS components were considered negligible.

5.2.2 Field experiment

A field experiment was conducted between 3 June and 12 September 2008 at a forest edge located on the Falster island in Denmark. The forest is approximately 24 m height (h) and is mostly composed of European beech trees (*Fagus sylvatica*) of about 75-year-old. The forest has a dense crown layer and a sparse trunk space, with tree frondescence usually occurring early May. Two 45.9 m height masts equipped with sonic anemometers were mounted, one (mast M1) in the upwind open grass field at approximately $1.5h$ from the forest leading edge (54°45.790N, 12°2.116E), and the second one (mast M2) inside the forest at approximately $1.5h$ from the edge (54°45.778N, 12°2.181E) (see Fig. 5.2a). Wind statistics, including first- to third-order moments, obtained from sonic measurements, were presented in Dellwik et al. (2014) for near-neutral condition and mean wind direction toward the forest. The reader can refer to this paper to obtain a more detailed description of the instrumentation and of the data analysis.

5.2.3 Description of numerical simulations

The three-dimensional flow over and inside a clearing-forest interface is simulated for the Falster site. This simulation is referred hereafter as the heterogeneous-edge case. In the simulation, the atmosphere is neutrally stratified and the mean wind direction is perpendicular to the edge, corresponding to the near-neutral data analysed in Dellwik et al. (2014) and to the 285° wind sector from North. The simulations are run using a time-step of $\Delta t = 0.03\,\mathrm{s}$. The computational domain extends over $960 \times 480 \times 250\,\mathrm{m}$ with $480 \times 240 \times 140$ grid points in the x, y and z directions, respectively, including a 480 m long clearing, infinite in the lateral direction, located upwind from the forest. The roughness length of the clearing surface and of the forest ground is set to 0.03 m. The grid resolution is 2 m in the horizontal and 1 m below 84 m in the vertical. Above this height, the grid is stretched. The same grid configuration and resolution was applied by Dupont et al. (2011) in a similar forest edge study. Here, the study is focused on

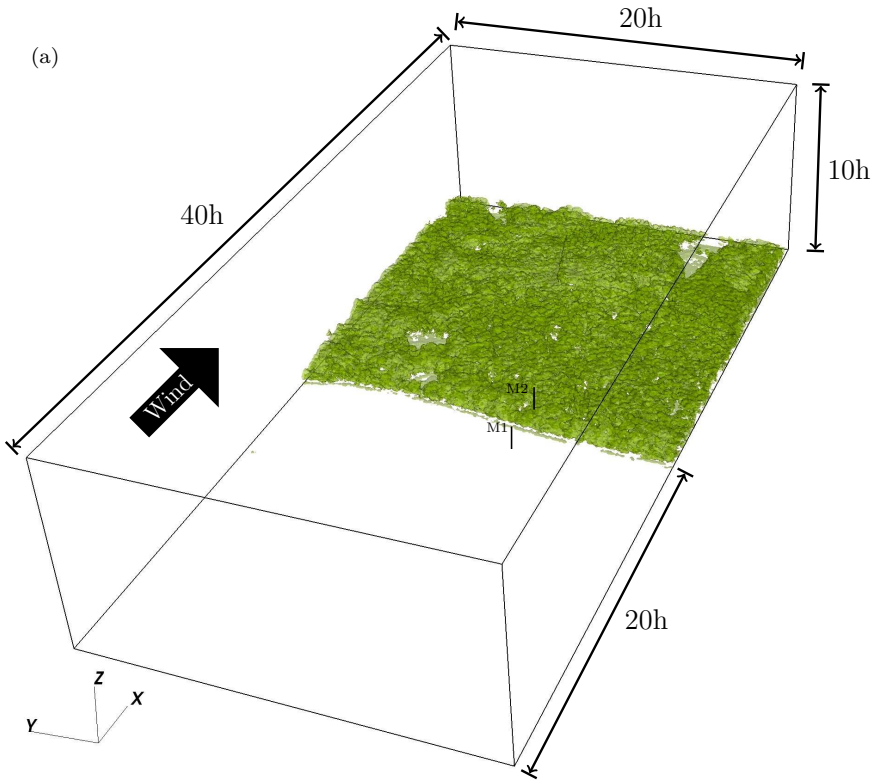

Figure 5.2: (a) Three-dimensional iso-contours of the frontal area density (a) of the Falster island forest as retrieved from high resolution aerial LiDAR scans and as considered in the LES computational domain. (*continued on next page*)

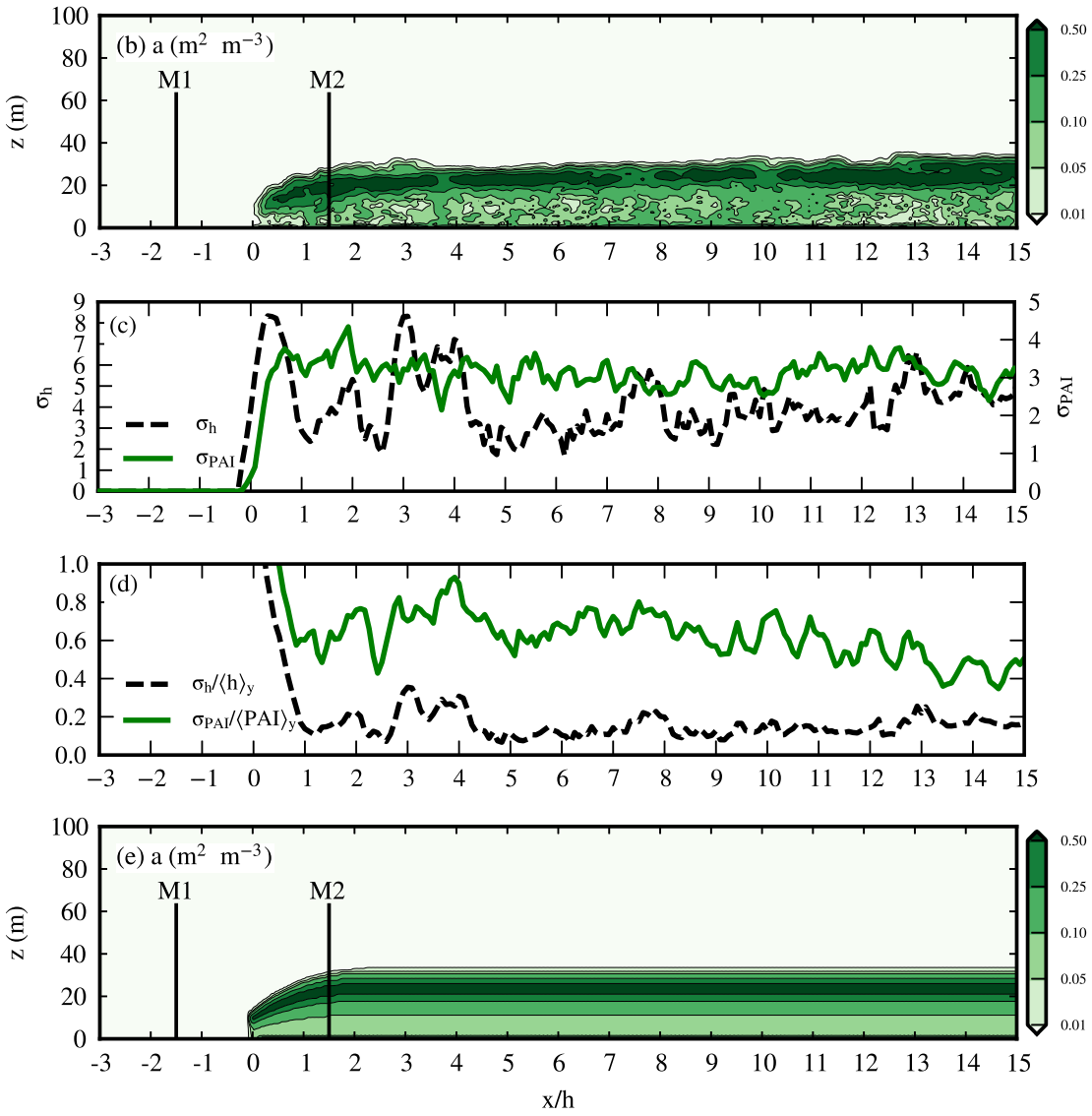

Figure 5.2: (*continued*) (b) y-averaged frontal area density of the forest. (c) Standard deviations of the forest PAI (σ_{PAI}) and forest height (σ_h) with distance from the edge. (d) Same as (c) but normalized by y-averaged PAI and canopy height. (e) Frontal area density of the forest considered in the homogeneous-edge case. M1 and M2 indicate the locations of the measurement masts.

the flow near-above the canopy and inside, where coherent structures developing at canopy top are dominant. The influence of meso-scale structures is neglected for this neutrally stratified atmosphere (Dupont and Brunet, 2009). The LES resolution and the height of the domain are therefore prescribed from a compromise between computational effort, and the adequate resolution of the coherent eddies

dominating the flow.

The inlet, outlet and lateral boundary conditions applied on the LES domain are periodic. The periodicity of forest density is not treated in the lateral direction but is believed not to influence the solution at the center of the domain near the masts, where the study is focused. Near and at the upper boundary, the Rayleigh damping layer is applied over a 54 m depth from top, using a constant base-state velocity $\hat{u}$ prescribed according to the well-known log-law relationship (where $u_* = 0.3\,\mathrm{m\,s^{-1}}$, $\kappa = 0.4$ and $\hat{v} = \hat{w} = 0$). At the bottom boundary, the momentum flux is parameterized using a bulk aerodynamic drag law. More details about these boundary conditions can be found in the ARPS user manual (Xue et al., 1995).

The frontal area density a of the forest is deduced from a forest scan performed in August 2013 from an helicopter with a mounted LiDAR. The scan was executed at a high reflection density (> 10 reflections/m^2) to reveal the detailed structure of the canopy interior. The reflections of the LiDAR pulses on the canopy formed a point cloud, where each pulse had a x, y and z coordinates. This point cloud was transformed into a three-dimensional grid of a values, based on a method using radiation transfer properties inside canopies (Boudreault et al., 2014b). In this method, the bin radius and the horizontal resolution were set to 2 m, and the vertical resolution to 1 m. Fig. 5.2a presents three-dimensional iso-contours of a, and Fig. 5.2b shows a values in the $x - z$ plane crossing M1 and M2 masts. The lateral variability of PAI (σ_{PAI}), or the vertically summed frontal area density, appears relatively homogeneous along the edge region, around 3, while the canopy height exhibits a maximum standard deviation (σ_h) at the edge and between $x =$ 2.5 to $4.5h$ of about 8 m (Fig. 5.2c). When normalized by their mean values, both standard deviations of PAI and h exhibit an homogeneous trend along the edge, representing 60% and 20%, respectively (Fig. 5.2d).

The wind experiment was performed 5 years earlier than the forest scan so we evaluated the canopy growth during this period. The forest PAI was measured near the mast M2 during the wind experiment with a plant canopy analyzer (PCA) (LAI-2000, LI-COR, Inc., Lincoln, Nebraska). Similar values as the ones retrieved from the LiDAR ($PAI \approx 6$) 5 years later, were obtained. Furthermore, the tree growth between 2008 and 2013 was estimated to be 1 m for 75-year-old trees, which is within the uncertainty of the LES vertical grid resolution (1 m). For these reasons, we found it appropriate to use the canopy structure deduced from the 2013 scan to perform LES, and to evaluate the results against the 2008 wind measurements.

An additional simulation, similar as the heterogeneous-edge case but with an horizontally homogeneous forest, is performed. This simulation is referred as the homogeneous-edge case. To construct this homogeneous forest, two regions are distinguished: the leading edge region, between $x = 0$ and $2h$, and the far-edge

region, $x > 2h$. In this latter region, the foliage vertical distribution is deduced by horizontally averaging a from 2 to $20h$ in the x direction and over $10h$ in the y direction, centred on mast M2. In the leading edge region, the averaged a vertical distribution of the far-edge region is scaled down with the y-averaged tree height to keep the same edge shape as the heterogeneous-edge case (Fig. 5.2e). The ratio of total PAI between the heterogeneous- and homogeneous-edge case is 1:0.93. The leading edge in the homogeneous-edge case is perfectly straight whereas it shows a slight y-curvature in heterogeneous-edge case. The y-curvature is retained in the heterogeneous-edge case simulation to perform a realistic comparison with the field experiment.

5.2.4 Statistical data analysis

To characterize the edge flow dynamics, we shall first introduce averaging operators used for the statistical treatment of the LES data.

The time-averaging operator, denoted by an overbar, and the departure from the time-average, denoted by a prime, are defined as

$$\bar{\phi}_i = \frac{1}{T}\int_0^T \phi_i(t)\mathrm{d}t, \quad \phi_i' = \phi_i - \bar{\phi}_i, \tag{5.9}$$

where T is the time period over which the LES data is averaged. In our simulations, instantaneous time samples of velocities are gathered each 20 s after the flow is reaching ergodicity, over a time period of $T = 15000$ s (750 samples) for the heterogeneous edge-case, and $T = 6000$ s (300 samples) for the homogeneous edge-case. The same sampling approach was applied in the edge flow analysis of Dupont and Brunet (2008a, 2009) and Dupont et al. (2011), with the difference that a larger sample size was here gathered (750 samples for the heterogeneous edge-case compared to 90 in Dupont et al.'s studies), to ensure smooth statistics in the results where time-averaged fields are shown only.

After the time-averaging operation is performed, the horizontal-averaging operator, denoted by angled brackets, and the departure from the horizontal-average, denoted by a double-prime, are defined as

$$\langle\bar{\phi}_i\rangle = \frac{1}{A}\iint_R \bar{\phi}_i(x,y,z)\mathrm{d}x\mathrm{d}y, \quad \bar{\phi}_i'' = \bar{\phi}_i - \langle\bar{\phi}_i\rangle, \tag{5.10}$$

where R is a region in the $x-y$ plane. The horizontal-averaging is performed locally around each grid point, over regions of $A = x \times y = h \times 5h$, using a total number of 720 time-averaged spatial samples. The choice of this averaging-area is justified in Section 5.3.6.

The y-averaging operator of time-averaged wind fields, denoted by $\langle\cdot\rangle_y$, is defined as

$$\langle\bar{\phi}_i\rangle_y = \frac{1}{D}\int_{-D/2}^{D/2}\bar{\phi}_i \mathrm{d}y, \tag{5.11}$$

where D is $10h$ centred around the experimental masts. The total domain width ($20h$) is not used for the y-averaging operator to avoid the influence of the large clearings present along $y = 14h$ (Fig. 5.7a), and because this portion of the domain show relatively constant y-variability in the canopy structure, as shown in Fig. 5.2c and d. The spatial standard deviation of a given quantity, σ_ϕ, is defined according to the y-direction over the same distance D as the y-averaging operator.

Different statistical quantities are constructed from the averaging operations introduced above. For example, the single-point, time-averaged covariance of the velocities, or turbulent fluxes, and the spatial covariance between time-averaged velocities, or dispersive fluxes, are respectively assembled as $\overline{u_i' u_j'}$ and $\langle\bar{u}_i''\bar{u}_j''\rangle$.

5.3 Results

In this section, the inflow conditions for the heterogeneous, the homogeneous edge-case and the wind field experiment upwind of the edge are first compared (Section 5.3.1). The comparison is followed by an evaluation of the LES model against the measurements (Section 5.3.2). A two-dimensional view of the edge flow is then presented and compared to the one obtained from the homogeneous-edge case (Section 5.3.3). Finally, the impacts of canopy horizontal heterogeneities on the mean wind dynamics is analysed from a three-dimensional view of the mean edge flow (Section 5.3.4), from spatial standard deviations of flow statistics (Section 5.3.5) and from dispersive fluxes (Section 5.3.6).

5.3.1 Inflow conditions

The ratios of the root-mean-square of the turbulent velocity fluctuations to the mean velocity, or turbulence intensities TI, are compared at M1 for the heterogeneous edge-case, the homogeneous edge-case and for the field measurements (Fig. 5.3).

The inflow conditions upwind the edge are found different between the measurements (20% at 20 m) and the simulations (30% and 35% at 20 m for the heterogeneous and the homogeneous edge-case, respectively). In the LES, periodic conditions have been used, meaning that the outflow from the forest is reintroduced at the inlet boundary of the domain. Although the clearing length upstream of the forest is about $20h$ long, a wake effect from the upwind forest (or downwind edge) is still present at the forest leading edge. This is the reason for the high TI

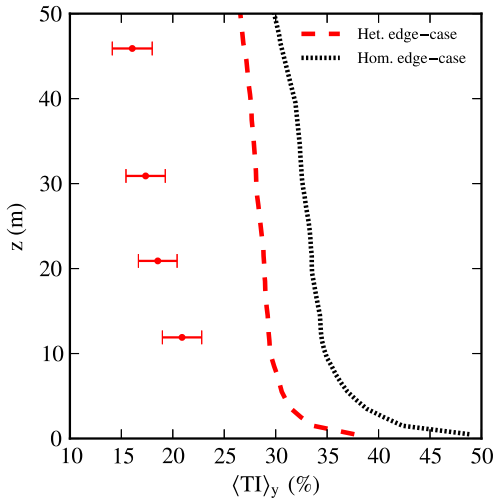

Figure 5.3: At M1, inflow profiles of turbulence intensity for the observations (circle red dots with error bars) and y-averaged $\left(\langle TI\rangle_y = \sqrt{\frac{2}{3}\langle E\rangle_y}/\langle\overline{u}\rangle_y\right)$ for the heterogeneous- (red dashed line) and homogeneous-edge case (black dotted line).

in the simulations. These differences can have an impact on the model evaluation against the measurements presented in Section 5.3.2, and suggest that the LES setup may need improvement. Nevertheless, this does not compromise the study in general, which is focused on the impacts of canopy heterogeneity.

A 5% higher turbulence intensity is observed for the homogeneous-edge case compared to the heterogeneous-edge case. The difference could be related to the missing density at the location of the y-curvature of the edge, to the fact that the total PAI between both cases are not equivalent at the forest scale, or to an effect of canopy heterogeneity. The total effect of the forest-clearing pattern on the flow is beyond the scope of the present study, where the effect of the plant-scale heterogeneity on the edge flow is in focus. The specific reasons for the difference in turbulence intensity should nevertheless be clarified in more detail in a future study.

5.3.2 Model evaluation against field measurements

Simulated and measured statistical wind profiles located at the upwind and downwind masts from the forest edge are compared (Fig. 5.4): streamwise velocity ($\overline{u}$), turbulent momentum flux ($\overline{u'w'}$), standard deviations of the three wind velocity components (σ_u, σ_v, σ_w), turbulent kinetic energy (E), and skewnesses of u and w (Sk_u, Sk_w). Profiles are normalized with a reference velocity (u_{ref}) and a reference friction velocity ($u_{*,ref}$) defined at 30.9 m height on mast M1. In Fig. 5.4, the shaded areas surrounding the LES lines and the error bars around experimental

dots represent the standard deviations between 10 min periods. The temporal variabilities of the LES wind profiles are comparable to the measurements, therefore indicating similar variability in both datasets.

Mean wind profiles obtained from the model show typical characteristics of a flow above a bare soil at M1 and a flow over a forest canopy at M2. The velocity profile exhibits a similar shape from the surface at M1 and from the near canopy top at M2. Within the canopy, the velocity profile has an inflection point at

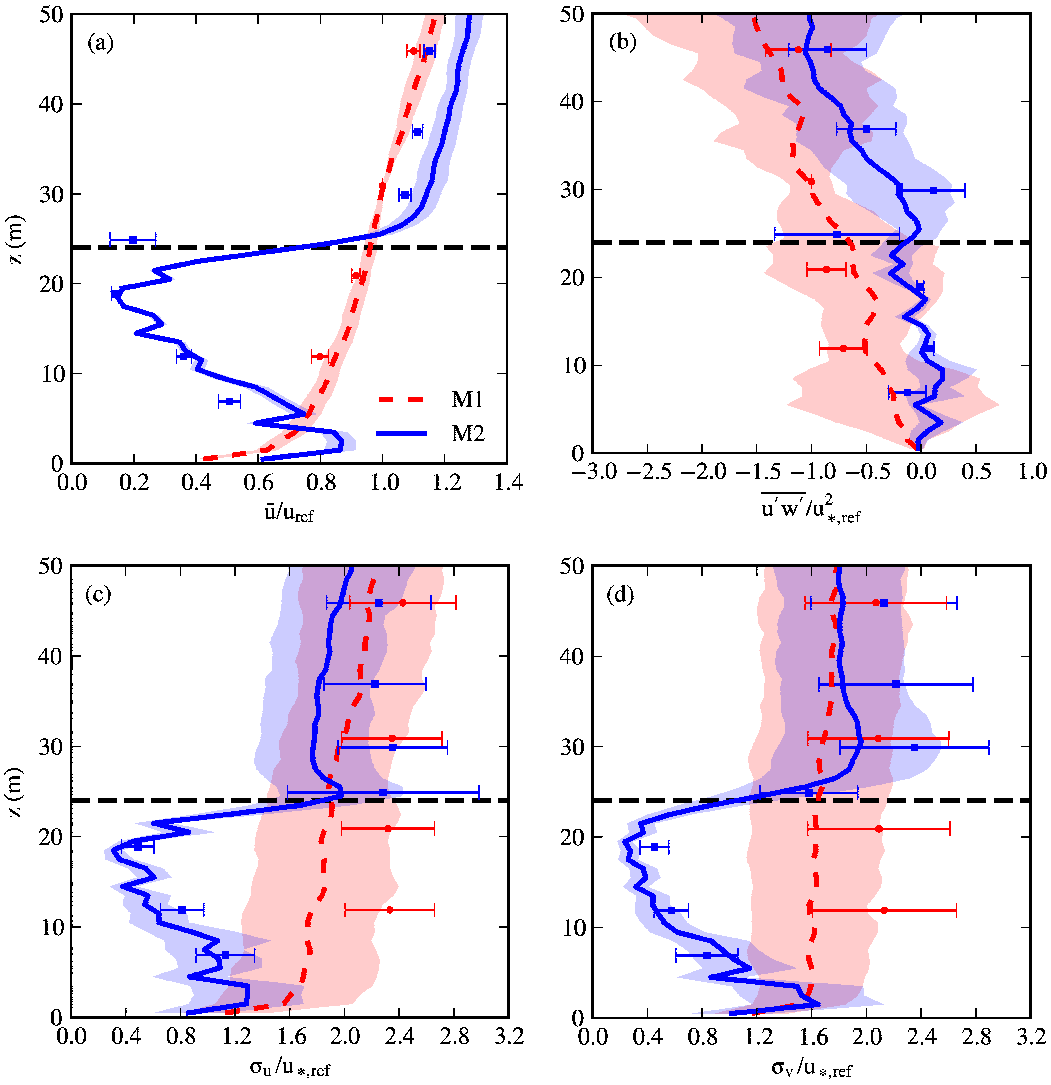

Figure 5.4: Observed (dots: red circles at M1 and blue squares at M2) and simulated (heterogeneous-edge case, lines: red dashed-line at M1 and blue solid line at M2) time-averaged vertical profiles of streamwise wind velocity $\overline{u}$ (a), turbulent momentum flux $\overline{u'w'}$ (b), standard deviations of the three wind velocity components σ_u (c), σ_v (d), and (*continued on next page*)

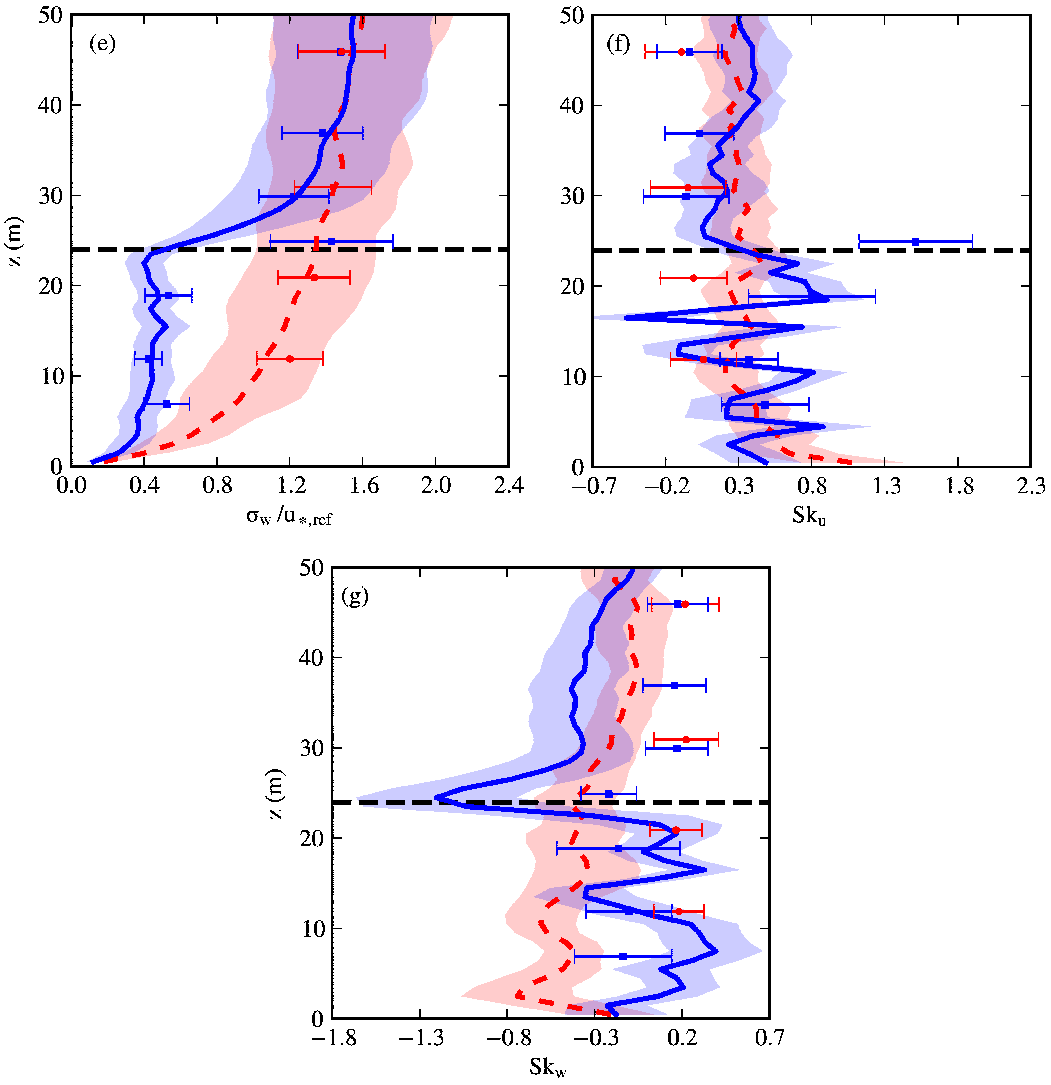

Figure 5.4: (*continued*) σ_w (e), u and w skewnesses Sk_u (f) and Sk_w (g), upwind (M1) and downwind (M2) the forest leading edge. All variables are normalized with the reference streamwise wind velocity, u_{ref}, and the friction velocity, $u_{*,ref}$, located at 30.9 m height on mast M1 ($u_{ref} = 8.62$ and $u_{*,ref} = 0.54$ m s^{-1} for the observed data, and $u_{ref} = 1.77$ and $u_{*,ref} = 0.54$ m s^{-1} for the simulations). The error bars (observation) and shaded areas (simulation) show the standard deviations between 10 min periods. The horizontal dashed black line indicates the canopy top.

the canopy top, the velocity reaches a minimum in the upper canopy where the density is highest, and increases within the understory (Fig. 5.4a). As a result of the periodic conditions, the turbulent momentum flux is unexpectedly not constant with height at M1 and M2, and slightly decreases (Fig. 5.4b). The non-constant behaviour is also shown in the measurements, although less pronounced at M1.

The magnitude of $\overline{u'w'}/u^2_{*,ref}$ is lower at M2. The standard deviations σ_u and σ_v are almost constant with height at M1, while they reach a minimum at M2 in the upper canopy and increase below as the wind velocity (Fig. 5.4c and d). The standard deviation σ_w decreases near the surface at M1 and at canopy top at M2, and is almost constant within the canopy (Fig. 5.4e). Skewness profiles are almost constant with height at M1 and show a significant minimum at canopy top for Sk_w (Fig. 5.4g) and a slight maximum in the upper canopy for Sk_u (Fig. 5.4f). All statistics show vertical variability within the canopy, where it is most significant for skewness profiles. The variability is found independent of the integration time and is rather attributed to the local structure of the heterogeneous canopy.

Compared with measurements, the LES is able to reproduce the main characteristics of the wind dynamics at both locations. The main differences occur for σ_u, σ_v and Sk_w. The profiles of $\sigma_u/u_{*,ref}$ and $\sigma_v/u_{*,ref}$ are slightly underestimated by the model for all points at M1 and only above the canopy at M2. Sk_w is negative at M1 and above the canopy at M2 while measurements indicate positive values. Since these discrepancies are observed at both locations, they could potentially be explained by differences in inflow condition between the simulation and the field experiment, as is suggested by the 10% higher turbulence intensity for the simulation (Fig. 5.3). The flow dynamics at M1 are not responding exactly to a boundary-layer flow over a bare surface, but to a residual canopy wake created from the LES periodic conditions (see Section 5.3.1). The main effect of the residual canopy wake upwind the forest is to enhance the turbulent momentum flux (Fig. 5.4b) and the mean wind velocity (Fig. 5.4a), where the ratios of the standard devations with the friction velocity are too low compared to measurements (Fig. 5.4c and Fig. 5.4d). The wake effect of the far upwind forest also explains the non-constant profile of $\overline{u'w'}$ at M1. The reader is referred to Mann and Dellwik (2014) for an explanation of the non-constant behaviour in the measurements. At the measurement location right above the canopy at M2, sharp transitions in the turbulent flow occurs (see Dellwik et al., 2014, for discussion) which are not resolved by the LES grid. Other (most important) differences between simulation and measurements should be related to uncertainty on the exact $x-y$ position of the mast, the variabilities of canopy structures smaller than the resolution of the LES, or to the 5-year period between wind and canopy structure measurements. Despite these differences, the LES simulations are used to study the impacts of canopy heterogeneity on the edge flow.

5.3.3 Two-dimensional view of the edge flow

To illustrate the simulated flow over the whole forest edge, Fig. 5.5 shows the y-averaged $x-z$ planes of the mean streamwise and vertical wind velocity components ($\langle\overline{u}\rangle_y$ and $\langle\overline{w}\rangle_y$), turbulent kinetic energy ($\langle E\rangle_y$), turbulent momentum flux

($\langle\overline{u'w'}\rangle_y$), correlation coefficient between u and w ($r_{uw} = -\langle\overline{u'w'}\rangle_y / (\langle\sigma_u\rangle_y\langle\sigma_w\rangle_y)$), and skewnesses of u and w ($\langle Sk_u\rangle_y$ and $\langle Sk_w\rangle_y$), for the heterogeneous-edge case. The y-averaging distance is shown in Fig. 5.7a. The variables are normalized with an upwind reference velocity $\langle u_{ref}\rangle_y$ and a upwind reference friction velocity $\langle u_{*,ref}\rangle_y$ defined at 30.9 m height at mast M1. Compared to Fig. 5.4a-g, these reference variables have been y-averaged (Eq. 5.11). For comparison, Fig. 5.6 presents the same variables, but for the homogeneous-edge case. Since the inflow conditions differ between the two edge-cases (see Section 5.3.1), this normalization allow for an analysis of the differences due to canopy heterogeneity only.

Overall, the mean edge flow characteristics of the heterogeneous-edge case show more similarities with the edge flow over a mature maritime pine forest (Fig. 5.1b) than with the edge flow over a forest with uniform vertical foliage distribution (Fig. 5.1a). A deflection of the flow at the edge with a wind jet in the sub-canopy layer is simulated. This wind jet decreases slowly with distance from the edge. A layer with positive turbulent momentum flux develops from the edge, below the base of the foliated layer, associated to the sub-canopy wind jet. A turbulent region develops above the canopy from about $3h$ downwind from the edge due to the high wind shear. The turbulence is rapidly damped within the canopy. In the heterogeneous edge-case, no well-defined enhanced gust zone is observed, only a constant maximum of Sk_u at the canopy top starting from the edge. At about $3h$ from the edge, the correlation coefficient r_{uw} adjusts with the canopy to a maximum of about 0.5 at canopy top, a value usually observed in canopy flow (Finnigan, 2000). This similarity with a mature maritime pine forest is explained by the sparse trunk space of our forest site, although the trunk space is not as deep as in Dupont et al.'s 2011 site.

The mean edge flow characteristics of the homogeneous-edge case exhibit similar characteristics as the one in the heterogeneous-edge case (Fig. 5.6). The main differences are related to the weaker flow penetration within the canopy from the edge, which leads to (1) a larger flow tilt angle at the edge, (2) a faster decrease of the sub-canopy wind jet with distance from the edge, (3) a lower level of turbulence within the canopy, (4) a subtle faster flow above the canopy between $x = 2h$ and $5h$, (5) a lower Sk_u at canopy top and within the canopy, with a subtle enhanced gust zone at canopy top between $x = 2h$ and $5h$, and (6) a lower Sk_w in the forest understory after $5h$. Additionally, the correlation coefficient r_{uw} adjusts faster, reaching a maximum at canopy top near the forest leading edge instead of $3h$ in the heterogeneous-edge case. The turbulent kinetic energy and turbulent momentum flux are lower within the internal boundary layer above the canopy but this could be related to differences in inflow conditions. To the end, the flow in the homogeneous-edge case is intermediate between an edge flow in a forest with uniform vertical foliage distribution, and an edge flow in a forest with a foliated

layer concentrated in the upper canopy.

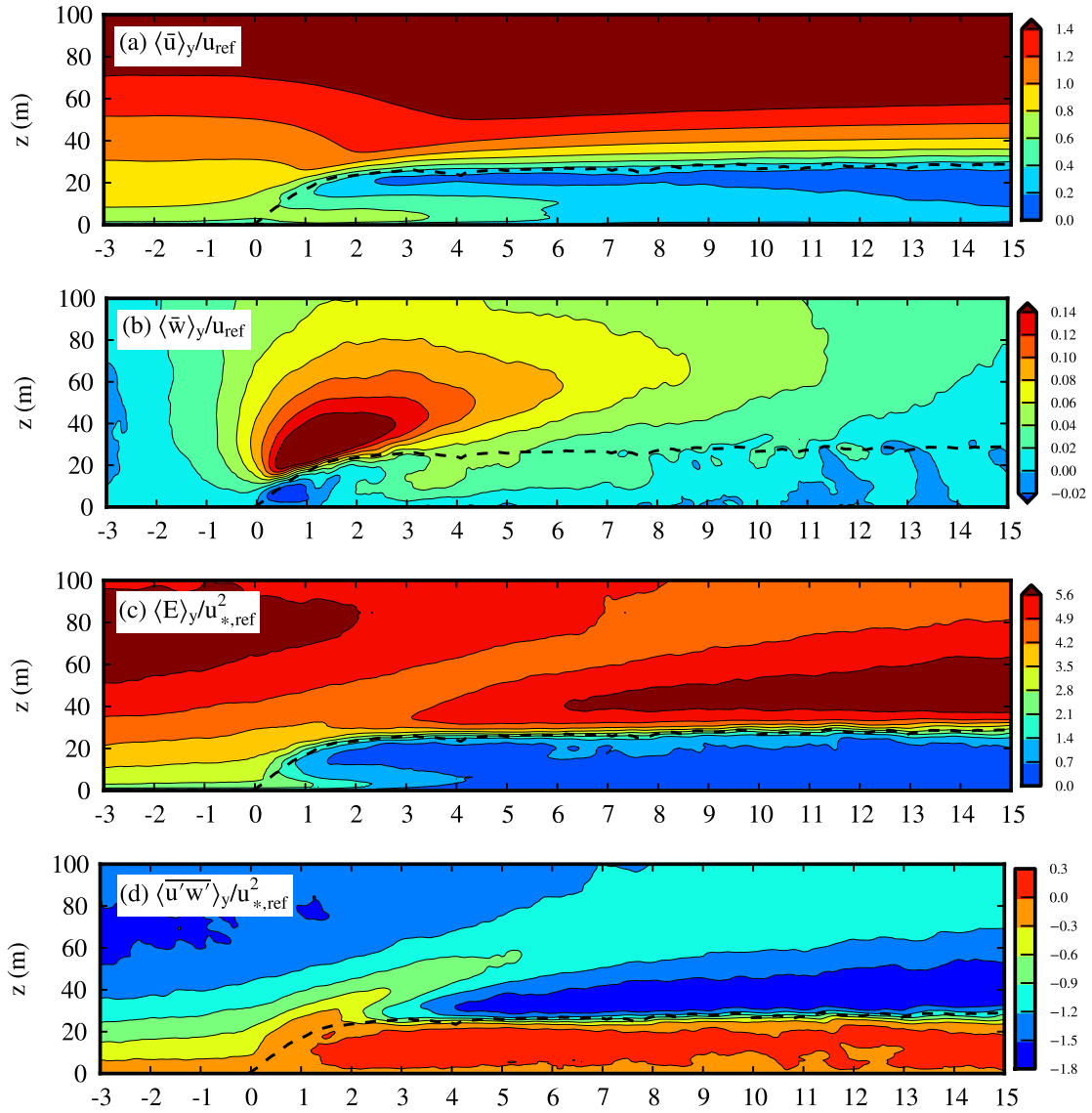

Figure 5.5: Time- and y-averaged edge flow statistics as simulated for the heterogeneous-edge case: (a) streamwise velocity, (b) vertical velocity, (c) turbulent kinetic energy, (d) turbulent momentum flux, (*continued on next page*)

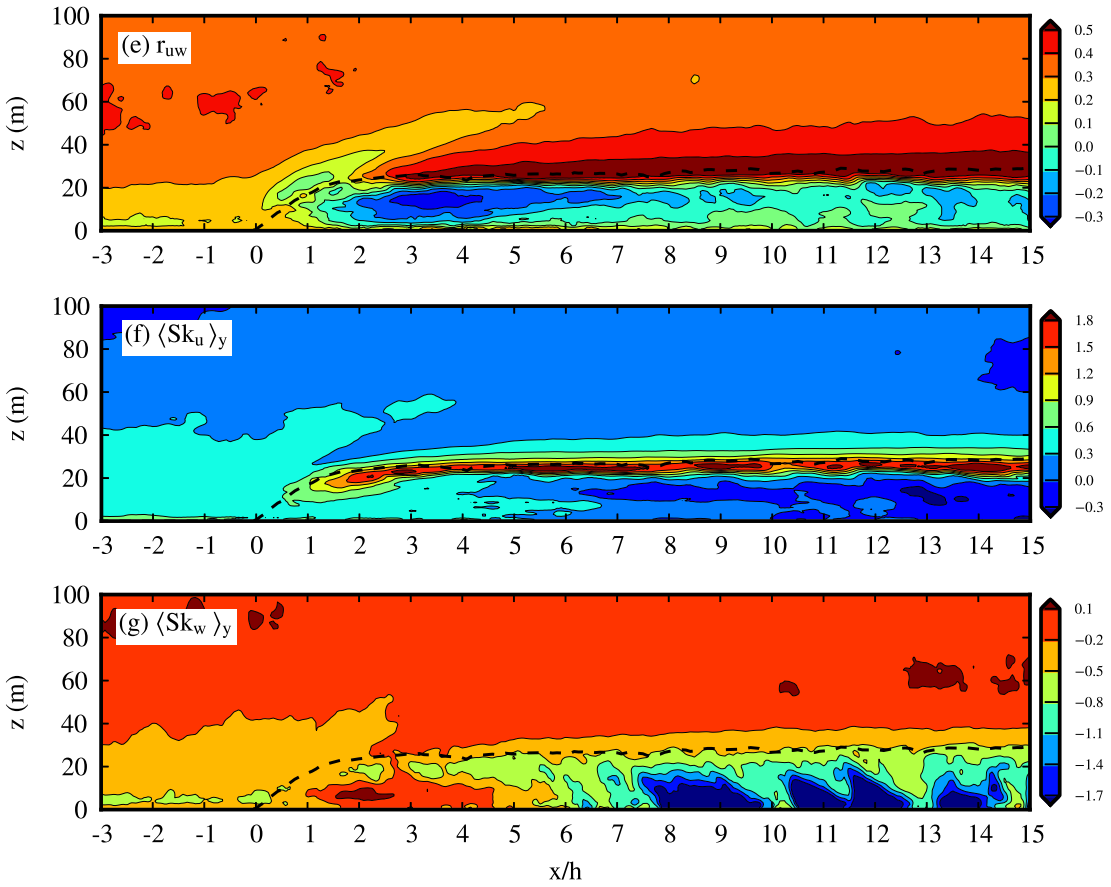

Figure 5.5: (*continued*) (e) coefficient of correlation, (f) skewness of the streamwise velocity, and (g) skewness of the vertical velocity. All variables are normalized with the reference streamwise wind velocity, $\langle u_{ref} \rangle_y$, and the friction velocity, $\langle u_{*,ref} \rangle_y$, located 30.9 m height on mast M1 ($\langle u_{ref} \rangle_y = 1.74$ and $\langle u_{*,ref} \rangle_y = 0.29$ m s^{-1}). The black dashed-line indicate the y-averaged tree height.

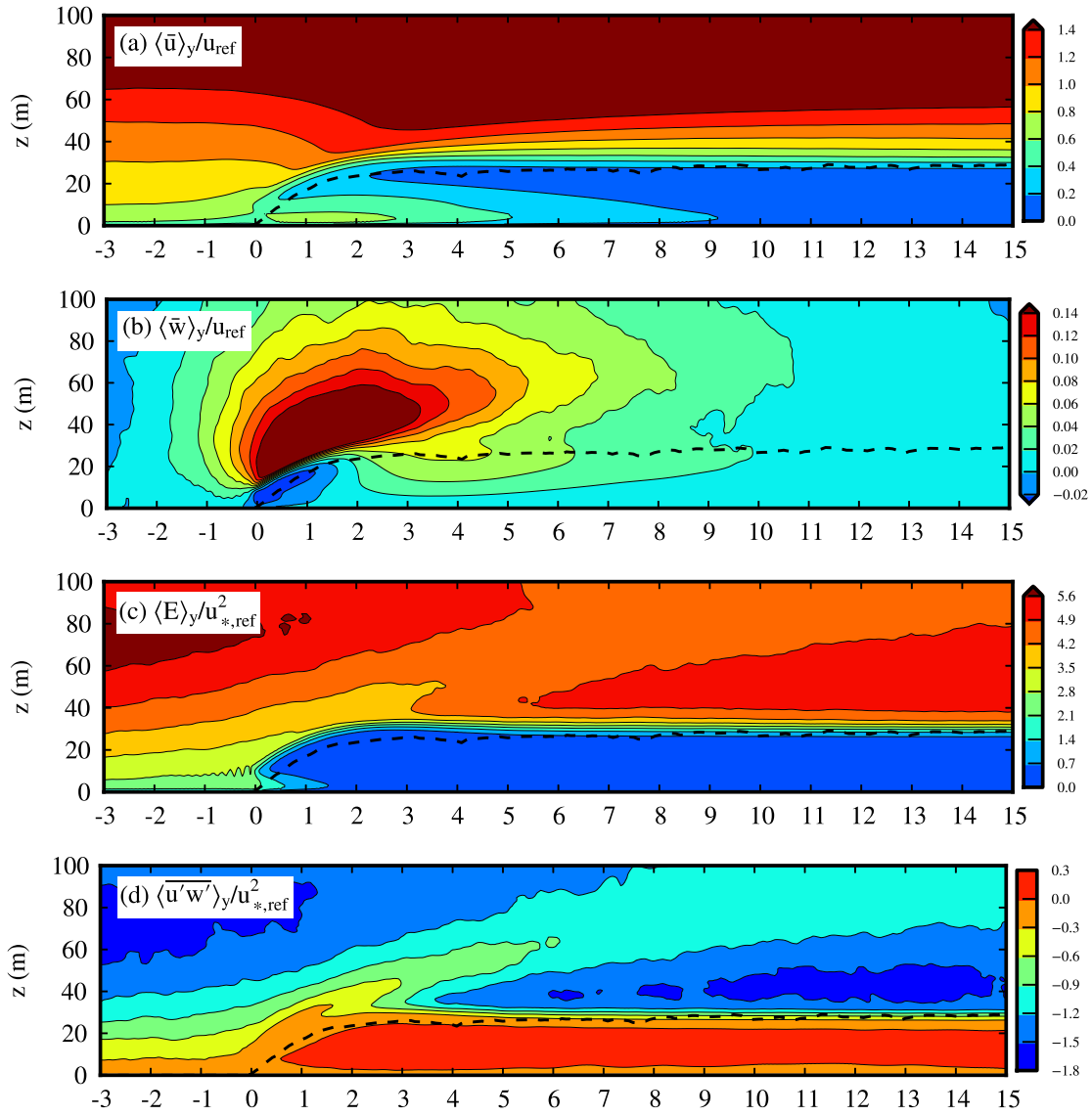

Figure 5.6: Same as Figure 5.5, but for the homogeneous-edge case (*continued on next page*).

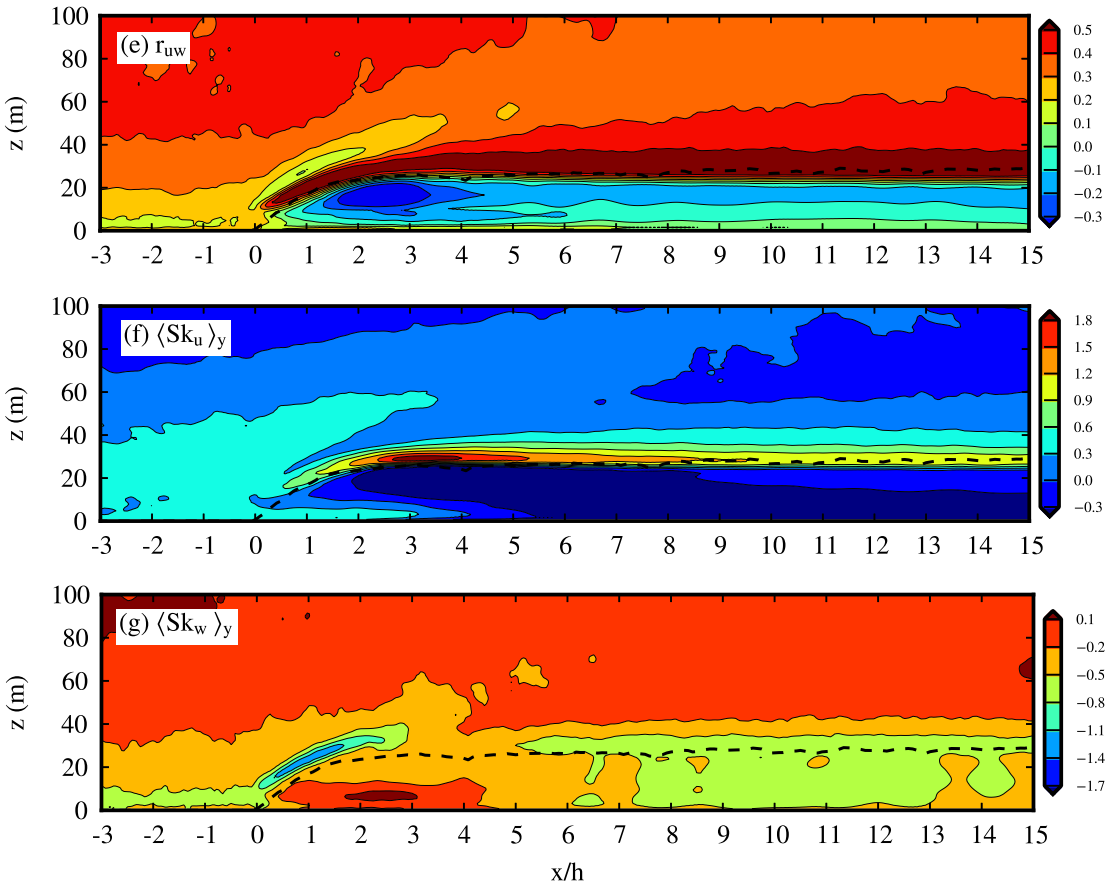

Figure 5.6: (*continued*) Same as Figure 5.5, but for the homogeneous-edge case ($\langle u_{ref} \rangle_y = 1.60$ and $\langle u_{*,ref} \rangle_y = 0.31$ ms^{-1}).

5.3.4 Three-dimensional view of the edge flow

Statistics of the time-averaged flow in the $x-y$ plane at $z = h/2$ are presented in Fig. 5.7 for the heterogeneous-edge case. This height has the advantage of showing both the flow penetration from the edge and the exchange with the above atmosphere through coherent structure penetration. As in previous figures, variables are normalized with u_{ref} and $u_{*,ref}$. All statistics show spatial variabilities in the streamwise and spanwise directions while statistics from the homogeneous-edge case (figure not shown) exhibit only a smooth streamwise variation in the edge region. These spatial variabilities are therefore explained by the horizontal heterogeneous structure of the canopy.

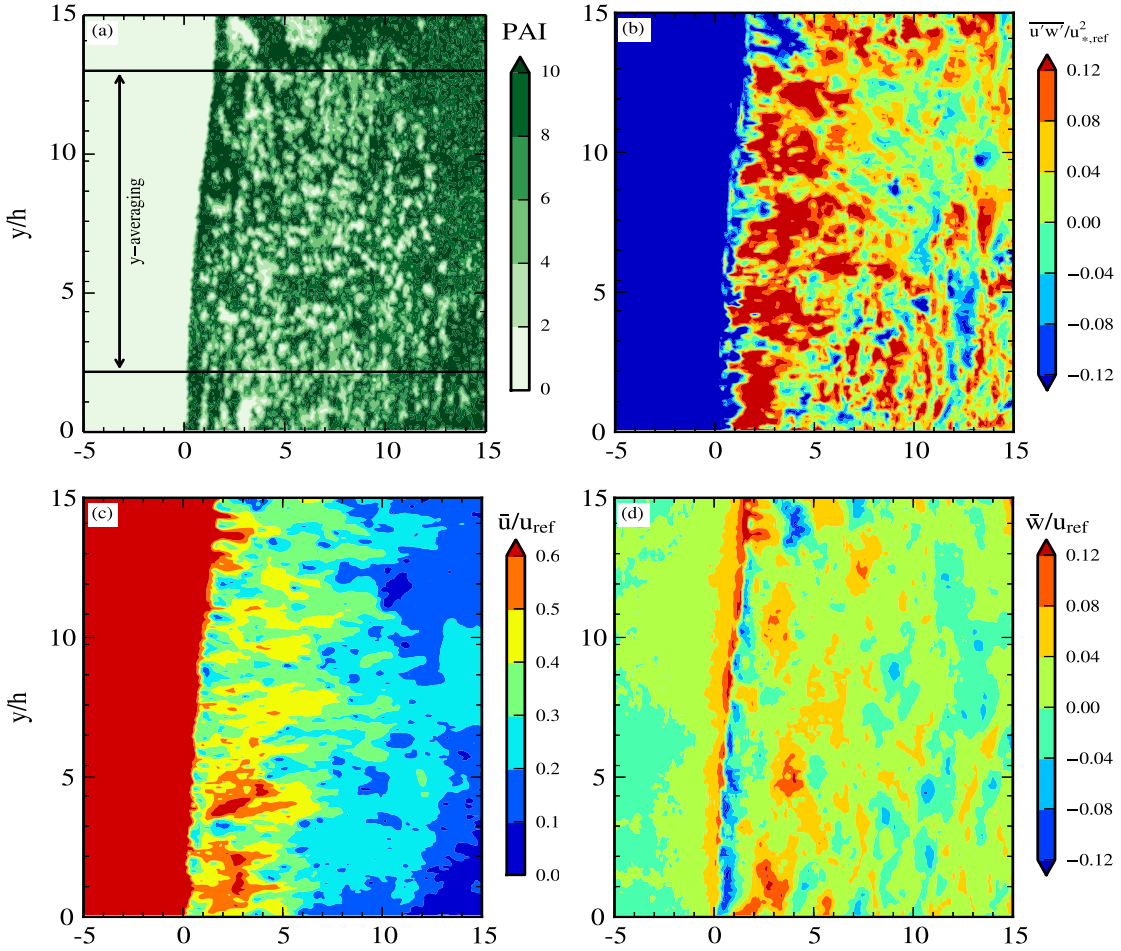

Figure 5.7: (a) Vertical integrated plant area index (PAI). Time-averaged edge flow statistics at $z = h/2$ as simulated for the heterogeneous-edge case: (b) turbulent momentum flux, (c) streamwise velocity, (d) vertical velocity, (*continued on next page*)

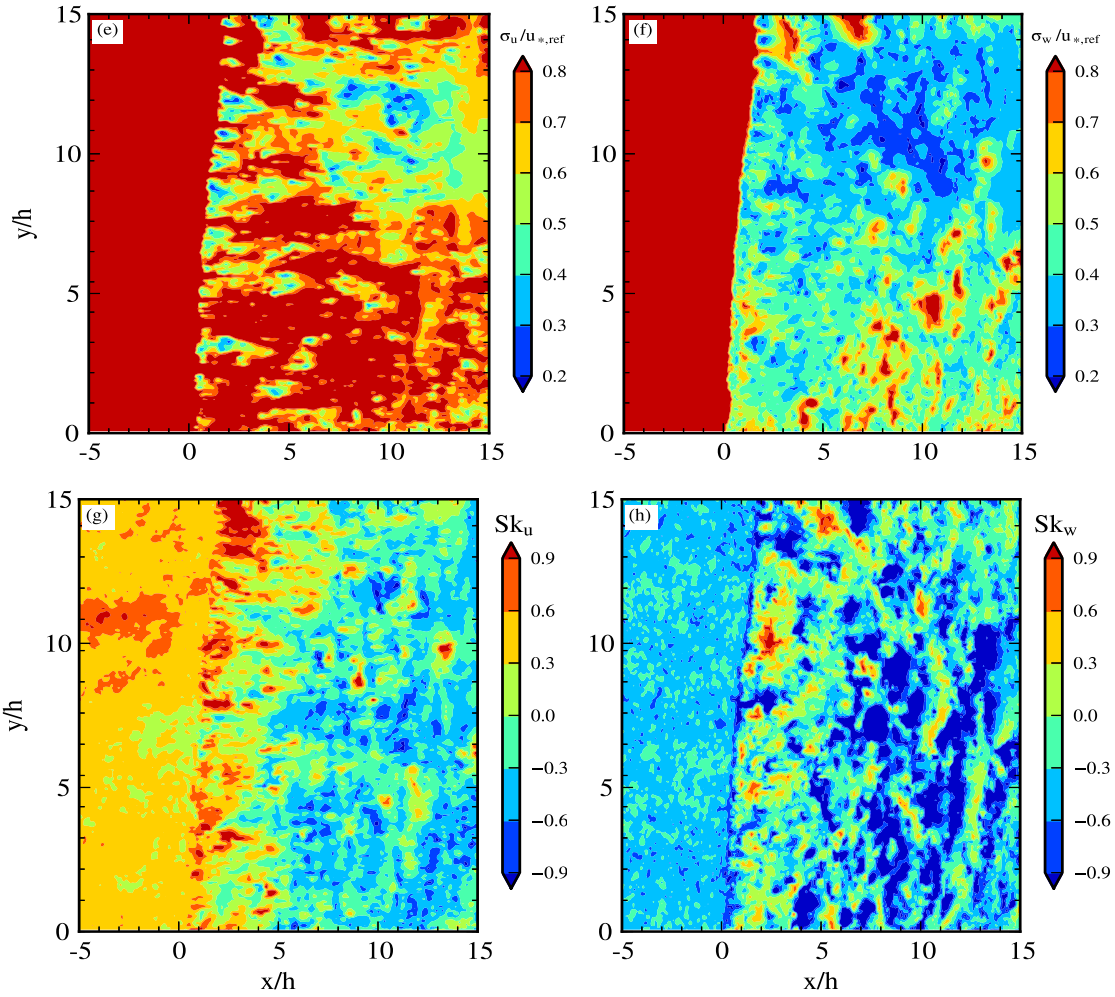

Figure 5.7: (*continued*) (e) standard deviation of u, (f) standard deviation of w, (g) skewness of u, and (h) skewness of w. All variables are normalized with the reference streamwise wind velocity, u_{ref}, and the friction velocity, $u_{*,ref}$, located 30.9 m height on mast M1.

In the edge region, from about $x = 0$ to $6h$, longitudinal high wind speed patterns extending up to $6h$ are visible (Fig. 5.7c). They correspond to the flow penetration through the sparsest regions of the forest edge. These patterns are associated with high values of σ_u (Fig. 5.7e), $\overline{u'w'}$ (Fig. 5.7b) and Sk_u (Fig. 5.7g). Further downstream ($x > 6h$), the edge effect is less visible and the variabilities of turbulent fields are more correlated to forest gaps or low canopy density regions from which turbulent structures penetrate easier, or where the flow accelerates. Compared to u-statistics, w-statistics do not show much differences between the edge region and further downstream, except the negative values of w near the edge due to the flow skirting around the tree crowns (Fig. 5.7d). Statistics from w

exhibit more a local effect in relation to the canopy structures. In particular, small clearings correlate with high values of σ_w (Fig. 5.7f). Sk_u and Sk_w (Fig. 5.7g and Fig. 5.7h) depend as well on the local structure of the canopy, changing abruptly from positive to negative values in the $x-y$ plane. Negative values of Sk_w are often associated with gaps in the canopy.

5.3.5 Spatial standard deviations of flow statistics

To quantify the spatial variability of the flow due to the forest heterogeneities, Fig. 5.8 shows the lateral spatial standard deviations of flow statistics obtained from the heterogeneous-edge case subtracted with the deviations obtained from the homogeneous-edge case. This latter subtraction aims at removing spatial variabilities related to large-scale turbulent structures present in both cases due to the limited size of the computational domain or due to the clearing-forest pattern. The dispersive fluxes are excluded from this analysis and their contributions are quantified in Section 5.3.6. The lateral standard deviations are corresponding to the y-region used for spatially averaged wind statistics in Fig. 5.5 and 5.6. Hence, Fig. 5.8 includes the spatial standard deviations of (1) $\overline{u}$ and $\overline{w}$ ($\sigma_{\overline{u}}$ and $\sigma_{\overline{w}}$) normalized by $\langle\overline{u}\rangle_y$ at the same height, (2) σ_u and σ_w (σ_{σ_u} and σ_{σ_w}) normalized by $\langle\sigma_u\rangle_y$ and $\langle\sigma_w\rangle_y$, respectively, and (3) Sk_u and Sk_w (σ_{Sk_u} and σ_{Sk_w}), along the edge region, at $z=h/2$ and $1.25h$. Note that σ_{Sk_u} and σ_{Sk_w} are not normalized as the other standard deviations due to near-zero values of skewnesses in some regions of the canopy. Standard deviation values in the leading edge region, between $x=0-1h$, needs to be taken with caution as they also reflect the slight y-curvature of the heterogeneous forest edge (Fig. 5.7a).

Flow variabilities induced by forest heterogeneities occur mostly within the canopy and less above. As seen on Fig. 5.8a, the variability of $\overline{u}$ ($\overline{w}$) represents about 20% (5%) of the spatial mean at mid-canopy height. It occurs mostly in the edge region for $\overline{u}$ ($x<8h$) due to the difference of edge-flow penetration between the sparsest and densest regions of the forest edge, as observed in Fig. 5.7c. Second- and third-order moments of w exhibit larger variabilities than corresponding u-moments. The variability of σ_w (σ_u) represents about 30% (15%) of the spatial mean within the canopy, and that of Sk_w (Sk_u) about 0.4 (0.1). They do not show any distinct trend with the distance from the edge, as standard deviations of PAI and h remain relatively homogeneous along the edge (Fig. 5.2d). These levels of flow spatial variability are associated to 60% and 20% spatial standard deviations of PAI and canopy height, respectively.

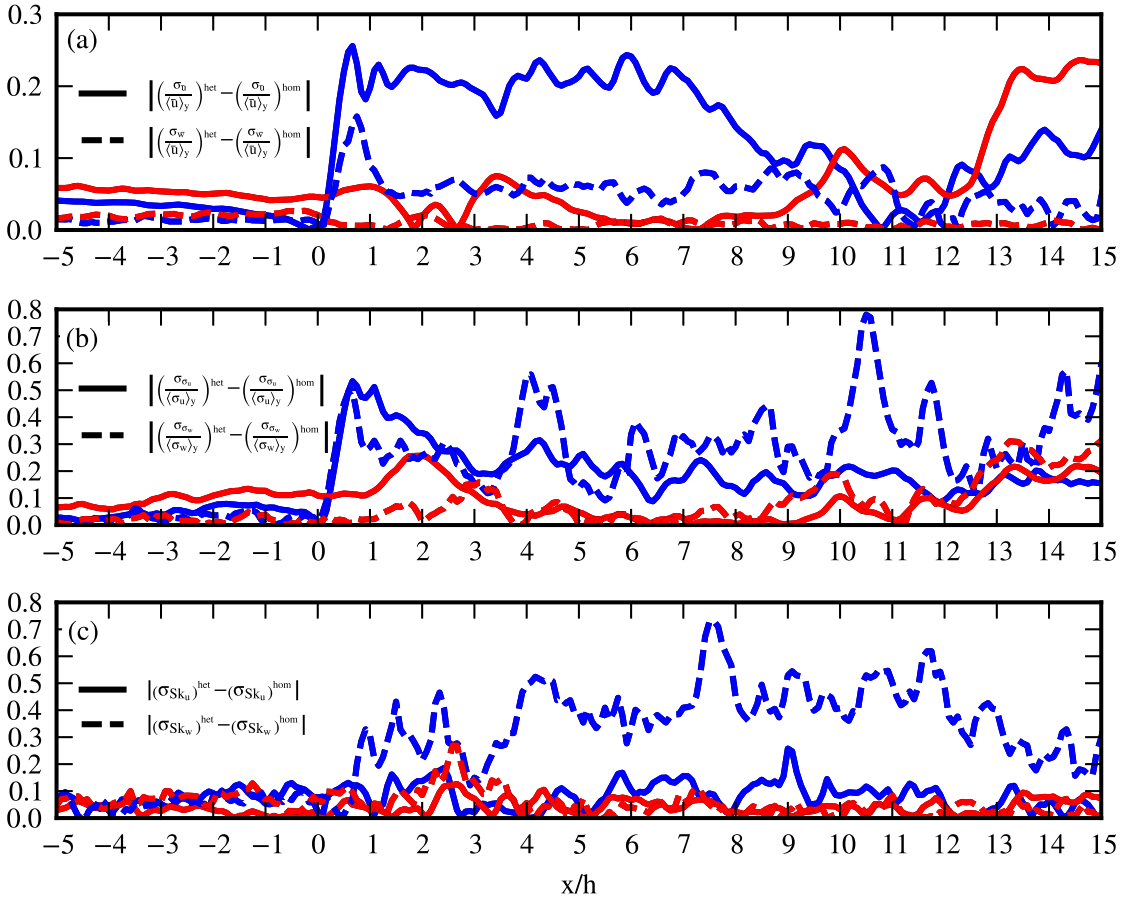

Figure 5.8: Spatial standard deviations along the edge at $z = h/2$ (blue lines) and $z = 1.25h$ (red lines) of (a) $\overline{u}$ and $\overline{w}$ normalized by time- and y-averaged u at the same height, (b) σ_u and σ_w normalized by the time- and y-averaged σ_u and σ_w at the same height, respectively, and (c) Sk_u and Sk_w, for the heterogeneous-edge case minus the corresponding spatial standard deviations obtained from the homogeneous-edge case.

5.3.6 Dispersive fluxes

Dispersive fluxes for different sizes of the averaging region R along $z = 0.75h$ are shown in Fig. 5.9 for the heterogeneous-edge for: the variance of the streamwise velocity component ($\langle \bar{u}'' \bar{u}'' \rangle_y$), the variance of the vertical velocity component ($\langle \bar{w}'' \bar{w}'' \rangle_y$) and the momentum flux ($\langle \bar{u}'' \bar{w}'' \rangle_y$). The variables are normalized with an upwind reference friction velocity $\langle u_{*,ref} \rangle_y$ defined at 30.9 m height at mast M1. Fig. 5.10 shows the same variables, but in the entire $x - z$ plane for the averaging region R defined in Section 5.2.4 ($A = x \times y = h \times 5h$). The dispersive fluxes are first calculated with regards to the averaging region R before being y-averaged. We are interested to quantify if tree-scale heterogeneities are inducing important dispersive fluxes at the scale of the edge (or up to the scale of R). This can indicate if homogeneity is an acceptable assumption in edge flow. Note that the dispersive fluxes below the LES grid size are ignored whereas dispersive fluxes above this scale remain.

The choice of the horizontal-averaging area should be as large as possible to include a representative sample of the variability present in the time-averaged flow. Choosing a too small averaging area can underestimate the edge-scale dispersive fluxes, especially near the leading edge where the flow variability is important (see Fig. 5.7). This is shown by the increasing u-variance with increasing y-averaging between $x = 0$ to $4h$ (Fig. 5.9a). However, choosing a too large y-averaging can include unwanted variabilities related to the y-curvature of the edge, and to the large-scale turbulent structures which are present in the domain due to its limited size or to the clearing-forest pattern. The former effect can be related to notable differences in (y) spatial-variability between free-air (where no density is found due to the curved edge) and where the spatial-variability inside the canopy is integrated. The latter effect is related the large turbulent structures in the domain which are inducing important stationnary high and low regions of wind velocity in the time-averaged flow (and therefore dispersive fluxes). This is clearly observable upstream the edge for $A = 1h \times 10h$ in the dispersive u-variance. As we seek to quantify the dispersive fluxes induced by the canopy only, an area of $A = x \times y = h \times 5h$ is therefore chosen to calculate the dispersive fluxes.

Important dispersive flux variances are found above the leading edge, in the lower trunk space of the entry region and downwind around canopy top (Fig. 5.10a and 5.10b). The dispersive flux variances vanish in the streamwise direction (Fig. 5.10a and 5.10b) whereas the dispersive momentum flux remain everywhere inside the canopy (Fig. 5.10c). Ratios of the dispersive fluxes with the single-point fluxes ($\langle \bar{u}_i'' \bar{u}_i'' \rangle_y / \langle \overline{u_i' u_i'} \rangle_y$) indicated that the dispersive u-variance can be as high as 10 to 50% of the single-point u-variance at the leading edge, 20% downwind just below the tree crown layer (not shown). The dispersive w-variance is as high as 10 to 30% of the single-point w-variance at the leading edge. Both single-point

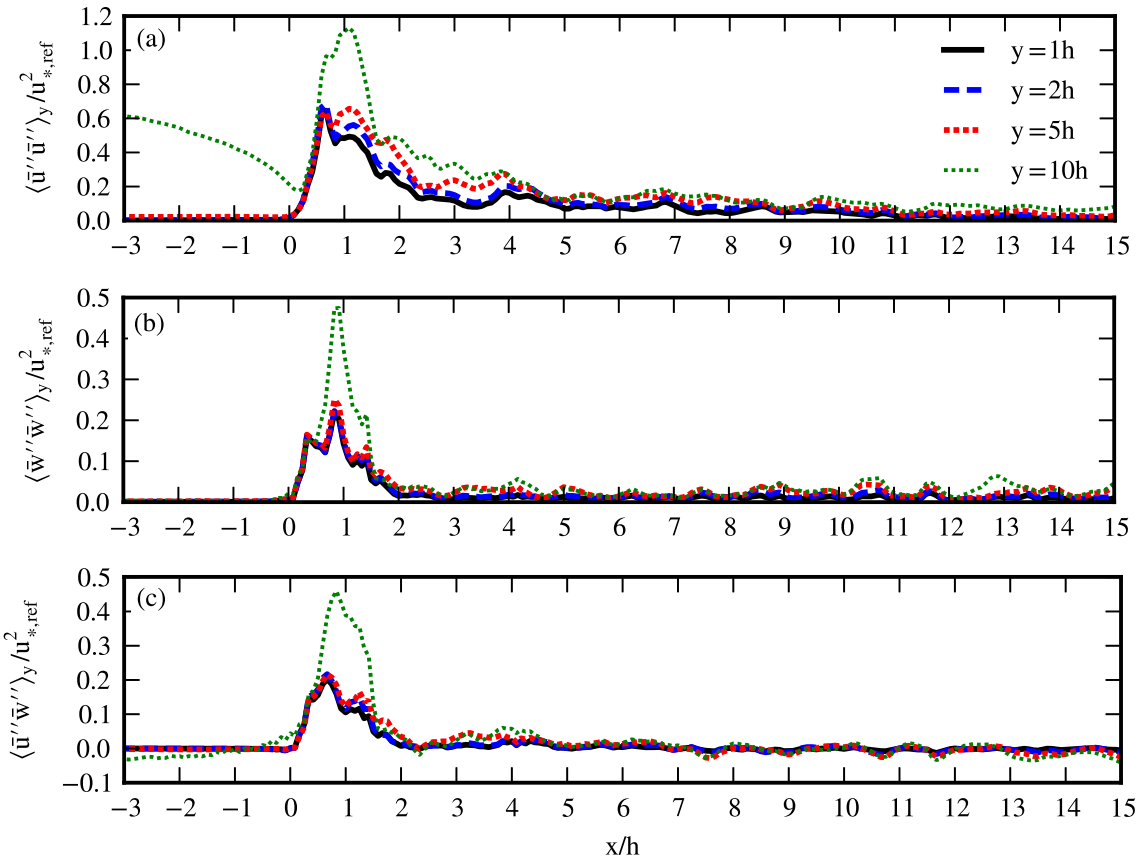

Figure 5.9: Dispersive fluxes calculated for the heterogeneous-edge case along $z = 0.75h$, y-averaged, for different sizes of the averaging region R for: (a) the variance of the streamwise velocity component, (b) the variance of the vertical velocity component, and (c) the momentum flux. The regions are shown for $A = h \times h$ (black solid line), $A = h \times 2h$ (blue dashed-line), $A = h \times 5h$ (red squared-line) and $A = h \times 10h$ (green dotted-line). All variables are normalized with the reference friction velocity, $\langle u_{*,ref} \rangle_y$, located 30.9 m height on mast M1.

and dispersive momentum flux (Fig. 5.5d and 5.10c, respectively) are found low inside the canopy, except at the leading edge where they are found comparable in magnitude. These results reach the observations of Poggi et al. (2004) and Bailey and Stoll (2013), who also found non-negligible dispersive fluxes for their study.

5.4 Discussion and conclusion

The wind flow over an heterogeneous forest edge on the Falster island in Denmark was investigated using large-eddy simulation. The forest exhibits spatial standard deviations of PAI and canopy height of about 60% and 20%, respectively.

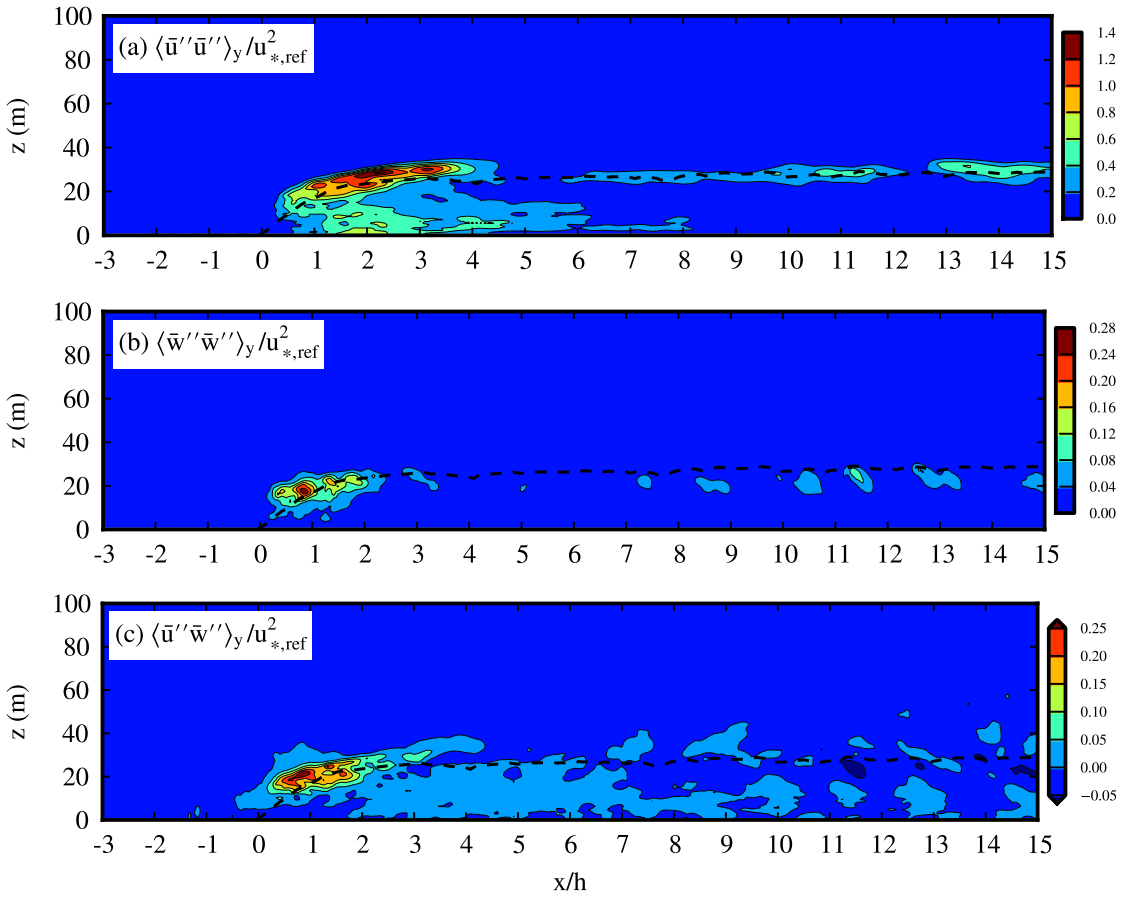

Figure 5.10: Edge-scale dispersive fluxes, y-averaged, as calculated for the heterogeneous-edge case for: (a) the variance of the streamwise velocity component, (b) the variance of the vertical velocity component, and (c) the momentum flux. All variables are normalized with the reference friction velocity, $\langle u_{*,ref} \rangle_y$, located 30.9 m height on mast M1. The black dashed-line indicate the y-averaged tree height.

Compared to previous LES edge flow studies, this represents the first attempt to simulate edge flow in a forest where three-dimensional heterogeneities down to the tree-scale are explicitly accounted for. The edge flow was first evaluated against wind measurements upwind and downwind of the forest leading edge. The impact of the canopy heterogeneity on the edge flow was thereafter investigated.

Different features are identified in the mean two-dimensional edge flow compared to an equivalent horizontally homogeneous forest. The main differences are mostly related to a further flow penetration within the heterogeneous forest from the edge. This emphasizes the importance of representing well the edge shape, density and vertical foliage distribution, that controls the flow tilt angle and flow penetration within the canopy. Remaining differences that cannot be explained by

these effects are related to a slower adjustment of the correlation coefficient r_{uw} and the absence of a defined enhanced gust zone at canopy top when the canopy was heterogeneous.

The horizontal heterogeneities of the forest induce significant spatial variabilities of flow statistics. In particular, statistics of the streamwise wind velocity (u) correlate with edge heterogeneities due to flow penetration in the sparsest regions of the forest, creating a succession of high and low velocity regions that could affect the lateral transport mechanism through dispersive fluxes and $x-y$ shear production mechanisms. Near the leading edge, the spatial standard deviation of u reaches about 20%. Further downstream, only the statistics of the vertical wind velocity (w) show a high correlation with heterogeneities. The vertical velocity is more representative of a local effect. The largest spatial variability of the standard deviations of velocity components (30% and 15% for w and u, respectively) and skewnesses (0.4 and 0.1 for Sk_w and Sk_u, respectively) in the heterogeneous-edge case compared to the homogeneous one, could indicate an easier penetration of turbulent structures within the heterogeneous forest. However, the efficiency of turbulence to transport momentum (r_{uw}) is comparable downwind of the edge in the heterogeneous- and homogeneous-edge cases, without enhancing significantly the total momentum exchange ($\overline{u'w'}$) at forest scale. Similarly as in row canopies (Bailey and Stoll, 2013; Chahine et al., 2014), we suspect that in presence of tree-scale heterogeneities, turbulent structures are more likely forming at some specific locations.

In our edge flow analysis, non-negligible edge-scale dispersive fluxes are found. They can represent as high as 10 to 50% of the single-point variances and are even be comparable to the momentum flux at the leading edge. These results corroborate with previous studies in organized canopies (Poggi et al., 2004; Bailey and Stoll, 2013) and strongly contradict the assumption that they can be considered negligible.

The spatial variability due to forest heterogeneities may have some consequences in numerical modeling using simplified turbulence models, coarse grids or homogeneous canopy descriptions. In the edge region, a poor description of the edge shape and ignoring the canopy heterogeneity could respectively lead to poor modeling accuracy and bias. In the far-edge region, a bias related to dispersive fluxes could remain near canopy top. Consequently, considering the canopy heterogeneity and a careful description of the edge is recommended to avoid any sorts of modeling error due to the spatial variability of the forest.

Acknowledgements

The authors acknowledge the financial support of the Center for Computational Wind Turbine Aerodynamics and Atmospheric Turbulence sponsored by the Dan-

ish Council for Strategic Research, grant number 09-067216, and Vattenfall. We would also like to thank the Center for Analysis and Prediction of Storms (CAPS) at the University of Oklahoma for providing the ARPS code. Computer simulations related to this work were performed using the Avakas cluster from MésoCentre MCIA as well as the ISPA cluster. Thanks are expressed to Dr Mark R. Irvine for his help with the cluster set-up and administration.

6

SUMMARY AND OUTLOOK

In wind energy, forested sites are of interest for wind turbine siting, but they are often associated with high levels of wind shear and turbulence intensity, which increase the loads on wind turbines. Computational fluid dynamics (CFD) is a useful tool to quantify the wind characteristics, but the interaction between the forest and the atmosphere is challenging to simulate with a high degree of accuracy.

The motivation of the thesis was to improve the numerical predictions for flows over and inside forests for wind (energy) assesments. A great part of the prediction uncertainty is currently related to canopy heterogeneities. Heterogeneities are due to the fragmented nature of the landscape, often shaped by man-made activities, or simply due to the random variability of the forest properties. Forest heterogeneities can alter the momentum transfer significantly in the boundary layer and the prediction accuracy of wind models may therefore rely on their proper description. A first objective was to improve the representation of the canopy structure in wind models and a second objective, to use the new forest description to study the flow over and inside tree- to stand-scale heterogeneities.

To account for the canopy structure, the drag parameterization using a three-dimensional representation of the forest using the frontal area density as input was well suited. This approach required the specification of the density of the forest in all points of the three-dimensional computational domain. For such small-scale canopy structure description, the acquisition of the density over large domains would be challenging using traditional inventory methods. Aircraft-based light detection and ranging (LiDAR) scanning was identified as the most promising technology to meet these requirements. The reflection points of aerial LiDAR scans (ALS), however, do not directly provide the information about the forest density. The scans must be priorly transformed into a format suitable for numerical wind models. The development of such a LiDAR method for vegetation density description and its validation constituted a major part of the thesis.

To improve wind predictions over and inside heterogeneities, a first question that arose was whether a detailed description was important for accuracy, and if the wind field over large areas could be affected significantly. For this objective, a forest grid was generated using the LiDAR method defined for a 5×5 km^2 forested site in Sweden and Reynolds-averaged Navier-Stokes (RANS) simulations were performed. Secondly, edges are a common type of heterogeneities encountered in forests. The wind flow around homogeneous forest edges has previously been

studied in the scientific literature, whereas the impacts of tree-scale heterogeneities are currently less understood. Knowing if and how the edge flow is affected by tree-scale heterogeneities could suggest potential improvements for numerical models. For this purpose, a second grid was generated from high resolution helicopter-based LiDAR scans for the Falster island edge site in Denmark and large-eddy simulations (LES) were carried.

From the objectives, three hypothesis were initially formulated (see Chapter 1) and demonstrated troughout the thesis (in Chapter 3, 4 and 5). In this section, each of the hypothesis are discussed, along with outlooks of future work possibilities.

Hypothesis 1

> *Using aerial LiDAR scans of forested areas in combination with Beer-Lambert's law, a high-accuracy forest description can be achieved for large computational domains.*

Conlusion A method to calculate highly variable and realistic frontal area density input was achieved by using raw data from aerial LiDAR scans, together with the Beer-Lambert law. From the calibration and validation of the method with ground-based measurement of plant area index and tree height, it was shown that highly variable and realistic frontal area density input can be gridded. A grid was generated from the method and prescribed at the lower boundary of RANS simulations of a 5×5 km^2 forested site. When compared to wind measurements from a mast, the simulations showed a good correlation for the mean wind speed of two wind directions with different influences from the upstream forest. The method is therefore a promising way forward for achieving higher accuracy in wind modeling.

Outlook For the turbulent kinetic energy, the CFD model indicated that further developments may be needed to improve the predictions. A forested hill located upwind of a specific wind direction produced a too high level of turbulence compared to the observations. Turbulence modeling developments at real sites could benefit from the proposed LiDAR method. The method, which provides a detailed description of the terrain and vegetation, can be a valuable component for testing various wind models at sites with high-quality wind measurements. This could improve the predictive capability of RANS and high-resolution LES simulations. For simplified models, the mapping of the forest properties using the LiDAR method (plant area index and tree height) could be converted to reliable estimates of roughness and displacement heights (see *e.g.* Raupach, 1994), to provide lower uncertainty inputs.

The LiDAR method should be applied at other forested sites to verify if a global decrease of modeling uncertainties is gained comparatively to the use of standard methods (*e.g.* applying a high-roughness value of forest). Raw data of LiDAR scans are becoming increasingly accessible in several countries and the uncertainty reduction could be verified for many different sites. If improvements are confirmed, the LiDAR method could become a standard of practice to perform wind assessments.

Wind farms at forested sites are generally located far from residential areas, but individual buildings may be located nearby. Buildings are currently not accounted for in the proposed LiDAR method, but a detection algorithm could be developed. Sharp objects such as buildings are not easily treated in CFD, but they could be used in connection with advanced methods for treating complex geometries (*e.g.* immersed boundaries, see Mittal and Iccarino, 2005). Eventually, a mapping of CFD inputs could be produced at country-scales, which could ultimately lead to a large-scale mapping of micro-scale effects.

Hypothesis 2

> *A detailed representation of the canopy structure is important to achieve high-accuracy simulations of the wind field over large areas.*

Conclusion For a 1×1 km area, RANS simulations showed that higher wind velocities and tke were found with more complex canopy structures. The tke was more sensitively responding to the small variations of canopy structure compared to the velocity. When the site is complex, the small-scale heterogeneities are therefore important to consider as simplifying the canopy description can degrade the accuracy of the simulations near the surface. In wind energy, this can be especially important when small wind turbines located at a complex forested site are considered.

Outlook The increase in wind velocity and turbulent kinetic energy when refining the canopy structure is an interesting effect to investigate further. It is suspected that the flow inside an heterogeneous forest is more likely to conserve high wind speed and turbulence through the many gaps present in the canopy structure compared to an homogeneous one. An improved understanding of this effect could provide general guidelines to wind farm developers on the best sites to choose prior a wind turbine siting near forests.

The ALS gives temporal snapshot of the canopy structure for a specific day of the year. It is currently unknown how the mean wind field is varying with the sea-

For example, databases such as Danmarks højdemodel and Landmäteriet in Sweden are now publicly available.

sonal changes in canopy structure at sites where deciduous (leafy) trees are found. Quantification of theses differences using time-series of ALS could be performed so that the sensitivity of the CFD simulations for these particular forests could be verified. If a high sensitivity or variability is found, this could give an indication that corrections on the scans, or the use of time-series of ALS, could be necessary and/or recommended.

Hypothesis 3

Tree-scale heterogeneities do not have an important impact in edge flow.

Conclusion The spatial variability from tree-scale heterogeneities was found important in edge flow. The main difference found is a further flow penetration inside the canopy, making the density and vertical foliage distribution key properties to describe the equivalent homogeneous forest edge. Other differences are related to a slower adjustment of the correlation coefficient and the absence of a defined enhanced gust zone at canopy top. Significant spatial standard deviations of time-averaged flow statistics were found, increasing with high-order moments. Compared to single-point fluxes, the magnitude of dispersive fluxes were found high at the leading edge (10 to 50% of the single-point variances and comparable to the momentum flux).

Outlook The LES model was evaluated against field measurements. Differences related to inflow conditions were found, as was shown with the 30% turbulence intensity for the LES simulation upwind the edge compared to 20% for the measurements. This suggests that the LES model in the configuration presented may need improvements to reproduce more realistic inflow conditions. Inflow conditions are currently an area of active research in the LES community, and various approaches have been proposed (see *e.g.* Keating et al., 2004). More dedicated attention towards this topic is recommended for future LES studies at forested sites.

The turbulence intensity was found lower past the heterogeneous edge (30%) compared to the homogeneous one (35%). It is not clear if the difference is due to the missing density at the location of the y-curvature of the edge, to the fact that the total PAI between both cases are not equivalent at the edge scale, or if it is an effect related to canopy heterogeneity. This should be clarified in a future study. Nevertheless, as for the previous RANS study, it is speculated that high wind speed and turbulence is conserved trough the gaps in the canopy structure when the forest is heterogeneous. Simplified cases could be set up, for example, an infinite (periodic) forest with different types of heterogeneities. Since the configuration studied was for an edge located in front of a wide open clearing, it would

also be interesting to investigate the edge flow in many more different configurations where the clearing distance and the length of the forest are varied inside the domain. The outcomes of such studies could lead to classifications of wind potentials by forest types. This information could provide useful guidelines for preliminary studies of wind turbine siting assessments.

As regards the main conclusions of the study, the spatial variability due to forest heterogeneities may have some consequences in numerical modeling, where simplified turbulence models, coarse grids or homogeneous canopy descriptions are used. If scans are not available and a homogeneous canopy descriptions is considered, the study showed that the density and the vertical foliage distribution is important to reproduce properly, since they both control the flow tilt angle and flow penetration within the canopy. Other effects related to canopy heterogeneity can however not be captured without a detailed description of the canopy, as is the case for dispersive fluxes. This can introduce a systematic bias in simplified turbulence models, but it is currently unknown if dispersive fluxes are really changing the flow properties in homogeneous canopy and how dispersive fluxes would affect in this case the mean velocity and the turbulent kinetic energy in the flow. A detailed 1st- and 2nd-order budget is recommended to verify the role and the importance of each dispersive flux terms in these budgets. Identifying the mechanisms through which they act in the energy redistribution loop (*i.e.* the mean, turbulent, and dispersive kinetic energy of the flow), could for example help formulating more extensive turbulence closures accounting implicitely for heterogeneities. For coarse CFD simulations (> 10 m resolution), where the forest heterogeneities over stand-scales are removed, such effort has the potential to improve the simulation accuracy, especially when fragmented landscapes including forest edges are considered.

In conclusion, it was shown in the thesis that modern techniques, such as remote sensing, can bring valuable information from the actual world to the virtual world of modern computing. A closer similarity between the two can benefit the wind predictions, or can lead one step further to more insights about real world flows. These steps are key puzzle pieces to modern challenges, such as the safety of energy supply in the context of a changing climate.

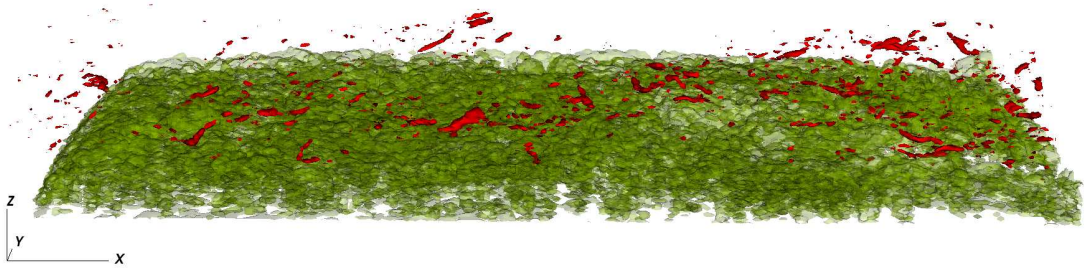

Time-snapshot of vortex structures generated numerically above a forest edge (illustrated as iso-surfaces of Q-criterion in red and the forest with the frontal area density in green).

Appendix A

EVALUATION OF METHODS FOR FOREST PROPERTIES ACQUISITION

PO.ID 361

Input parameters for CFD flow modeling of forested terrains

Louis-Étienne Boudreault[1], Ebba Dellwik[1], Eva Bøgh[2] , Andrey Sogachev[1]
[1]DTU Wind Energy, [2]Roskilde University

Summary

The purpose of this study is to present different methods for obtaining the forest characteristics required as inputs parameters in common CFD-RANS (Computational Fluid Dynamics, Reynolds-Averaged Navier-Stokes) modeling for wind energy assessment. We compare in situ measurements of forest height h and LAI (Leaf Area Index) together with terrestrial satellite measurements products acquired at different spatial resolutions, for which both spatial and time series were made available. It is shown that:

- For the forest height estimations, the SRTM and ASTER satellites include information from the forest, but far from the precision needed for the CFD modeling. The DSM based on aerial laser scans underestimate the forest height by several meters, whereas the maximum height deduced from the cloud points (raw data) were in good accordance with the forest inventory measurements (Fig. 6). Reprocessing the cloud points therefore is the most promising method for determining the forest height.

- For the LAI, the satellite-based estimates should be used with care as calibration to site specific measurements is necessary. The derived LAI values could be sensitive to a number of environmental factors (i.e. presence of clouds or biased winter reflectance) as well as to the different scaling relations involved in its derivation. A significant difference between the MODIS (LAI=3.1) and Landsat 7 (LAI=5.43, Fig. 7) satellites were obtained. The Landsat 7 showed unphysical variability in the derived LAI. However, the extraction of LAD and LAI from wind data taken within the canopy (Eq. 2, LAI=5.22) showed a good comparison with the mean value of an optical in-situ technique (LAI=5.67) and with the mean value of Landsat 7 (LAI=5.43) in the summer (Fig. 8).

Context

- In CFD-RANS modeling, the drag effect of the forest in the momentum equations is usually accounted trough a sink term as follows,

$$\frac{\partial U_i}{\partial t} = \cdots - C_d LAD(z) U_i |U|, \qquad (1)$$

where $C_d = 0.2$ is a drag coefficient and LAD(z) is the vertical plant area per unit volume.

- The height of the forest and its vertical distribution LAD(z) are thus required in order to evaluate this term.

- By applying a variety of simplification assumptions [1] to Eq. (1), the forest architecture can be related to atmospheric measurements by,

$$C_d LAD(z) = \left| \frac{\partial \overline{u'w'}}{\partial z} \right| \frac{1}{U(z)^2}. \qquad (2)$$

Example site:

- The Tromnæs beech forest edge experiment was located on the Falster island at 54°45' N, 12°2' E. From March-September 2008, a measurement campaign was conducted where both the foliated and the bare canopy period were covered. Complex flow phenomenons were observed making it a relevant test case for CFD validation.

Fig. 1: Tromnæs forest edge experiment site. White circle: approx. mast location

- Non-dimensional tree-specific profiles of LAD can be constructed from the mast measurements of the wind using Eq. (2) and the observed h:

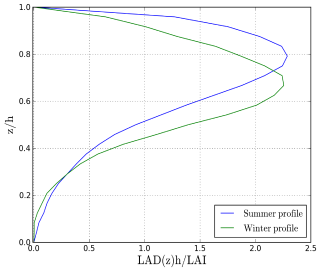

Fig. 2: Normalized beech Leaf Area Density (LAD) profiles

- The use of these profiles could be extrapolated to regions where h and LAI can be obtained from any of the techniques shown below.

Forest height (h) estimation

- Different canopy height estimates based on DSMs (Digital Surface Models), DTM (Digital Terrain Model) and forest inventory were obtained:

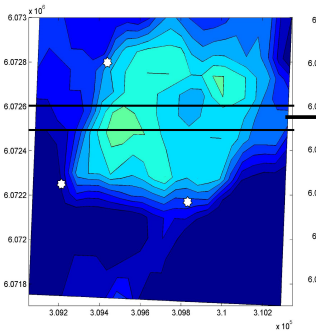

Fig. 3: Space shuttle SRTM (100 m resolution, 2000/02)

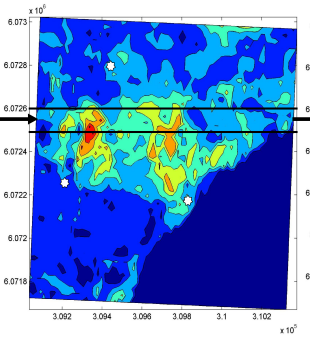

Fig. 4: Satellite ASTER [2] (15-90 m resolution)

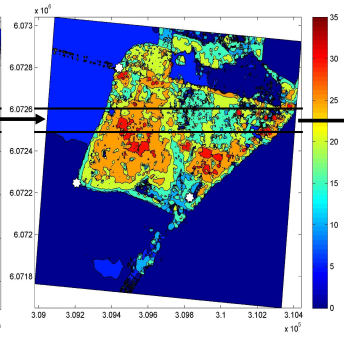

Fig.5: Aerial laser-scan (1.6m resolution, 2007/05/01)

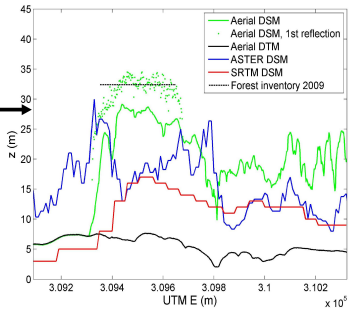

Fig.6: Forest height intercomparison (forest transect)

Leaf Area Index (LAI) estimation

- The total drag of the canopy is reflected in the LAI parameter,

$$LAI = \int_0^h LAD(z)dz. \qquad (3)$$

- The LAI can be obtained from satellite images [3, 4] using the reflectance ratio from different wavelength intervals [5] or from in-situ instruments (Fig. 8).

- For the summer, the LAI values obtained from the satellite-based MODIS instrument was 3.1 (not shown). The Landsat 7 showed unrealistic variability compared to the in-situ measurements (Fig 8), although the mean values agreed well (5.43 and 5.67 respectively) with the estimate of 5.22 (point in Fig. 8) based on Eq. (3) and the LAD summer profile presented in Fig. 2.

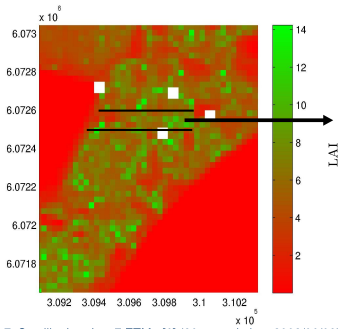

Fig.7: Satellite Landsat 7 ETM+ [6] (30m resolution, 2002/06/08)

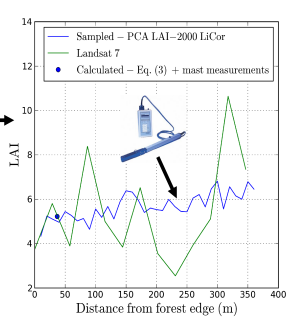

Fig.8: LAI intercomparison (forest transect)

References

1. Queck, R., Bienert, A., Maas, H.-G., Harmansa, S., Goldberg, V. and Bernhofer, C., 2012. Wind fields in heterogeneous conifer canopies: parametrisation of momentum absorption using high-resolution 3D vegetation scans. *Eur. J. Forest Res.* 131:165-176.
2. ASTER GDEM is a product of METI and NASA.
3. Carlsson, T.N. and Ripley, D.A., 1997. On the relation between NDVI, fractional vegetation cover, and leaf area index. *Remote sensing of Environment.* 62(3): 241-252.
4. Zeng, X., Dickinson, R.E., Walker, A., Shaikh, M., DeFries, R.S. and Qi, J., 2000. Derivation and Evaluation of Global 1-km Fractional Vegetation Cover Data for Land Modeling. *J. Appl. Meteor.* 39, p. 826–839.
5. Norman, J.M., Kustas, W.P. and Humes, K.S., 1995. Source approach for estimating soil and vegetation energy fluxes in observations of directional radiometric surface temperature. *Agricultural and Forest Meteorology.* 77(3-4): 263-293.
6. NASA Landsat Program, 2002, Landsat ETM+ scene L71194022_02220020608, USGS, Sioux Falls.

Bibliography

Apsley, D. and Castro, I. (1997). A limited-length-scale $k-\epsilon$ model for the neutral and stably-stratified atmospheric boundary layer. *Boundary-Layer Meteorology*, 83:75–98.

Ayotte, K. (2008). Computational modelling for wind energy assessment. *Journal of Wind Engineering and Industrial Aerodynamics*, 96:1571–1590.

Bailey, B. and Stoll, R. (2013). Turbulence in sparse, organized vegetative canopies: a large-eddy simulation study. *Boundary-Layer Meteorology*, 147:369–400.

Baldocchi, D. and Meyers, T. (1988). Turbulence structure in a deciduous forest. *Boundary-Layer Meteorology*, 43:345–364.

Bechmann, A. (2006). *Large-eddy simulation of atmospheric flow over complex terrain.* PhD thesis, Risø DTU, Roskilde, Denmark.

Bechmann, A., Berg, J., Courtney, M., Jørgensen, H., Mann, J., and Sørensen, N. (2009). The Bolund Experiment: Overview and Background. Technical Report Technical report Risø-R-1658(EN), Risø DTU - National Laboratory for sustainable energy.

Belcher, S., Harman, I., and Finnigan, J. (2012). The wind in the willows: flows in forest canopies in complex terrain. *Annual Review of Fluid Mechanics*, 44:479–504.

Blackadar, A. (1962). The vertical distribution of wind and turbulent exchange in a neutral atmosphere. *Journal of Geophysical Research*, 67:3095–3102.

Bohrer, G., Katul, G., Walko, R., and Avissar, R. (2009). Exploring the effects of microscale structural heterogeneity of forest canopies using large-eddy simulation. *Boundary-Layer Meteorology*, 132:351–382.

Borak, J. (2009). Effective interpolation of incomplete satellite-derived leaf-area index time series for the continental United States. *Agricultural and Forest Meteorology*, 149:320–332.

Boudreault, L.-E., Bechmann, A., Sørensen, N., Sogachev, A., and Dellwik, E. (2014a). Canopy structure effects on the wind at a complex forested site. In *Journal of Physics: Conference Series*, volume 524 012112. IOP Publishing.

Boudreault, L.-E., Bechmann, A., Tarvainen, L., Klemedtsson, L., Shendryk, I., and Dellwik, E. (2014b). A LiDAR method of canopy structure retrieval for wind modeling of heterogeneous forests. *Agricultural and Forest Meteorology.* Accepted.

Boudreault, L.-E., Dellwik, E., Bechmann, A., Sørensen, N., and Sogachev, A. (2012a). Numerical simulation of the air flow around a forest edge using LiDAR-derived forest heights. In *8th PhD Seminar on Wind Energy in Europe*, Zurich, Switzerland.

Boudreault, L.-E., Dellwik, E., Bechmann, A., Sørensen, N., and Sogachev, A. (2013). Plant area density extraction from aerial LiDAR scans for CFD applications over forests. In *13th EMS Annual Meeting & 11th European Conference on Applications of Meteorology (ECAM)*, Reading, UK.

Boudreault, L.-E., Dupont, S., Bechmann, A., and Dellwik, E. (2014c). Edge flow in inhomogeneous canopy. *Boundary-Layer Meteorology.* In preparation.

Boudreault, L.-E., Dupont, S., Bechmann, A., and Dellwik, E. (2014d). Wind dynamics of an heterogeneous forest edge: large-eddy simulation and in-situ experiment. In *21st Symposium on Boundary Layers and Turbulence*, Leeds, UK.

Boudreault, L.-E., Sogachev, A., Dellwik, E., and Bøgh, E. (2012b). Input parameters for CFD flow modelling of forested terrain. In *Proceedings of EWEA 2012 - European Wind Energy Conference & Exhibition. European Wind Energy Association (EWEA)*, Copenhagen, Denmark.

Bréda, N. (2003). Ground-based measurements of leaf area index: a review of methods, instruments and current controversies. *Journal of Experimental Botany*, 54:2403–2417.

Campbell, G. and Norman, J. (1998). *An introduction to environmental biophysics.* Springer-Verlag, New York.

Cava, D. and Katul, G. (2008). Spectral short-circuiting and wake production within the canopy trunk space of and alpine hardwood forest. *Boundary-Layer Meteorology*, 126:415–431.

Chahine, A., Dupont, S., Sinfort, C., and Brunet, Y. (2014). Wind-flow dynamics over a vineyard. *Boundary-Layer Meterol.*, 151:557–577.

Chen, J. and Black, T. (1992). Defining leaf area index for non-flat leaves. *Plant Cell and Environment*, 15:421–429.

Clewley, D., Lucas, R., Accad, A., Armston, J., Bowen, M., Dwer, J., Pollock, S., Bunting, P., McAlpine, C., Eyre, T., Carreiras, J., and Moghaddam, M. (2012). An approach to mapping forest growth stages in Queensland, Australia through integration of ALOS PALSAR and Landsat sensor data. *Remote Sensing*, 4:2236–2255.

Coen, J. (2005). Simulation of the Big Elk Fire using coupled atmosphere-fire modeling. *International Journal of Wildland Fire*, 14:49–59.

Coops, N., Hilker, T., Wulder, M., St-Onge, B., Newham, G., Siggins, A., and Trofymow, J. (2007). Estimating canopy structure of Douglas-fir forest stands from discrete-return LiDAR. *Trees*, 21:295–310.

Deardorff, J. W. (1980). Stratocumulus-capped mixed layers derived from a 3-dimensional model. *Boundary-Layer Meteorology*, 18(4):495–527.

Dellwik, E., Bingöl, F., and Mann, J. (2014). Flow distortion at a dense forest edge. *Quaterly Journal of the Royal Meteorological Society*, 140:676–686.

Dellwik, E. and Jensen, N. (2000). Internal equilibrium layer growth over forest. *Theoretical and Applied Climatology*, 66:173–184.

Dellwik, E. and Jensen, N. (2005). Flux-profile relationships over a fetch limited beech forest. *Boundary-Layer Meteorology*, 115:179–204.

Dupont, S. and Brunet, Y. (2006). Simulation of turbulent flow in an urban forested park damaged by a windstorm. *Boundary-Layer Meteorology*, 120:133–161.

Dupont, S. and Brunet, Y. (2008a). Edge flow and canopy structure: a large-eddy simulation study. *Boundary-Layer Meteorology*, 126:51–71.

Dupont, S. and Brunet, Y. (2008b). Influence of foliar density profile on canopy flow: A large-eddy simulation study. *Agricultural and Forest Meteorology*, 148:976–990.

Dupont, S. and Brunet, Y. (2009). Coherent structures in canopy edge flow: a large-eddy simulation study. *Journal of Fluid Mechanics*, 630:93–128.

Dupont, S., Brunet, Y., and Finnigan, J. J. (2008). Large-eddy simulation of turbulent flow over a forested hill: validation and coherent structure identification. *Quaterly Journal of the Royal Meteorological Society*, 134:1911–1929.

Dupont, S., Gosselin, F., Py, C., de Langre, E., Hemon, P., and Brunet, Y. (2010). Modelling waving crops using large-eddy simulation: comparison with experiments and a linear stability analysis. *Journal of Fluid Mechanics*, 652:5–44.

Dupont, S., J.-M., B., Irvine, M., Lamaud, E., and Brunet, Y. (2011). Long-distance edge effects in a pine forest with a deep and sparse trunk space: in situ and numerical experiments. *Agricultural and Forest Meteorology*, 151:328–344.

El-Sheimy, N., Valeo, C., and Habib, A. (2005). *Digital terrain modeling*. Artec House, Norwood.

Evans, J. and Hudak, T. (2007). A multiscale curvature algorithm for classifying discrete return lidar in forested environments. *IEEE Transactions on Geoscience and Remote Sensing*, 45(4):1029–1038.

EWEA (2013). Wind in Power: 2013 European Statistics. Technical report, European Wind Energy Association (EWEA), Brussels, Belgium.

FAO (2010). Global Forest Resources Assessment 2010 – main report. Technical report, Food and Agriculture Organization of the United Nations (FAO), Rome, Italy.

Finnigan, J. (2000). Turbulence in plant canopies. *Annual Review of Fluid Mechanics*, 32:519–571.

Finnigan, J. J. (1985). Turbulent transport in flexible plant canopies. In *The Forest-Atmosphere Interaction*, pages 443–480. BA Hutchison, Dordrecht, The Netherlands: Reidel.

Harman, I. and Finnigan, J. (2007). A simple unified theory for flow in the canopy and roughness sublayer. *Boundary-Layer Meteorology*, 123:339–363.

Hicks, B., Hyson, P., and Moore, C. (1975). A study of eddy fluxes over a forest. *Journal of Applied Meteorology*, 15:58–66.

Irvine, M., Gardiner, B., and Hill, M. (1997). The evolution of turbulence across a forest edge. *Boundary-Layer Meteorology*, 84:467–496.

Jonckheere, I., Fleck, S., Nackaerts, K., Muys, B., Coppin, P., Weiss, M., and Baret, F. (2004). Review of methods for in situ leaf area index determination Part I. Theories, sensors and hemispherical photography. *Agricultural and Forest Meteorology*, 121:19–35.

Jones, W. and Launder, B. (1972). The prediction of laminarization with a two-equation model of turbulence. *International Journal of Heat and Mass Transfer*, 15:301 – 314.

Kaimal, J. C. and Finnigan, J. J. (1998). *Atmospheric boundary layer flows : their structure and measurement*. Oxford University Press, New York.

Kantha, L. (2004). The length scale equation in turbulence models. *Nonlinear Process Geophys*, 11:83–97.

Katul, G., Mahrt, L., Poggi, D., and Sanz, C. (2004). One- and two-equation models for canopy turbulence. *Boundary-Layer Meteorology*, 113:81–109.

Katul, G. and Poggi, D. (2010). The influence of hilly terrain on aerosol-sized particle deposition into forested canopies. *Boundary-Layer Meteorology*, 137:67–88.

Keating, A., Piomelli, U., Balaras, E., and Kaltenbach, H.-J. (2004). A priori and a posteriori tests of inflow conditions for large-eddy simulation. *Physics of fluids*, 16:4696–4712.

Klemp, J. and Lilly, D. (1978). Numerical simulation of hydrostatic moutain waves. *Journal of the Atmospheric Sciences*, 35:78–107.

le Maire, G., Mardsen, C., Nouvellon, Y., Stape, J.-L., and Ponzoni, F. (2012). Calibration of a species-specific spectral vegetation index for leaf area index (LAI) monitoring: example with MODIS reflectance time-series on Eucalyptus plantations. *Remote Sensing*, 4:3766–3780.

Leblanc, S. and Chen, J. (2001). A practical scheme for correcting multiple scattering effects on optical LAI measurements. *Agricultural and Forest Meteorology*, 110:125–139.

Lee, X. (2000). Air motion within and above forest vegetation in non-ideal conditions. *Forest Ecology and Management*, 135:3–18.

Lefsky, M., Harding, D., Cohen, W., Parker, G., and Shugart, H. (1999). Surface lidar remote sensing of basal area and biomass in deciduous forests of eastern Maryland, USA. *Remote Sensing of Environment*, 67:83–98.

Leonard, A. (1974). Energy cascade in large simulation of turbulent fluid flow. *Advances in Geophysics*, 18A:237–248.

Leonard, B. (1979). A stable and accurate convective modelling procedure based on quadratic upstream interpolation. *Computational methods in applied mechanical engineering*, 19:59–98.

Lieffers, V., Stadt, K., and Navratil, S. (1996). Age structure and growth of understory white spruce under aspen. *Canadian Journal of Forest Research*, 26:1002–1007.

Lien, F.-S., Yee, E., and Wilson, J. (2005). Numericall modelling of the turbulent flow developing within and over a 3-D building array, Part II: A mathematical foundation for a distributed drag force approach. *Boundary-Layer Meteorology*, 114:245–285.

Lindroth, A. (1993). Aerodynamic and canopy resistance of short-rotation forest in relation to leaf area index and climate. *Boundary-Layer Meteorology*, 66:265–279.

Lopes Da Costa, J., Castro, F., Palma, J., and Stuart, P. (2006). Computer simulation of atmospheric flows over real forests for wind energy resource evaluation. *Journal of Wind Engineering and Industrial Aerodynamics*, 94:603–620.

Mann, J. and Dellwik, E. (2014). Sudden distortion of turbulence at a forest edge. In *Journal of Physics: Conference Series*, volume 524 01210. IOP Publishing.

Mcinerney, D., Suarez-Minguez, J., Valbuena, R., and Nieuwenhuis, M. (2010). Forest canopy height retrieval using LiDAR data, medium-resolution satellite imagery and kNN estimation in Aberfoyle, Scotland. *Forestry*, 83:195–206.

Michelsen, J. (1992). Basis3d - a platform for development of multiblock PDE solvers. Technical Report Technical report AFM 92-05, Technical University of Denmark.

Michelsen, J. (1994). Block structured multigrid solution of 2D and 3D elliptic PDE's. Technical Report Technical report AFM 94-06, Technical University of Denmark.

Mittal, R. and Iccarino, G. (2005). Immersed boundary methods. *Annual Review of Fluid Mechanics*, 37:239–261.

Moeng, C. H. (1984). A large-eddy-simulation model for the study of planetary boundary-layer turbulence. *Journal of the Atmospheric Sciences*, 41(13):2052–2062.

Monsi, M. and Saeki, T. (2005). On the factor light in plant communities and its importance for matter production. *Annals of Botany*, 95:549–567.

Morsdorf, F., Kötz, B., Meier, E., Itten, K., and Allgöwer, B. (2006). Estimation of LAI and fractionnal cover from small footprint airborne laser scanning data based on gap fraction. *Remote sensing of Environment*, 104:50–61.

Morse, A., Gardiner, B., and Marshall, B. (2002). Mechanisms controlling turbulence development across a forest edge. *Boundary-Layer Meteorology*, 103:227–251.

Nichiporovich, A. (1962). Properties plant of crops as an optical system. *Soviet Plant Physiology*, 8:428–435.

Orlanski, I. (1975). A rational subdivision of scales for atmospheric processes. *Bulletin of the American Meteorological Society*, 56:527–530.

Panferov, O. and Sogachev, A. (2008). Influence of gap size on wind damage variables in a forest. *Agricultural and Forest Meteorology*, 148:1869–1881.

Patankar, S. (1980). *Numerical heat transfer and fluid flow*. McGraw Hill Book Company, New York.

Peduzzi, A., Wynne, R., Thomas, V., Nelson, R., Reis, J., and Sanford, M. (2012). Combined use of airborne lidar and DBInSAR data to estimate LAI in temperate mixed forests. *Remote Sensing*, 4:1758–1780.

Pimont, F., Dupuy, J.-L., Linn, R., and Dupont, S. (2011). Impacts of tree canopy structure on wind flows and fire propagation simulated with firetec . *Annals of Forest Science*, 68:523–530.

Pinard, J.-P. and Wilson, J. (2001). First- and second-order closure models for wind in a plant canopy. *Journal of Applied Meteorology*, 40:1762–1768.

Poggi, D., Katul, G., and Albertson, J. (2004). A note on the contribution of dispersive fluxes to momentum transfer within canopies. *Boundary-Layer Meteorology*, 111:615–621.

Popescu, S. and Wynne, R. (2004). Seeing the trees in the forest: using lidar and multispectral data fusion with local filtering and variable window size for estimating tree height. *Photogrammetric Engineering And Remote Sensing*, 70:589–604.

Queck, R., Bienert, A., Maas, H.-G., Harmansa, S., Goldberg, V., and Bernhofer, C. (2012). Wind fields in heterogeneous conifer canopies: parametrisation of momentum absoption using high-resolution 3D vegetation scans. *European Journal of Forest Research*, 131:165–176.

Raupach, M. (1994). Simplified expressions for vegetation roughness length and zero-plane displacement as functions of canopy height and area index. *Boundary-Layer Meteorology*, 71:211–216.

Raupach, M. (1995). Corrigenda. *Boundary-Layer Meteorology*, 76:303–304.

Raupach, M., Bradley, E., and Ghadiri, H. (1987). A wind tunnel investigation into aerodynamic effect of forest clearings on the nesting of abbott's Boody on Christmas Island. Technical report, CSIRO Centre for environmental Mechanics, Canberra, Australia.

Raupach, M., Coppin, P., and Legg, B. (1996a). Experiments on scalr dispersion within a model plant canopy. Part I: The turbulence structure. *Boundary-Layer Meteorology*, 35:21–52.

Raupach, M., Finnigan, J., and Brunet, Y. (1996b). Coherent eddies and turbulence in vegetation canopies: the mixing-layer analogy. *Boundary-Layer Meteorology*, 78:351–382.

Raupach, M. and Shaw, R. (1982). Averaging procedures for flow within vegetation canopies. *Boundary-Layer Meteorology*, 22:79–90.

Rhétoré, P.-E. (2009). *Wind turbine wake in atmospheric turbulence.* PhD thesis, Alborg University, Aalborg, Denmark.

Rhie, C. (1981). *A numerical study of the flow past an isolated airfoil with separation.* PhD thesis, University of Illinois.

Richardson, J., Moskal, L., and Kim, S.-H. (2009). Modeling approaches to estimate effective leaf area index from aerial discrete-return LIDAR. *Agricultural and Forest Meteorology*, 149:1152–1160.

Ross, J. (1981). *The radiation regime and architecture of plant stands.* Springer Netherlands, Dordrecht.

Sanz, C. (2003). A note on k-epsilon modelling of vegetation canopy air-flows. *Boundary-Layer Meteorology*, 108:191–197.

Schlegel, J. (2012). Large-eddy simulation of inhomogeneous canopy flows using high-resolution terrestrial laser scanning data. *Boundary-Layer Meteorology*, 142:223–243.

Shaw, R. and Schumann, U. (1992). Large-eddy simulation of turbulent flow above and within a forest. *Boundary-Layer Meteorology*, 61:41–64.

Shendryk, I., Hellström, M., Klemedtsson, L., and Kljun, N. (2014). Low-density LiDAR and optical imagery for biomass estimation over boreal forest in Sweden. *Forests*, 5:992–1010.

Sogachev, A. (2009). A note on two-equation closure modelling of canopy flow. *Boundary-Layer Meteorology*, 130:423–435.

Sogachev, A. and Panferov, O. (2006). Modification of two-equation models to account for plant drag. *Boundary-Layer Meteorology*, 121:229–266.

Solberg, S., Brunner, A., Hanssen, K., Lange, H., Naesset, E., Rautiainen, M., and Stenberg, P. (2009). Mapping LAI in a Norway spruce forest using airborne laser scanning. *Remote Sensing of Environment*, 113:2317–2327.

Solberg, S., Naesset, E., Hanssen, K., and Christiansen, E. (2006). Mapping defoliation during a severe insect attack on Scots pine using airborne laser scanning. *Remote Sensing of Environment*, 102:364–376.

Sørensen, N. (1995). General purpose flow solver applied to flow over hills. Technical Report Risø-R-827(EN), Ph.D. thesis., Risø DTU.

Sørensen, N. (1998). Hygrid2D - a 2D mesh generator. Technical Report Technical report Risø-R-827(EN), Risø DTU.

Sørensen, N., Bechmann, A., Boudreault, L.-E., Koblitz, T., and Sogachev, A. (2013). CFD applications in wind energy using RANS. In *CFD for atmospheric flows and wind engineering.* von Karman Institute for Fluid Dynamics, Rhode-St-Genèse.

Sun, R., Krueger, S., Jenkins, M., Zulauf, M., and Charney, J. (2009). The importance of fire-atmosphere coupling and boundary-layer turbulence to wildfire spread. *International Journal of Wildland Fire*, 18:50–60.

Thom, A. (1968). The exchange of momentum, mass and heat between an artificial leaf and airflow in a wind tunnel. *Quaterly journal of the royal meteorological society*, 94:44–55.

Thom, A. (1971). Momentum absorption by vegetation. *Quaterly journal of the royal meteorological society*, 97:414–428.

TPWind (2014). Strategic Research Agenda / Market Deployment Strategy (SRA/MDS). Technical report, European Wind Energy Technology Platform.

van Leeuwen, M. and Nieuwenhuis, M. (2010). Retrieval of forest structural parameters using lidar remote sensing. *European Journal of Forest Research*, 129:749–770.

Verhoef, A., McNaughton, K., and Jacobs, A. (1997). A parameterization of momentum roughness length and displacement height for a wide range of canopy densities. *Hydrology and Earth System Sciences*, 1:81–91.

Vertex IV (2007). *Vertex IV and Transponder T3 manual*. Haglöf Sweden AB, Box 28, 88221 Långsele, Sweden.

Watanabe, T. (2004). Large-eddy simulation of coherent turbulence structures associated with scalar ramps over plant canopies. *Boundary-Layer Meteorology*, 112:307–341.

Weiss, M., Baret, F., Smith, G., Jonckheere, I., and Coppin, P. (2004). Review of methods for in situ leaf area index determination Part II. Estimation of LAI, errors and sampling. *Agricultural and Forest Meteorology*, 121:37–53.

Wilcox, D. C. (2006). *Turbulence Modeling for CFD*. DCW Industries, Inc., La Canada.

Wilson, J., Ward, D., Thurtell, G., and Kidd, G. (1982). Statistics of atmospheric turbulence within and above a corn canopy. *Boundary-Layer Meterology*, 24:495–519.

Wilson, N. and Shaw, R. (1977). A higher order closure model for canopy flow. *Journal of Applied Meterology*, 16:1198–1205.

Xue, M., Droegemeier, K., and Wong, V. (2000). The Advanced Regional Prediction System (ARPS) – A multi-scale nonhydrostatic atmospheric simulation and prediction model. Part I. Model dynamics and verification. *Meteorology and Atmospheric Physics*, 75:161–193.

Xue, M., Droegemeier, K., Wong, V., Shapiro, A., and Bewster, K. (1995). ARPS Version 4.0 User's Guide. Technical report, Center for Analysis and Prediction of Storms, University of Oklahoma, Norman, OK.

Xue, M., Droegemeier, K., Wong, V., Shapiro, A., Brewster, K., Carr, F., Weber, D., Liu, Y., and Wang, D. (2001). The Advanced Regional Prediction System (ARPS) – A multi-scale nonhydrostatic atmospheric simulation and prediction tool. Part II. Model physics and applications. *Meteorology and Atmospheric Physics*, 76:143–165.

Yang, B., Morse, A., Shaw, R., and Paw U, K. (2006). Large-eddy simulation of turbulent flow across a forest edge. Part II: momentum and turbulent kinetic energy budgets. *Boundary-Layer Meteorology*, 121:433–457.

Zilitinkevich, S. (2008). The effect of stratification on the aerodynamic roughness length and displacement height. *Boundary-Layer Meteorology*, 129:179–190.

This thesis was submitted as partial fulfillment of the requirements for a PhD degree based on work carried out at the Department of Wind Energy of the Technical University of Denmark over a three year period. Financial support was provided by the Center for Computational Wind Turbine Aerodynamics and Atmospheric Turbulence (COMWIND) sponsored by the Danish Council for Strategic Research, grant number 09-067216, and Vattenfall.

ISBN 978-87-93278-03-5

DTU Wind Energy - Technical University of Denmark
Frederiksborgvej 399, P.O. Box 49
DK-4000 Roskilde

www.vindenergi.dtu.dk